THÈSE

En vue de l'obtention du

DOCTORAT DE L'UNIVERSITÉ DE TOULOUSE

Délivré par :

Institut National Polytechnique de Toulouse (INP Toulouse)

Discipline ou spécialité :

Signal, Image, Acoustique et Optimisation

Présentée et soutenue par :

Mme NINGNING ZHAO

le jeudi 20 octobre 2016

Titre :

INVERSE PROBLEMS IN MEDICAL ULTRASOUND IMAGES - APPLICATIONS TO IMAGE DECONVOLUTION, SEGMENTATION AND SUPER-RESOLUTION

Ecole doctorale :

Mathématiques, Informatique, Télécommunications de Toulouse (MITT)

Unité de recherche :

Institut de Recherche en Informatique de Toulouse (I.R.I.T.)

Directeur(s) de Thèse :

M. DENIS KOUAME

M. JEAN YVES TOURNERET

Rapporteurs :

M. ALI MOHAMMAD-DJAFARI, SUPELEC

M. JEAN-MARC GIRAULT, UNIVERSITE DE TOURS

Membre(s) du jury :

M. JEAN-CHRISTOPHE PESQUET, UNIVERSITE PARIS 5, Président

M. ADRIAN BASARAB, UNIVERSITE PAUL SABATIER, Membre

M. DENIS KOUAME, UNIVERSITE PAUL SABATIER, Membre

M. JEAN YVES TOURNERET, INP TOULOUSE, Membre

Acknowledgements

I would like to appreciate my supervisors professor Denis Kouamé, professor Jean-Yves Tourneret firstly. Many thanks are given to them for the opportunity to join this work. Besides, they have helped me a lot during my PhD studies. I would also like to appreicate my co-supervisor Adrian Basarab. Without his help and guidence, my PhD work cannot finish smoothly.

I would like to thank China Scholarship Council (CSC) for supporting my PhD work at University of Toulouse. I would also like to thank my committee members, professor Jean-Christophe Pesquet, professor Ali Mohammad-Djafari and Jean-Marc Girault. Thanks a lot for their brilliant comments and questions about my PhD work. Moreover, I would like to thank professor Jean-Christophe Pesquet for accepting me as a visiting student in his lab for one month.

A special thanks will be given to my Chinese friends (Dou Qian, Su Qiankun, Lei Fang, Xue Rui, Ge Ning$\cdots$) and colleagues from the teams SC (Sebastien, Pierre-Antoine, Abder$\cdots$) and TCI (Zhouye, Teodora). Thanks them for accompanying me for last three or four years. Another special thanks will be given to my parents, my sisters (Jing and Dan) and my boyfriend Qi. Thanks them for supporting, encouraging and accompanying me all the time.

Résumé

L'imagerie ultrasonore est une modalité d'acquisition privilégiée en imagerie médicale en raison de son innocuité, sa simplicité d'utilisation et son coût modéré d'utilisation. Néanmoins, la résolution limitée et le faible contraste limitent son utilisation dans certaines d'applications. C'est dans ce contexte que différentes techniques de post-traitement visant à améliorer la qualité de telles images sont proposées dans ce manuscrit. Dans un premier temps, nous proposons d'aborder le problème conjoint de la déconvolution et de la segmentation d'images ultrasonores en exploitant l'interaction entre ces deux problèmes. Le problème, énoncé dans un cadre bayésien, est résolu à l'aide d'un algorithme MCMC en raison de la complexité de la loi a posteriori des paramètres d'intérêt. Dans un second temps, nous proposons une nouvelle méthode rapide de super-résolution fondée sur la résolution analytique d'un problème de minimisation l2-l2. Il convient de remarquer que les deux approches proposées peuvent être appliquées aussi bien à des images ultrasonores qu'à des images naturelles ou constantes par morceaux. Enfin, nous proposons une méthode de déconvolution aveugle basée sur un modèle paramétrique de la réponse impulseionelle de l'instrument ou du noyau de flou.

Abstract

In the field of medical image analysis, ultrasound is a core imaging modality employed due to its real time and easy-to-use nature, its non-ionizing and low cost characteristics. Ultrasound imaging is used in numerous clinical applications, such as fetus monitoring, diagnosis of cardiac diseases, flow estimation, etc. Classical applications in ultrasound imaging involve tissue characterization, tissue motion estimation or image quality enhancement (contrast, resolution, signal to noise ratio). However, one of the major problems with ultrasound images, is the presence of noise, having the form of a granular pattern, called speckle. The speckle noise in ultrasound images leads to the relative poor image qualities compared with other medical image modalities, which limits the applications of medical ultrasound imaging. In order to better understand and analyze ultrasound images, several device-based techniques have been developed during last 20 years. The object of this PhD thesis is to propose new image processing methods allowing us to improve ultrasound image quality using post-processing techniques. First, we propose a Bayesian method for joint deconvolution and segmentation of ultrasound images based on their tight relationship. The problem is formulated as an inverse problem that is solved within a Bayesian framework. Due to the intractability of the posterior distribution associated with the proposed Bayesian model, we investigate a Markov chain Monte Carlo (MCMC) technique which generates samples distributed according to the posterior and use these samples to build estimators of the ultrasound image. In a second step, we propose a fast single image super-resolution framework using a new analytical solution to the l2-l2 problems (i.e., ℓ_2-norm regularized quadratic problems), which is applicable for both medical ultrasound images and piece-wise/natural images. In a third step, blind deconvolution of ultrasound images is studied by

considering the following two strategies: i) A Gaussian prior for the PSF is proposed in a Bayesian framework. ii) An alternating optimization method is explored for blind deconvolution of ultrasound images using parametric model for the PSF/blurring kernel.

Acronyms and notations

Acronymes

ADMM	alternating direction method of multipliers
AWGN	additive white Gaussian noise
BCCB	block circulant matrix of circulant blocks
BCD	block coordinate descent
BSNR	blurred signal-to-noise ratio
CNR	contrast-to-noise ratio
CSC	China Scholarship Council
CT	computed tomography
DFT	discrete Fourier transform
EM	expectation maximization
FB	forward-backward
FFT	fast Fourier transform
GGD	generalized Gaussian distribution
GPU	graphics processing units
HMC	Hamiltonian Monte Carlo
HR	high resolution
iFFT	inverse fast Fourier transform

i.i.d	independent and identically distributed
IRIT	Institut de Recherche en Informatique de Toulouse
ISNR	improvement in signal-to-noise ratio
IST	iterative shrinkage/thresholding
LR	low resolution
MAP	maximum a posteriori
MCMC	Markov Chain Monte Carlo
MMSE	minimum mean square error
MRI	magnetic resonance imaging
MSSIM	image structural similarity
NMSE	normalized mean square error
NRMSE	normalized root mean square error
OA	overall accuracy
PDF	probability density function
PSF	point spread function
PSNR	peak signal-to-noise ratio
PSRF	potential scale reduction factor
PZT	piezoelectric
RF	radio-frequency
RG	resolution gain
RMSE	root mean square error
SNR	signal-to-noise ratio
SR	super resolution
TRF	tissue reflectivity function
TV	total variation

US	ultrasound
w.r.t.	with respect to

Mathematical symbols

$\propto$	proportional to
$\ll$	much lower
$\gg$	much greater
$\delta(\cdot)$	Dirac delta function
$\imath_C(\cdot)$	indicator function on set C
$\otimes$	Kronecker product
$\circledast$	cyclic convolution
$\|\cdot\|_F$	Frobenius norm
$\|\cdot\|_2$	ℓ_2 norm
$\|\cdot\|_1$	ℓ_1 norm
$\|\cdot\|_0$	ℓ_0 pseudo norm
$\mathrm{tr}\,(\cdot)$	trace of matrix
∇	differential operator
$\odot$	Hadamard product

Contents

Acknowledgements iii

Résumé v

Abstract vii

Acronyms and notations x

Introduction 1

List of publications 5

Chapter 1 Medical ultrasound imaging 7

1.1 Ultrasound imaging background 7

1.1.1 Attributes and applications 8

1.1.2 Ultrasound propagation 12

1.1.3 Ultrasound transducer 17

1.1.4 Ultrasound data 20

1.2 Ultrasound image formation 23

1.2.1 Received signal 23

1.2.2 Point spread function 24

1.3 Post-processing techniques in ultrasound imaging 25

1.3.1 Introduction to inverse problems . . . 25
1.3.2 Speckle reduction . . . 26
1.3.3 Image deconvolution . . . 27
1.3.4 Image segmentation . . . 32
1.3.5 Single image super-resolution . . . 34
1.4 Conclusion . . . 35

Chapter 2 Joint deconvolution and segmentation of ultrasound images 37

2.1 Introduction . . . 38
2.1.1 Problem Statement . . . 38
2.1.2 Related Work . . . 39
2.1.3 Proposed method . . . 40
2.2 Bayesian Model for Joint Deconvolution and Segmentation . . . 40
2.2.1 Likelihood . . . 42
2.2.2 Prior Distributions . . . 42
2.2.3 Joint posterior distribution . . . 44
2.3 Sampling the posterior and computing the Bayesian estimators . . . 44
2.3.1 Hybrid Gibbs sampler . . . 45
2.3.2 Parameter estimation . . . 48
2.3.3 Computational complexity analysis . . . 49
2.4 Experimental results . . . 49
2.4.1 Evaluation metrics . . . 49
2.4.2 Sampler convergence . . . 51
2.4.3 Computational complexity . . . 52
2.4.4 Synthetic data . . . 52
2.4.5 Joint Deconvolution and Segmentation . . . 55
2.5 Conclusions . . . 68

Chapter 3 Fast Single Image Super-resolution **69**

3.1 Introduction . . . 69

3.2 Image Super-resolution Formulation . . . 71

3.2.1 Model of Image Formation . . . 71

3.2.2 Problem formulation . . . 72

3.3 Proposed fast super-resolution using an ℓ_2-regularization . . . 73

3.3.1 Proposed closed-form solution for the $\ell_2 - \ell_2$ problem . . . 74

3.3.2 Solution of the $\ell_2 - \ell_2$ problem in the image domain . . . 76

3.3.3 Solution of the $\ell_2 - \ell_2$ problem in the gradient domain . . . 77

3.4 Generalized fast super-resolution . . . 79

3.4.1 General form of the proposed algorithm . . . 80

3.4.2 TV regularization . . . 80

3.4.3 ℓ_1-norm regularization in the wavelet domain . . . 82

3.4.4 Learning-based ℓ_2-norm regularization . . . 83

3.5 Experimental Results . . . 83

3.5.1 Fast SR using ℓ_2-regularizations . . . 84

3.5.2 Natural images: Embedding the $\ell_2 - \ell_2$ analytical solution into the ADMM . . . 91

3.5.3 Medical ultrasound images: Embedding the $\ell_2 - \ell_2$ analytical solution into the ADMM framework . . . 99

3.6 Conclusion . . . 101

Chapter 4 Blind-deconvolution of ultrasound images **103**

4.1 Introduction . . . 103

4.2 Blind deconvolution using a Gaussian prior for the PSF . . . 105

4.2.1 Hierarchical Bayesian model . . . 105

4.2.2 Hybrid Gibbs Sampler . . . 108

4.2.3 Simulation results . . . 110

4.3 Blind deconvolution using a parametric model for the PSF . . . 114

4.3.1 Parametric model of the PSF . . . 114
4.3.2 Optimization Problem Formulation . . . 116
4.3.3 BCD-based algorithms . . . 117
4.3.4 Simulation results . . . 121
4.4 Conclusion . . . 123

Conclusions and perspectives **127**

Appendices **131**

Appendix A Computation of blurring operator . . . 133
A.1 Block circulant matrix with circulant blocks . . . 133
A.2 Spectral decomposition . . . 135
A.2.1 General definitions . . . 135
A.2.2 Spectral decomposition of a BCCB matrix . . . 135
Appendix B Appendices of Chapter 2 . . . 137
B.1 Determinations of the conditional distributions of the noise variance and scale parameters 137
B.2 Sampling the shape parameters with an RWMH Algorithm . . . 138
B.3 Sampling the TRF using an Hamiltonian Monte Carlo Algorithm . . . 139
B.3.1 HMC Algorithm . . . 139
B.3.2 Tuning the parameters ϵ and L . . . 140
Appendix C Appendices of Chapter 3 . . . 143
C.1 Derivation of the analytical solution (3.13) . . . 143
C.2 Pseudo codes of the proposed fast ADMM super-resolution methods for TV and ℓ_1-norm regularizations . . . 145
Appendix D Calculation of proximity operators . . . 147
D.1 Definition . . . 147
D.2 Proximity operator of $|x|^p$ . . . 147
Appendix E Proximal hamiltonian Monte Carlo (PHMC) method . . . 151
E.1 Proximal Metropolis adjusted Langevin algorithm . . . 151

E.2 Proximal Hamiltonian Monte Carlo algorithm 152
E.3 Generalization to deconvolution problem 153

Bibliography **174**

List of Figures

1.1 A sound wave consists of pressure fluctuations. Diagnostic ultrasound waves are longitudinal waves with the motion of particles in a direction parallel to the direction of energy transport [LCR07]. 8

1.2 Block diagram of an ultrasound imaging process [Ale10]. 9

1.3 External parts of a medical ultrasound imaging system. 9

1.4 Specular reflection (left) versus scattering/diffuse reflection (right). 13

1.5 Specular reflection and transmission at the boundaries of two media. 14

1.6 Spatial resolution of an ultrasound imaging system. 15

1.7 Lateral resolution of ultrasound imaging. 16

1.8 Different kinds of ultrasound probes. 18

1.9 Basic piezoelectric ultrasound transducer structure [Sza04]. 18

1.10 Transducer arrays contain multi elements. A: linear; B: Phased; C: Convex [Tou14]. . 19

1.11 Conceptual diagram of electronic beamforming. Top: Focalization in transmission in US imaging scanners. Bottom: Focalization in reception in US imaging scanners [Tou14]. 21

1.12 RF image and its corresponding B-mode image of thyroid [Bas08, Mor13]. The extracted axial profiles from the two images are shown at the right side of the figure. . . 22

1.13 Relationship between ultrasound RF, IQ and B modes. “LBP” in the demodulation stage represents low band-pass filter. 23

1.14 Point spread function of an electronically focused array at the focal point [LCR07]. . . 24

1.15 Point spread function phantom simulated using the Field II software [Jen96]. Different apodization and focolization are employed in each image. 25

1.16 Spectrum (left) and log cepstrum (right) of measured PSF and sythetic reflectivity function for an A-line signal. The two images are extracted from [JL94]. 29

2.1 Hierarchical Bayesian model for the parameter and hyperparameter priors, where the TRF $\mathbf{x}$ is modeled by a mixture of GGDs, the hidden label field $\mathbf{z}$ follows a Potts MRF and the parameters appearing in the boxes are fixed in advance. 45

2.2 CPU time of our algorithm versus the image size (left) and the number of classes (right) for 6000 Monte Carlo iterations. Left: number of classes K = 2. Right: image size 100×100. 52

2.3 Deconvolution results for one column of the synthetic image (the red curves are the observed lines, the blue curves are the ground truth and the green curves are the restored signals using the proposed method). The GGD parameters are $\xi = 2$,$\gamma = 2$ in (a), $\xi = 1.5$,$\gamma = 1.2$ in (b) and $\xi = 0.6$,$\gamma = 0.4$ in (c). 53

2.4 Estimated marginal posterior distributions (histograms) of the noise variance σ_n^2 (1st line), the hyperparameters ξ (2nd line) and γ (3rd line). The vertical lines represent the ground truths of the corresponding parameters. Each column corresponds to a given image. 54

2.5 OA versus the ratios of the GGD parameters (left: scale parameters $\gamma_1 = \gamma_2 = 20$, right: shape parameters $\xi_1 = \xi_2 = 1$). 55

2.6 Group 1: (a) Simulated PSF; (b) Ground truth of the TRF; (c) Ground truth for label map; (d) Observed B-mode image; (e)-(i) Estimated TRFs in B-mode form obtained with methods ℓ_2, ℓ_1, $\text{Deconv}_{\text{EM}}$, $\text{Deconv}_{\text{MCMC}}$ and the proposed $\text{Joint}_{\text{MCMC}}$; (j) Estimated label map obtained with the proposed method (regularization parameters for the ℓ_2 and ℓ_1 methods set to 0.01 and 0.1). 57

2.7 (Group 1) 1st line includes the histograms of shape parameters $\boldsymbol{\xi}$ for the pixels inside (left) and outside (right) the inclusion; 2nd line includes the histograms of scale parameters $\boldsymbol{\gamma}$ for the pixels inside (left) and outside (right) the inclusion; The red and green vertical lines are the MMSE estimates and the true values of the parameters $\boldsymbol{\xi}$, $\boldsymbol{\gamma}$, respectively. 58

2.8 Group 2: (a) Ground truth of the TRF; (b) Ground truth for label map; (c) Observed B-mode image; (d)-(h) Estimated TRFs in B-mode form obtained with the methods ℓ_2, ℓ_1, $\text{Deconv}_{\text{EM}}$, $\text{Deconv}_{\text{MCMC}}$ and the proposed $\text{Joint}_{\text{MCMC}}$; (i) Estimated label map obtained with the proposed method (regularization parameters for the ℓ_2 and ℓ_1 methods set to 0.1 and 1). 60

2.9 Group 3: (a) Ground truth of the TRF; (b) Ground truth for label map; (c) Observed B-mode image; (d)-(h) Estimated TRFs in B-mode form obtained with methods ℓ_2, ℓ_1, $\text{Deconv}_{\text{EM}}$, $\text{Deconv}_{\text{MCMC}}$ and the proposed $\text{Joint}_{\text{MCMC}}$; (i) Estimated label map obtained with the proposed method (regularization parameters for the ℓ_2 and ℓ_1 methods set to 0.1 and 1). 61

2.10 Estimated TRF (left) and label map (right) for a two-class image with $K = 3$ (ISNR $= 14.46$ and OA $= 0.8$). 63

2.11 From up to down: 1st row corresponds to the mouse bladder; 2nd row is for the skin melanoma; 3rd row is for the healthy skin tissue. From left to right: Observed B-mode image, Restored B-mode images with ℓ_2-norm, ℓ_1-norm and the proposed method. The regions selected for computing CNR are shown in the red boxes in the observed B-mode images. 66

2.12 Vertical profiles passing through the skin tumor, extracted from the observed and restored images of the skin melanoma (group 2). 67

2.13 Marginal MAP estimates of labels. (Left) is the label map for the mouse bladder. The estimated labels in blue correspond to liquid regions whereas the other labels represent tissue regions with different statistical properties. (Middle) is the label map for the skin melanoma. The four estimated labels correspond to the water-gel (light blue), the tumor (yellow) and the skin tissues (the two shades of red). (Right) is the label map for the healthy skin tissue. The skin tissue appears in red. 67

3.1 Effect of the up-sampling matrix $\mathbf{S}^H$ on a 3×3 image and of the down-sampling matrix $\mathbf{S}$ on the corresponding 9×9 image (whose scale up factor equals 3). 72

3.2 SR of the pepper image when considering an $\ell_2-\ell_2$-model in the image domain: visual results. The prior image mean $\bar{\mathbf{x}}$ is defined as the bicubic interpolated LR image in Case 1 and as the ground truth HR image in Case 2. 85

3.3 SR of the "pepper" image when considering the $\ell_2-\ell_2$ model in the image domain: RMSE as functions of the regularization parameter τ for various noise levels (1st column), blurring kernel sizes (2nd column) and decimation factors (3rd column). The results in the 1st column were obtained for $d_r = d_c = 4$ and 9×9 kernel size; in the 2nd column, $d_r = d_c = 4$ and BSNR= 30 dB; in the 3rd column, the kernel size was 9×9 and BSNR= 30 dB. 86

3.4 SR of the motion blurred image when considering an $\ell_2-\ell_2$-model in the image domain: visual results. The prior image mean $\bar{\mathbf{x}}$ is defined as the bicubic interpolated LR image in Case 1 and as the ground truth HR image in Case 2. 87

3.5 SR of the face image when considering an $\ell_2-\ell_2$-model in the gradient domain: visual results. 89

3.6 SR of the face image when considering an $\ell_2-\ell_2$-model in the gradient domain: objective functions. 89

3.7 SR of the face image when considering an $\ell_2-\ell_2$-model in the gradient domain: visual results. 90

3.8 SR of the Monarch, Lena and Barbara images when considering a TV-regularization: visual results. 93

3.9 SR of the Monarch, Lena and Barbara images when considering a TV-regularization: objective function (left) and ISNR (right) vs time. 94
3.10 SR of the Monarch, Lena and Barbara images when considering a ℓ_1-norm regularization in the wavelet domain: visual results. 95
3.11 SR of the Monarch, Lena and Barbara images when considering an ℓ_1-norm regularization in the wavelet domain: objective function (left) and PSNR (right) vs time. . . 98
3.12 *In vivo* US image and the restored images with the proposed and classical methods using ℓ_p norm regularizers. 100
4.1 Observation, ground truth and estimated US images (top: RF images, bottom: B-mode images). 112
4.2 Ground truth and estimated PSFs. 112
4.3 Blind deconvolution of real US image which corresponds to healthy skin tissue. (a) is the observation; (b),(c) are the estimated PSFs using the homomorphic technique and the proposed method; (d), (e) are the restored US TRF using non-blind deconvlution method and the proposed method; (f) is the estimated labels jointly. 113
4.4 Simulated PSF with the proposed parametric model (4.18). 115
4.5 Graph of proximity operator of $|\cdot|^p$ $(0 < p \leq 2)$. 119
4.6 Blind deconvolution of simulated US images using a parametric model for the PSF. . . 123
4.7 Blind deconvolution of real US images using a parametric model for the PSF. 125
A.1 A BCCB matrix of size 9×9. 134
D.1 Plot of $g(x)$ for $x > 0$. 149

List of Tables

1.1 Comparison of different medical imaging modalities [Sza04]. 10
2.1 Parameter Estimations for the synthetic data 54
2.2 Hyperparameter Estimations for Simulated data (Group 2). 59
2.3 Deconvolution Quality Assessment for Simulated data 62
2.4 Deconvolution Quality for the real US data 68
3.1 SR assessment of the pepper image when considering an $\ell_2 - \ell_2$-model in the image domain. 85
3.2 SR assessment of the motion blurred image using an $\ell_2 - \ell_2$-model in the image domain. 88
3.3 SR of the face image when considering an $\ell_2 - \ell_2$-model in the gradient domain: quantitative results. 88
3.4 SR of the zebra image when considering a learning-based ℓ_2-norm regularization: quantitative results. 91
3.5 SR of the Monarch, Lena and Barbara images when considering a TV-regularization: quantitative results. 96
3.6 SR of the Monarch, Lena and Barbara images when considering a ℓ_1-norm regularization in the wavelet domain: quantitative results. 97
3.7 SR of the real US image 99
4.1 Performance of reflectivity image estimation. 111
4.2 Performance of PSF estimation. 112
4.3 Simulated US images: Performance of blind deconvolution using parametric PSF model. 122

Introduction

Motivation

Medical ultrasound (US) imaging is one of the most widely employed imaging modalities due to its harmless, portable, cost efficient and real time properties compared with other medical imaging modalities, e.g., X-ray, computed tomography (CT), magnetic resonance imaging (MRI) and positron emission tomography (PET). Particularly, due to the advances in ultrasound hardware conducted during last 20 years, clinical diagnosis using ultrasound systems is very common nowadays in radiology, cardiology and obstetrics. Moreover, driven by the healthcare needs and the requirement for low-cost imaging solutions, ultrasound is the first modality that is chosen for obstetrics, breast mass assessment and cardiovascular diseases. Besides, ultrasound is the only imaging modality capable of imaging soft tissue deformations quickly enough for the interventional procedure guidance. However, the relative poor image quality (e.g., low resolution and contrast) still limits the applications of medical ultrasound modality. Inspired by the tight relationship between image processing techniques and medical image analysis, it is more and more interesting to improve ultrasound image quality using some post-processing techniques besides the device-based methods. Among the existing post-processing techniques, restoration (denoising, deconvolution, blind-deconvolution, etc.) and segmentation remain necessary steps in ultrasound image analysis in order to obtain qualitative measurements such as the location of objects of interest, as well as the quantitative measurements such as area, volume or the analysis of dynamic behavior of anatomical structures. This PhD thesis deals with the problems of ultrasound image quality improvement using post-processing techniques,

including deconvolution, segmentation and super-resolution.

Organization of the manuscript

- **Chapter 1:** This chapter reminds the basic principles related to medical US imaging. In addition to the physics related to ultrasound image acquisition, the linear image formation model including the point spread function (PSF)/blurring kernel is presented. Moreover, several widely studied post-processing techniques and some related state-of-the-art methods for medical ultrasound imaging are reported.

- **Chapter 2:** This chapter presents a Bayesian method for joint deconvolution and segmentation of ultrasound images. Due to the tight relationship between these two problems, some methods coupling deconvolution and segmentation have been recently considered for piece-wise homogeneous/natural images. However, these methods are not always efficient for US images because of the presence of speckle noise. In this chapter, a new model for joint segmentation and deconvolution of ultrasound images is proposed within a Bayesian framework. Since the posterior distribution obtained with the proposed Bayesian model is intractable, a Markov chain Monte Carlo (MCMC) method based on a Gibbs sampler is investigated to sample the posterior distribution. The generated samples are then used to build the Bayesian estimators of the unknown model parameters.

- **Chapter 3:** This chapter presents a fast single image super-resolution (SR) method, which consists of recovering a high resolution image from its blurred, decimated and noisy version. The existing algorithms for single image SR include the traditional first-order gradient methods and the recent splitting-based methods dividing the SR problem into separate up-sampling and deconvolution steps that can be easily solved. Instead of following this splitting strategy, we propose to deal with the decimation and blurring operators simultaneously. The proposed method is sufficiently generic to deal with medical US images and natural piece-wise constant images. Different priors can be considered according to the image modalities of interest, including Laplacian, Gaussian, generalized Gaussian or TV priors.

- **Chapter 4:** While the deconvolution problems studied in the two previous chapters are supposed to be non-blind, i.e., the point spread function is estimated as a prerequisite step, this chapter studies the blind deconvolution of US images. Our first approach for tackling this problem consists of assigning a Gaussian prior to the PSF and to formulate the blind deconvolution problem within a Bayesian framework. An appropriate Gibbs sampler is then proposed to sample the posterior of this Bayesian model and to build Bayesian estimators of the parameters of interest. A second idea investigated in this chapter is based on a parametric model for the PSF. Given the parametric model for the PSF, several parameters are estimated instead of the whole PSF, which can reduce computational burden. The blind deconvolution problem is finally formulated as an optimization problem further solved within a variational framework.

Main Contributions

The main contributions of this thesis are as follows.

- **Chapter 2**. The contribution of this chapter is to propose a new hierarchical Bayesian model for joint segmentation and deconvolution of US images. This model is based on a mixture of generalized Gaussian distributions (GGDs) assigned to the tissue reflectivity function (TRF)/image to be estimated and a Potts model allowing interactions between pixels in a neighborhood to be considered. To our knowledge, the proposed method represents a first attempt for a joint segmentation and deconvolution in US imaging.

- **Chapter 3**. Single image super-resolution is addressed in this chapter. By taking advantage of the decimation and blurring operators' properties in the frequency domain, we show that it is possible to calculate the analytical solution of the $\ell_2 - \ell_2$ problem (i.e., Tikhonov regularized quadratic problem). Other general image priors (e.g., TV, ℓ_1-norm priors) can be considered by embedding this analytical solution into an alternating direction method of multipliers (ADMM) framework.

- **Chapter 4**. This chapter considers the blind deconvolution for ultrasound images. In order to estimate the PSF and the TRF jointly, a Gaussian prior is first considered in Bayesian inference. In a second step, a parametric model for the PSF is proposed in order to reduce the computational burden of the blind image deconvolution algorithm. The formulated problem is finally solved using an alternating optimization technique.

List of publications

International Journal papers

1. N. Zhao, Q. Wei, A. Basarab, N. Dobegion, D. Kouame and J.-Y. Tourneret, **Fast Single Image Super-resolution using a New Analytical Solution for $\ell_2 - \ell_2$ Problems**, *IEEE Trans. Image Process.*, 25(8):3683-3697, 2016.

2. N. Zhao, A. Basarab, D. Kouame and J.-Y. Tourneret, **Joint Segmentation and Deconvolution of ultrasound images using a hierarchical Bayesian Model based on generalized Gaussian Priors**, *IEEE Trans. Image Process.*, 25(8):3736-3750, 2016.

Conference papers

1. N. Zhao, A. Basarab, D. Kouame and J.-Y. Tourneret, **Restoration of ultrasound images using a hierarchical Bayesian model with a generalized Gaussian prior**, in *Proc. IEEE Int. Conf. Image Processing (ICIP)*, Paris, France, Oct. 2014.

2. N. Zhao, A. Basarab, D. Kouame and J.-Y. Tourneret, **Joint Bayesian Deconvolution And Point Spread Function Estimation For Ultrasound Imaging**, in *Proc. IEEE Int. Conf. Symposium on Biomedical Imaging: From Nano to Macro (ISBI)*, New York, USA, Apr. 2015.

3. Z. Chen, N. Zhao, A. Basarab and D. Kouame, **Ultrasound Compressive Deconvolution with Lp-Norm Prior**, in *Proc. IEEE Int. Conf. EUSIPCO*, Nice, Cote d'Azur, France, Sept. 2015.

4. N. Zhao, Q. Wei, A. Basarab, D. Kouame and J.-Y. Tourneret, **Single Image Super-resolution of medical ultrasound images using a fast algorithm**, in *Proc. IEEE Int. Conf. Symposium on Biomedical Imaging: From Nano to Macro (ISBI)*, Prague, Czech, Apr. 2015.

5. N. Zhao, Q. Wei, A. Basarab, D. Kouame and J.-Y. Tourneret, **Blind Deconvolution of Medical Ultrasound Images Using a Parametric Model for the Point Spread Function**, in *Proc. IEEE Int. Conf. Ultrasonics Symposium (IUS)*, Tours, France, Sep. 2016.

Chapter 1

Medical ultrasound imaging

Contents

1.1 Ultrasound imaging background 7
1.1.1 Attributes and applications 8
1.1.2 Ultrasound propagation 12
1.1.3 Ultrasound transducer 17
1.1.4 Ultrasound data 20
1.2 Ultrasound image formation 23
1.2.1 Received signal 23
1.2.2 Point spread function 24
1.3 Post-processing techniques in ultrasound imaging 25
1.3.1 Introduction to inverse problems 25
1.3.2 Speckle reduction 26
1.3.3 Image deconvolution 27
1.3.4 Image segmentation 32
1.3.5 Single image super-resolution 34
1.4 Conclusion 35

1.1 Ultrasound imaging background

Sound waves are caused by variation in the pressure within a medium. Precisely, a sound wave consists of repeating pattern of high and low pressure regions, as shown in Fig. 1.1. The wavelength λ is the shortest distance that the wave repeats itself, which is defined by

$$\lambda = \frac{c}{f} \tag{1.1}$$

where c is the speed of sound and f is its frequency. Note that the speed of sound depends on the medium. Particularly, the speed of sound in soft tissues takes values in the range $[1300, 1600]$

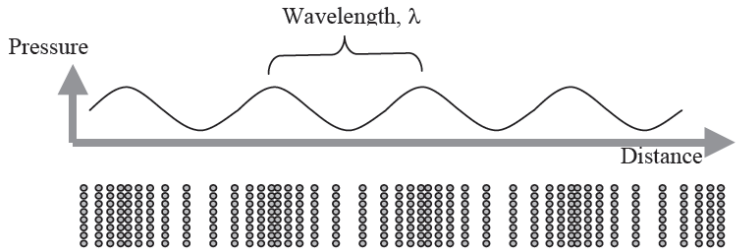

Figure 1.1: A sound wave consists of pressure fluctuations. Diagnostic ultrasound waves are longitudinal waves with the motion of particles in a direction parallel to the direction of energy transport [LCR07].

m/s with an average value of 1540 m/s. Ultrasound waves are characterized by frequencies higher than those audible to humans ($> 20,000$ Hz). Medical ultrasound imaging (also known as diagnostic sonography or ultrasonography) is a diagnostic imaging technique based on the use of ultrasound waves, i.e., it uses high-frequency sound waves to “view" inside the human body. The frequencies used in medical ultrasound generally range between 1-50 MHz. Ultrasound images (also known as sonograms) are obtained by detecting the reflected echos of the ultrasound pulses emitted into tissues using the same ultrasound probe.

During an ultrasound exam, a transducer (probe/scan head) is placed directly on the skin. A thin layer of gel is applied to couple the probe to the body since the ultrasound pulses are highly attenuated in the air. The echoes are then recorded and displayed as an image. The basic principle of US imaging process and the diagram of an ultrasound imaging system is shown in Fig. 1.2. Fig. 1.3 displays the externel parts of a medical ultrasound imaging system.

1.1.1 Attributes and applications

Attributes

A comparison between medical ultrasound imaging and other prominent medical imaging modalities such as X-ray computed tomography (CT) or magnetic resonance imaging (MRI), inspired from [Sza04] is presented in Table 1.1. Moreover, the attributes of medical ultrasound images are summarized and listed as below [Kre10],

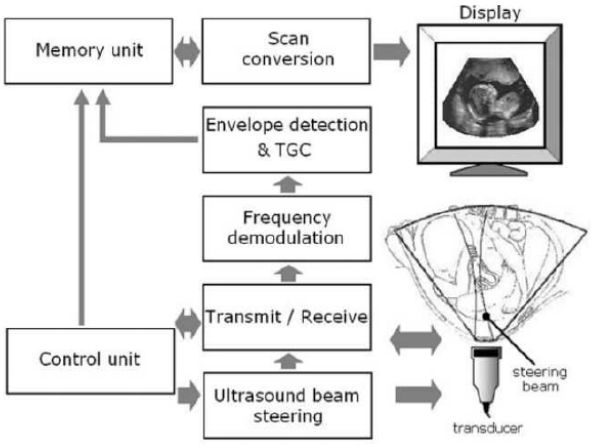

Figure 1.2: Block diagram of an ultrasound imaging process [Ale10].

Figure 1.3: External parts of a medical ultrasound imaging system.

Table 1.1: Comparison of different medical imaging modalities [Sza04].

Modality	Ultrasound	X-ray	CT	MRI
Principle	Mechanical properties	Mean tissue absorption	Tissue absorption	Biochemistry
Access	Small windows adequate	2 slides needed	Circumferential around body	Circumferential around body
Spatial resolution	Frequency and axially dependent $0.3 - 3$ mm	~ 1 mm	~ 1 mm	~ 1 mm
Penetration	Frequency dependent $3 - 25$ cm	Excellent	Excellent	Excellent
Safety	Very good	Ionizing radiation	Ionizing radiation	Very good
Speed	30-1000 frames/sec	Minutes	$\frac{1}{2}$ minute to minutes	10 frames/sec
Cost	$	$	$$$$	$$$$$$$$
Portability	Excellent	Good	Poor	Poor

- Safety: Ultrasound uses non-ionizing sound waves, which is an important advantage, in particular for the evaluation of fetal or gonadal tissues.
- Inexpensive: Ultrasound examination is less expensive to conduct than CT or MRI, leading to its improved availability possible in local low budget clinical environment.
- Portable: There are few (if any) contraindications to use medical ultrasound, compared with MRI or contrast-enhanced CT.
- Real time: The real-time nature of ultrasound imaging is useful for the evaluation of physiology as well as anatomy (e.g., fetal heart rate, the movement of the body's internal organs as well as blood flowing through the blood vessels).

However, ultrasonography suffers from some drawbacks, related to the non-negligible width of acoustic beam and finite bandwidth of the transducer [Ale10]. As a result, ultrasound images usually

have poor signal-to-noise ratio, limited contrast and spatial resolution. Besides, ultrasound waves do not penetrate bone or other tissues containing air very well. Therefore, it is difficult to visualize structures behind bones, e.g., brain. Moreover, training is required to accurately and efficienctly conduct an ultrasound exam and there is nonuniformity in the quality of examinations.

Applications

Medical ultrasound imaging is widely utilized in medicine. Usually, ultrasound is used to visualize internal body structures such as tendons, muscles, joints, vessels and internal organs. Its aim is often to find a source of a disease or to exclude any pathology. Clinical applications involving medical US imaging are summarized as follows [CSJ11, Sza04]:

- Cardiology: Echocardiography is an essential tool to diagnose cardiac diseases through the observation of the dilation of parts of the heart and of the function of heart ventricles and valves.
- Obstetrics: Obstetrical sonography is commonly used during pregnancy to check on the development of the fetus.
- Urology: Ultrasound can be used for measuring the blood flow through the kidney, seeing kidney stones or early detecting of prostate cancer.
- Angiology: Duplex ultrasound (B-mode vessel imaging combined with Doppler flow measurement) is daily used in angiology to diagnose arterial and venous disease all over the body.
- Emergency Medicine: Point of care ultrasound has many applications in the Emergency Department, including the Focused Assessment with Sonography for Trauma (FAST) exam for assessing significant hemoperitoneum or pericardial tamponade after trauma. Ultrasound is routinely used in the Emergency Department to expedite the care of patients with right upper quadrant abdominal pain who may have gallstones or cholecystitis.
- Gastroenterology/Colorectal surgery: In abdominal sonography, the solid organs of the abdomen such as the pancreas, aorta, inferior vena cava, liver, gall bladder, bile ducts, kidneys,

and spleen are imaged. Sound waves are blocked by gas in the bowel and attenuated in different degree by fat, therefore there are limited diagnostic capabilities in this area. The appendix can sometimes be seen when inflamed (e.g., appendicitis).

1.1.2 Ultrasound propagation

In a conventional pulse-echo ultrasound system, the ultrasound images are acquired by transmitting pulses into the body and detecting echoes reflected and backscattered by acoustic inhomogeneities. Thus, the physical phenomena during ultrasound propagation, e.g., reflection, scattering and attenuation, due to the interaction between ultrasound waves and medium decide the generation and the inherent properties (e.g., heavy speckle noise) of ultrasound images.

Reflection and scattering

When the emitted pulses travel through the interface between two media of different acoustic properties (acoustical impedance), the reflected echoes that travel back to the transducer and thus give information about the medium are due to reflection and scattering. Specular reflection happens when the reflector is large and smooth compared to the wavelength, where the reflected waves are in a singular direction. Conversely, scattering/diffuse reflection is taking place when the reflector is small compared to the wavelength. Fig. 1.4 displays the phenomena of specular reflection and scattering/diffuse reflection during ultrasound wave propagation.

- Reflection: As known from the basic physics, ultrasound waves are partially reflected or transmitted at the boundary between two media when the interfaces are large and flat. Reflection forms the basis of pulse-echo ultrasonic imaging and contributes to image formation displaying organ boundaries. The extent of reflection and transmission depends on the acoustic impedance, denoted as Z ($Z = \rho c$, where ρ is the density and c is the speed sound of the material). The amplitude of the reflected waves is proportional to the difference of the acoustic impedance of two materials, which is defined by the ratio of the reflected to the incident acoustic pressure

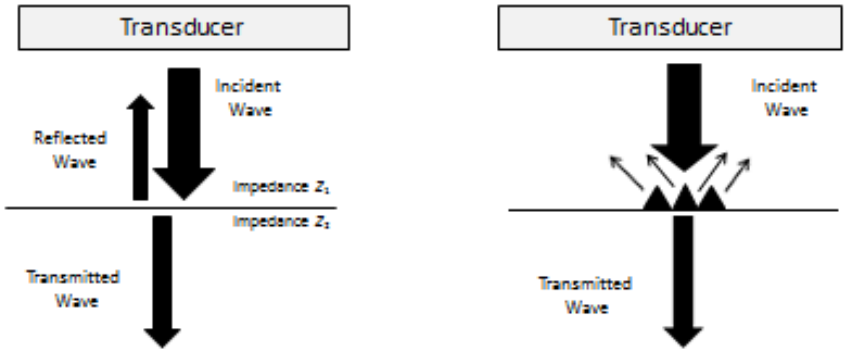

Figure 1.4: Specular reflection (left) versus scattering/diffuse reflection (right).

amplitude, called the amplitude reflection coefficient R defined by

$$R = \frac{Z_2 \cos\theta_1 - Z_1 \cos\theta_2}{Z_2 \cos\theta_1 + Z_1 \cos\theta_2} \tag{1.2}$$

where Z_1 and Z_2 are the acoustic impedances of the two tissues respectively. The ratio of the transmitted to the incident acoustic amplitude is called amplitude transmission coefficient T, which is given by

$$T = \frac{2Z_2 \cos\theta_1}{Z_2 \cos\theta_1 + Z_1 \cos\theta_2}. \tag{1.3}$$

- Scattering: During ultrasound wave propagation, the reflections from the interfaces whose dimensions (denoted as d) are very small, i.e., $d \ll \lambda$, are classified as scattering. The resulting detected echos have little angle dependence on the strength since the scattered waves spread in all directions. Compared with the strength of echos from large interfaces, the total ultrasound power scattered by the small targets is much smaller. Precisely, the scattered power (denoted as I_s) relative to the power of the incident pulse (denoted as I_i) is [Sza04]

$$\frac{I_s}{I_i} \propto d^6 f^4 \tag{1.4}$$

where f is the frequency of the pulse. This frequency dependence is often referred to as Rayleigh scattering [LCR07].

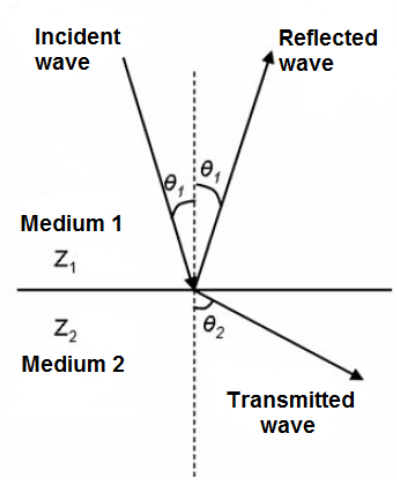

Figure 1.5: Specular reflection and transmission at the boundaries of two media.

Attenuation and Penetration

During ultrasound propagation, the loss of waves with distance is generally referred to as attenuation. The main mechanism contributions of ultrasound attenuation are absorption and scattering. Penetration, as the maximum distance that the ultrasonic beam can reach inside the tissue, is highly related with attenuation.

- Attenuation: The rate of the attenuation generally depends on two factors: i) the materials through which the waves are passing; ii) the ultrasound wave frequency (denoted as f). The energy lost during the wave propagation is caused by absorption (conversion into heat) or the scattering beam (out of the beam confines). In general, ultrasound attenuation is characterized by the following exponential decrease of the pressure. Considering the attenuation, a transmitted signal can be modeled by

$$p(z,t) = \exp(-\alpha z)s(t - z/c) \tag{1.5}$$

where z is the depth, $s(t-z/c)$ is the wave emitted by the probe along the axial of z and α is the attenuation coefficient of the medium defined by the ratio of the amplitudes on a logarithmic

scale, i.e.,

$$\alpha = 20 \log_{10}(A/A_0) \tag{1.6}$$

where A and A_0 are the amplitudes of the pulse at the depth of measurement and $z = 0$. Generally, α is given in dB/cm, which satisfies the relationship $\alpha_{\text{dB}} = 8.6886\alpha_{\text{nepers}}$ [Sza04]. Attenuation also depends on the frequency of pulse. For soft tissue, the attenuation coefficient is usually given as $0.3 - 0.6$ dB/cm/MHz [LCR07]. Thus, for deep organs, a low frequency (3-5 MHz) must be used to reduce the amount of attenuation.

- Penetration: Penetration is the maximum distance that the ultrasonic beam can reach inside the tissue. As stated above, higher frequencies lead to higher attenuation, then lower penetration. Thus, it is difficult to achieve good resolution at deeper depths given the trade-off between frequency and exploration depth.

Higher frequency ultrasound has shorter wavelength, thus the corresponding acquired image has better resolution. However, ultrasound with high frequency are absorbed easily, leading to more attenuation and less penetration. Therefore, high frequencies are used for scanning areas of the body close to the surface and low frequencies are used for areas that are deeper down in the body.

Resolution

- Spatial resolution: The spatial resolution of ultrasound images describes the minimum spacing

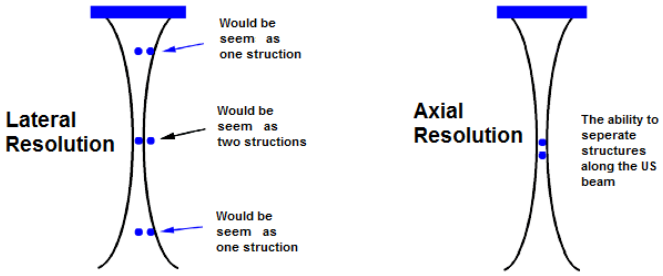

Figure 1.6: Spatial resolution of an ultrasound imaging system.

between two reflectors. The spatial resolution in ultrasound imaging mainly refers to the resolution along the axial direction (along the scan lines) and the lateral direction (perpendicular to the axial direction). Precisely, the axial spatial resolution is the ability to distinguish the closely spaced reflectors along/parallel to the beam axis, which mainly depends on the wavelength and frequency. Typically, the axial resolution is chosen equal to 2 wavelength

$$\lambda_{\text{ax}} = \frac{c}{2B} \tag{1.7}$$

where c is the sound velocity and B is the bandwidth of the pulse emitted by the transducer.

The lateral spatial resolution refers to the ability to distinguish closely spaced reflectors perpendicular to the beam, which depends on the beam width at the location of the reflectors and the focusing features [LCR07]. The lateral resolution is given by

$$\lambda_{\text{la}} = \frac{F\lambda}{D} \tag{1.8}$$

where F is the focal depth, D is the probe diameter and λ is the wavelength, as shown in Fig. 1.7.

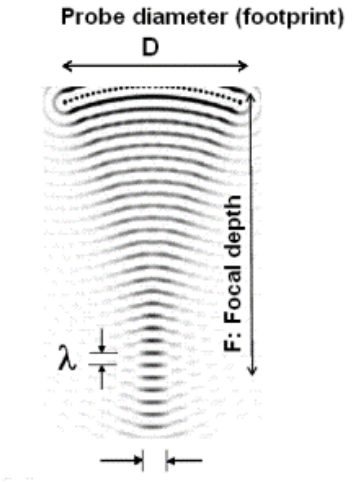

Figure 1.7: Lateral resolution of ultrasound imaging.

- Temporal resolution: In the standard brightness mode (B-mode) acquisition, the image is built as a collection of scan lines acquired in sequence. In this situation, temporal resolution is

synonymous with frame rate. Given the number of scan lines N, a maximum depth P and the sound speed c, the frame rate is given by

$$\mathrm{FR} = \frac{c}{2PN}. \tag{1.9}$$

For an image at 15 cm depth and 50 scan lines, the frame rate is approximately 100 frames/sec, i.e., a real time visualization is allowed. It is interesting to note that the ultrafast imaging in biomedical ultrasound developed in graphical processing unit (GPU) technology has permitted frame rates of $>$ 1000 frames per second [TF14b].

1.1.3 Ultrasound transducer

An ultrasound transducer/probe generates sound waves and receives echoes through conversion between electrical energy and mechanical energy. The ultrasound transducer highly affects the performance and imaging quality of ultrasonic scanner. According to different clinical applications, there exist different kinds of probes, see e.g., Fig. 1.8.

In an ultrasound probe, there are one or more quartz crystals called piezoelectric (PZT) crystals, as displayed in Fig. 1.9. When an electric current is applied to the crystals, these crystals vibrate rapidly. The rapid change of the crystals produce sound waves that travel through the tissues. Conversely, when sound waves hit the crystals, they emit electrical currents. This conversion of electrical energy to mechanical energy is known as PZT effect.

Transducer arrays

- Single element transducer: It contains only one element that cannot change focus.

- Array transducer: It contains more than one element, i.e., single slab of PZT crystal is sawed into separate elements, as shown in Fig. 1.9. Usually, multi-element transducers are manufactured because several scanning elements can be activated together to produce narrower beam (see Fig. 1.10). This beam can be formed by applying time delays to the individual elements that transmit excitation pulses. Moreover, the arrangement of transducer elements in an array

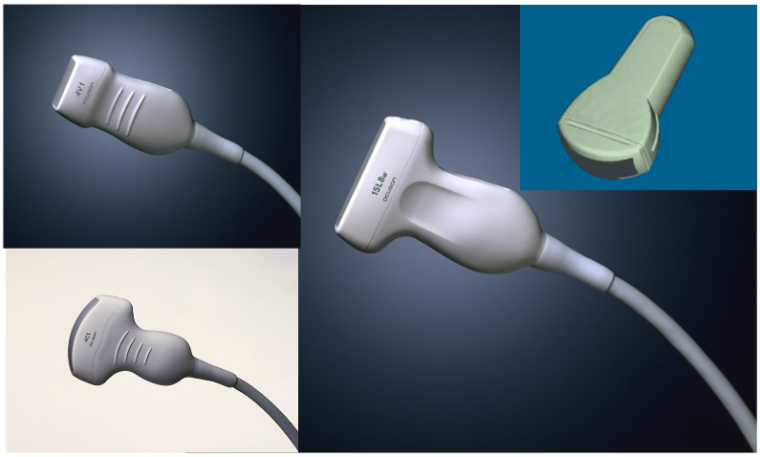

Figure 1.8: Different kinds of ultrasound probes.

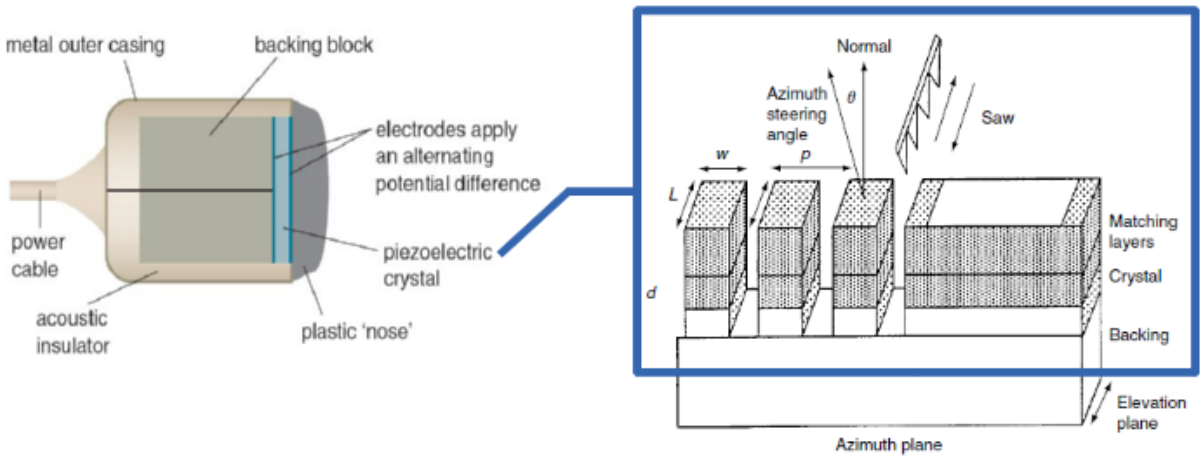

Figure 1.9: Basic piezoelectric ultrasound transducer structure [Sza04].

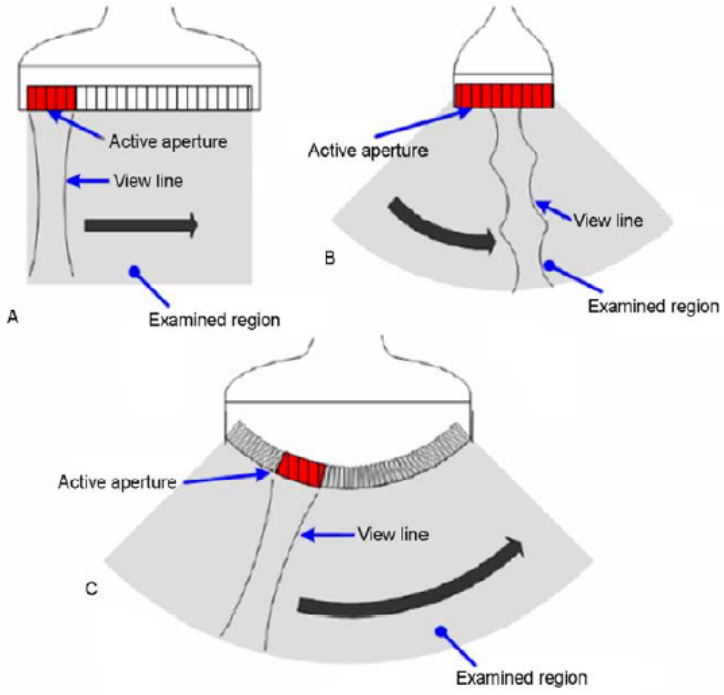

Figure 1.10: Transducer arrays contain multi elements. A: linear; B: Phased; C: Convex [Tou14].

makes it possible to focus or to steer the pulse-echo acoustic beam electrically by appropriately delaying the excitation pulses to each element. More illustrations about beamforming are presented in the following section.

1.1.4 Ultrasound data

Many different types of images can be formed using medical ultrasound instruments. The readers can refer to [Sza04] for detailed illustrations.

Beamforming

The ultrasound image acquisition can be divided into two main steps, i.e., transmission and reception. To concentrate the beam energy in a focal area, the transmission mode is when a subpart of the elements of the probe (called active elements) are acted together with previously delayed in such a way to obtain a summed beam at a focalization point. Then, the same probe switches in reception mode that record the reflected echoes from the scatterers. Then, the reflected signals are delayed and averaged, with or without apodization to create one radio-frequency (RF) line, as shown in Fig. 1.11. The accumulation of echoes in this way is referred to as delay-and-sum beamforming, which exists in both transmission and reception operations. The apodization in the beamforming is usually considered for reducing the amplitudes of side lobes in the incident pressure field. After repeating the transmission and reception operations along all the elements of the probe, one image called post-beamformed image/RF image is obtained. More recently, new beamforming techniques have been developed to improve ultrasound image formation, which is out of the scope of this manuscript. The readers can refer to [Tou14] and the references therein for more details illustrations.

RF, IQ signals

- RF: The radio frequency (RF) signal is the reflected signal obtained from the US imaging system after beamforming techniques.

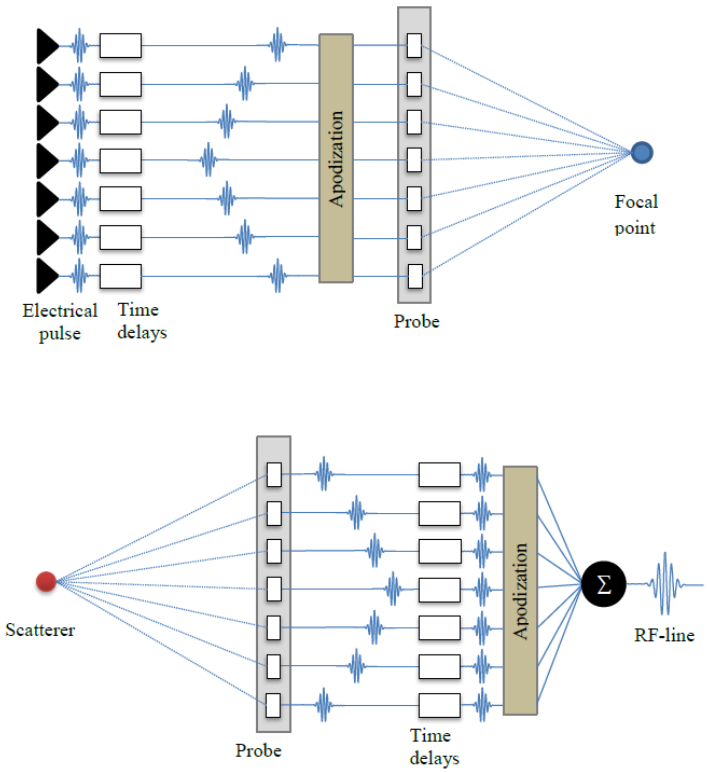

Figure 1.11: Conceptual diagram of electronic beamforming. Top: Focalization in transmission in US imaging scanners. Bottom: Focalization in reception in US imaging scanners [Tou14].

- IQ: The in phase/quadrature (IQ) signal, also called complex envelope signal, is the demodulated version of RF signal. It can be computed as

$$r_{\mathrm{IQ}} = [r_{\mathrm{RF}} - i\mathcal{H}(r_{\mathrm{RF}})]e^{-i\omega_0 t} \tag{1.10}$$

  where r_{RF}, r_{IQ} are the RF and IQ signals respectively, $\mathcal{H}(\cdot)$ represents the Hilbert transform and ω_0 is the central frequency of the ultrasound probe.

Ultrasound image modes

- A mode: The Amplitude mode is the simplest single dimension mode, where the signals are displayed as spikes related with the amplitude of the echoes.

- M mode: The motion mode, also called time motion (TM) mode, represents movement of structures over time. A 2D image is acquired initially and a single line is placed along the area of interest. The M mode displays the time history of this single line over time. Due to its good temporal resolution (high sampling rate), the M mode is valuable for evaluation of rapid movements, e.g., it is widely used in echocardiography given the dynamic output of the cardiac tissue. It is also often used with color flow Doppler for timing of abnormal flows.

- B mode: The ultrasound B-mode (B stands for brightness) images are 2D displays of echo signal amplitudes. Precisely, the envelopes of the received RF signals are detected previously by demodulating the RF signals. The corresponding amplitudes of the envelope signals are then logarithmically compressed, where the resulting generated data are B-mode images. The correspondence between a RF image and B-mode image of thyroid is shown in Fig. 1.12. Fig. 1.13 illustrates the relationship and calculation between RF, IQ and B-mode images.

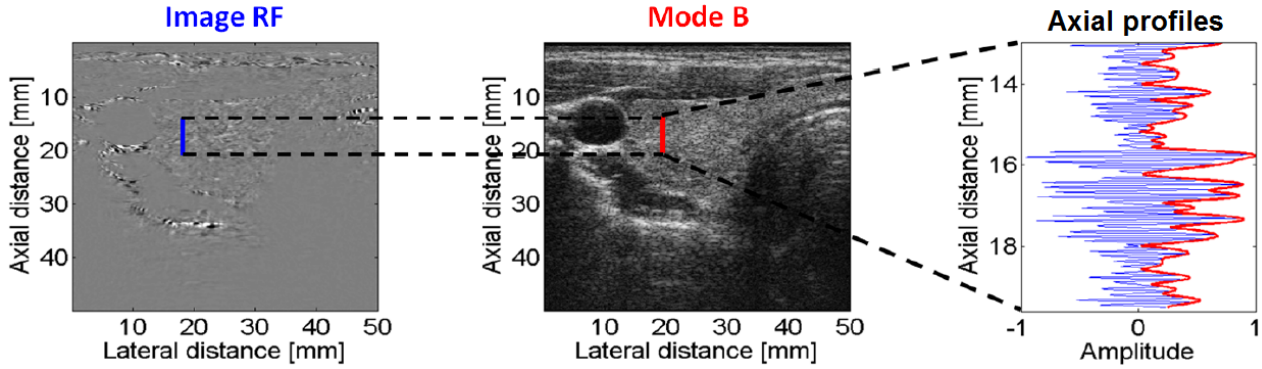

Figure 1.12: RF image and its corresponding B-mode image of thyroid [Bas08, Mor13]. The extracted axial profiles from the two images are shown at the right side of the figure.

- Other modes: Besides the US modes explained above, other widely used US modes include Doppler mode, continuous wave Doppler (CWD), pulse wave Doppler (PWD) and so on [Sza04], which are out of the scope of this manuscript.

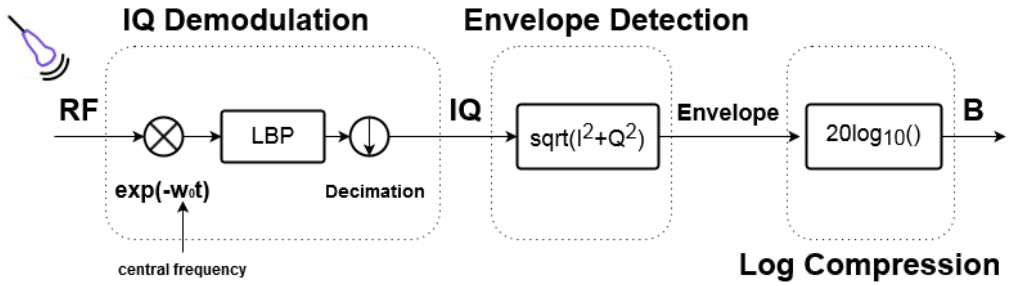

Figure 1.13: Relationship between ultrasound RF, IQ and B modes. "LBP" in the demodulation stage represents low band-pass filter.

1.2 Ultrasound image formation

Ultrasound images are produced based on the reflection of the waves on the body structures. By measuring the time between the transmission of a pulse and the reception of an echo, the ultrasound machine can calculate the distance between the probe and the tissue that caused the detected echo. This is the pulse-echo principle. In addition, the amplitude of the echoes also provide the information necessary to produce an image. This section motivates the linear model generally assumed and used in this manuscript for ultrasound image formation.

1.2.1 Received signal

Based on the physical principle of wave propagation and equation, Ng. et. al. [Ng06, NPK+06] introduced a linear model for ultrasound image formation. More precisely, under the first order Born approximation and the weak scattering condition classically assumed for soft tissues, the received signal is the scattered pressure field integrated over the transducer surface, convolved with the transducer electromechanical impulse response [Ng06, NPK+06]. The final expression of the received signal/pressure field in the time domain is a linear model given by

$$r(\mathbf{r}_0, t) = h(\mathbf{r}, t) \circledast f_m(\mathbf{r})|_{\mathbf{r}=\mathbf{r}_0}, \tag{1.11}$$

where $\circledast$ is the two dimensional convolution operator, $\mathbf{r}_0$ is the transducer surface, $\mathbf{r}$ is the location of the scatterer/tissue of interest, the term $f_m(\mathbf{r})$ is commonly referred as tissue reflectivity function

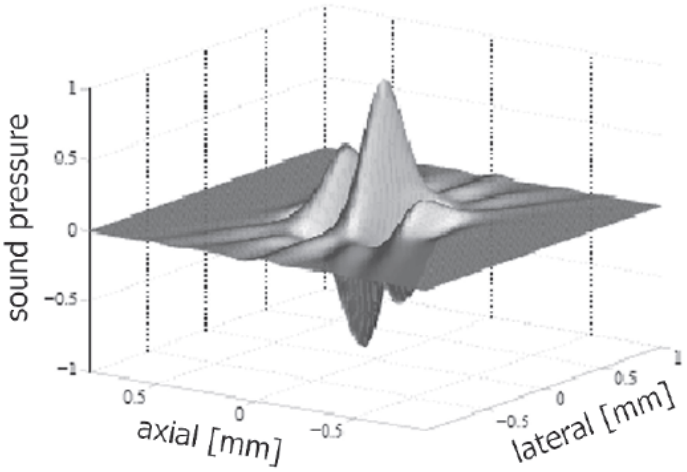

Figure 1.14: Point spread function of an electronically focused array at the focal point [LCR07].

(TRF) which accounts for the inhomogeneities of in the tissue due to density and propagation velocity perturbations, $h(\mathbf{r},t) = v_{pe}(\mathbf{r},t) \circledast h_{pe}(\mathbf{r},t)$ is the system point spread function (PSF) which combines the electromechanical response $v_{pe}(\mathbf{r},t)$ and the pulse-echo impulse response $h_{pe}(\mathbf{r},t)$. Note that h_{pe} relates the transducer geometry to the spatial extent of the scattered field [Ng06, NPK+06].

1.2.2 Point spread function

The ultrasound PSF plays an important role in ultrasound imaging system. It describes the imaging system response to a point input, and it must be derived for an accurate deconvolution. An important property of the PSF is its spatial variability. Methods allowing this variability to be handled are proposed in [Ale10]. The PSF depends on factors including the ultrasound system and the medium. Among the factors, the shape of the system PSF is mainly relative with the transducer and beamforming. As mentioned above, the most common beamforming technique is represented by static single focus beamforming (shown in Fig. 1.11), where the time delay of transducer elements and the apodization techniques can be designed to affect the focalization. The shape of the PSF at the focal point is displayed in Fig. 1.14. It is also interesting to note that the beamforming techniques can change the shape of the PSFs, as shown in Fig. 1.15. The differences between the PSFs in Fig.

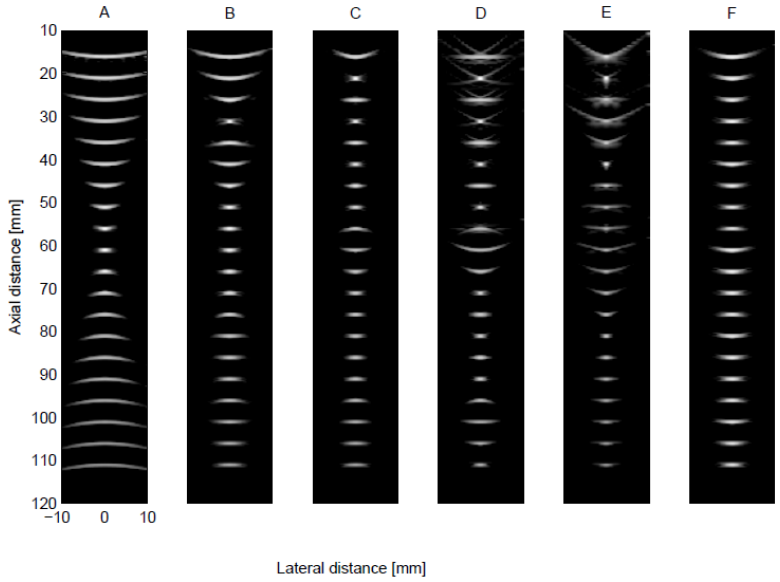

Figure 1.15: Point spread function phantom simulated using the Field II software [Jen96]. Different apodization and focolization are employed in each image.

1.15 are due to the different apodizations and focalizations. Finally, it is interesting to mention that the complicated dynamic beamforming techniques have been developed in order to have the most uniform PSFs on the imaged plane.

As stated in the previous ultrasound image presentation, the main limitation of ultrasound images is the poor image quality. Even though the device-based techniques have been carried out during last 20 years to improve ultrasound image visualization, many challenges on ultrasound imaging remain, e.g., restoration, resolution enhancement, segmentation, etc. Thus, some post-processing methods to improve the ultrasound image quality are prensented in the next section.

1.3 Post-processing techniques in ultrasound imaging

1.3.1 Introduction to inverse problems

An inverse problem is the process of calculating parameters from a set of observations: for example, calculating an image in CT, source reconstructing in acoustic, etc. In other words, it starts with

the results and then calculates the causes. Inverse problems most often do not fulfill Hadamard's postulates of well-posedness: they might not have a solution in the strict sense, solutions might not be unique or might not depend continuously on the data (stability). Moreover, even if a problem is well-posed, it may still be ill-conditioned, i.e., the condition number may be too large. In these cases, a traditional technique is to consider regularization/penalty terms or prior information to regularize the ill-posed/ill-conditioned problem to a well-posed/well-conditioned problem. Usually, the regularization term is related with the prior information about the parameters to be estimated.

In this part, several widely studied post-processing techniques for ultrasound images are reported, including speckle reduction, image deconvolution, image segmentation and image super-resolution. All these problems deal with parameter estimation given the observation. In this sense, they belong to the class of inverse problems.

1.3.2 Speckle reduction

Speckle noise is a well known inherent phenomenon in most B-mode US images due to the constructive and destructive interferences of backscattered echoes from the scatterers that are much smaller than the wavelength. Speckle noise leads to a granular pattern on the imaged tissue structures, which generally obscure fine anatomic details. Even though speckle reduction was not studied in detail in this manuscript, it is an important post-processing technique for medical US images. In the context of speckle reduction using post-processing techniques, speckle noise is widely assumed to be multiplicative [MT06, GCTZ09]. Thus, the logarithm transform is typically conducted to convert the multiplicative speckle noise into additive noise. A review of speckle reduction methods for cardiac ultrasound B-mode images can be found in [Per16]. However, it is interesting to note that even if speckle noise can be considered as multiplicative noise, it is also a source of information that can be exploited for speckle tracking and tissue characterization.

1.3.3 Image deconvolution

Linear image formation model

As a consequence of the linear model in (1.11), US images can be modelled as the convolution between a blurring kernel/PSF and a tissue reflectivity function. The resulting linear model can be rewritten as below

$$y(\mathbf{r}) = h(\mathbf{r}) \circledast x(\mathbf{r}) + n(\mathbf{r}), \quad \mathbf{r} \in \mathcal{R} \tag{1.12}$$

where $y(\mathbf{r})$ is the observed image pixel at the location $\mathbf{r}$, $x(\mathbf{r})$ is the TRF to be estimated, $h(\mathbf{r})$ is the system PSF, $n(\mathbf{r})$ is an additive noise due to the measurement and $\mathcal{R}$ is the image domain. Equivalently, after lexicographical ordering the corresponding images $y(\mathbf{r})$, $x(\mathbf{r})$, $n(\mathbf{r})$ and forming the huge matrix $\mathbf{H} \in \mathbb{R}^{N \times N}$ associated with $h(\mathbf{r})$, we obtain the following equivalent model

$$\mathbf{y} = \mathbf{H}\mathbf{x} + \mathbf{n}. \tag{1.13}$$

PSF estimation

Given the linear image model mentioned above, the PSF of an ultrasound system is unknown in practice. In an ultrasound image deconvolution framework, the estimation of the PSF is one of the key problems. The PSF is shift variant along the axial direction due to the physical reasons, e.g., attenuation, scattering. In this case, US images are generally divided into several local regions along the axial direction. In each region, the local PSF is assumed shift-invariant. The global blurring matrix is built in this case by combining these local shift-invariant PSFs [NPK+07, MA05, AMP+11, NO98]. Moreover, due to the development of recent beamforming techniques, it is often reasonable to assume a shift invariant PSF. Thus, we explore the existing methods for ultrasound PSF estimation under the assumption that PSF is shift invariant in this manuscript. Moreover, under the cyclic boundary condition, the PSF is block circulant with circulant blocks (BCCB). Then the product of $\mathbf{H}\mathbf{x}$ can be efficiently computed via Fast Fourier Transform (FFT). Details about the structure of $\mathbf{H}$ are given in Appendix A of this manuscript.

- Homomorphic technique:

  One of the most widely implemented technique is the homomorphic technique proposed in

[Opp65]. In a noise free case (ignoring the additive noise corrupting the measurements), the linear model (1.12) in the frequency domain is given by

$$Y(\boldsymbol{\omega}) = X(\boldsymbol{\omega})H(\boldsymbol{\omega}) \tag{1.14}$$

where $Y(\boldsymbol{\omega})$, $X(\boldsymbol{\omega})$ and $H(\boldsymbol{\omega})$ are the Fourier transforms of $y(\mathbf{r})$, $x(\mathbf{r})$ and $h(\mathbf{r})$ and $\boldsymbol{\omega}$ represent the location of images in the frequency domain. Particularly, it has been observed in numerous studies that the log-spectrum $\log|H|$ is regular and slow-varying function, while $\log|X|$ appears to be broadband and "spiky", see Fig. 1.16. Thus, it is possible to separate the PSF and the reflectivity function using homomorphic techniques, whose basic idea is to transform the product of two functions into the sum of two other functions. This separation is conducted in the cepstrum[1] domain. Precisely, the complex logarithmical transformation $\hat{Y}$ of the observation $Y(\boldsymbol{\omega})$ is given by

$$\begin{aligned}\hat{Y}(\boldsymbol{\omega}) &= \log|Y(\boldsymbol{\omega})| + i\angle Y(\boldsymbol{\omega}) \\ &= \log|X(\boldsymbol{\omega})| + \log|H(\boldsymbol{\omega})| + i\{\angle X(\boldsymbol{\omega}) + \angle H(\boldsymbol{\omega})\}\end{aligned} \tag{1.15}$$

where $|\cdot|$ and $\angle$ stand for the magnitude and phase of the complex signals. Considering the real parts (denoted as **Re**) and the imaginary parts (denoted as **Im**) separately, (1.15) implies the following relationships

$$\mathbf{Re}: \log|Y((\boldsymbol{\omega}))| = \log|X((\boldsymbol{\omega}))| + \log|H((\boldsymbol{\omega}))| \tag{1.16}$$

$$\mathbf{Im}: \angle Y((\boldsymbol{\omega})) = \angle X((\boldsymbol{\omega})) + \angle H((\boldsymbol{\omega})). \tag{1.17}$$

It has been shown that the energy of the PSF is confined at the first samples in the cepstrum domain, while the energy of the reflectivity function is spread over the entire cepstrum domain, see Fig. 1.16. Thus, the estimation of the PSF amplitude can be achieved by truncation in the cepstrum domain. However, the phase estimation is not obvious since it is wrapped, i.e.,

$$-\pi \leq \mathbf{W}\{\angle Y\} \leq \pi \tag{1.18}$$

[1]The cepstrum is the result of the inverse Fourier transform (IFT) of the logarithm of the spectrum (Fourier transform) of a signal

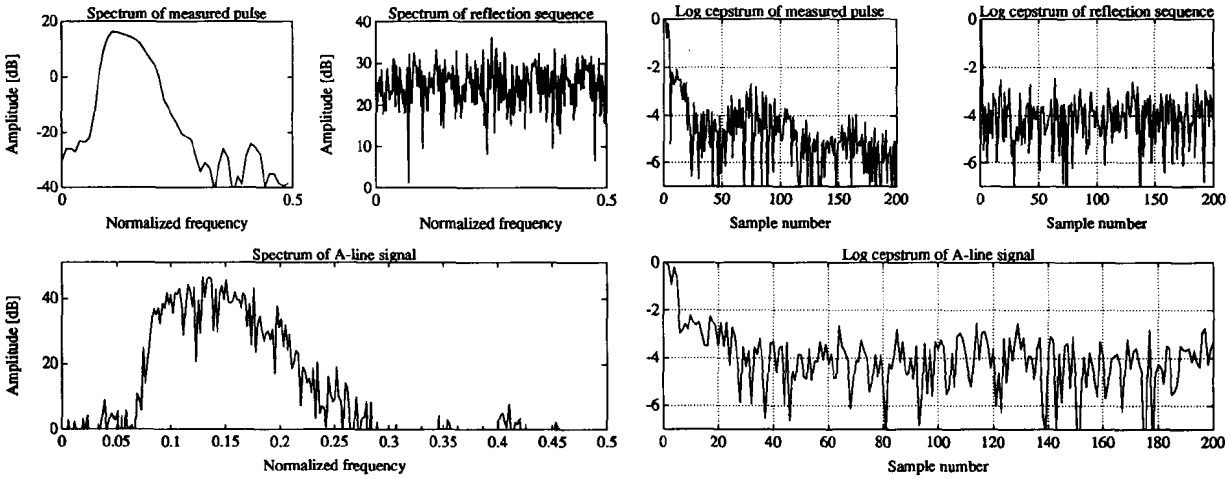

Figure 1.16: Spectrum (left) and log cepstrum (right) of measured PSF and sythetic reflectivity function for an A-line signal. The two images are extracted from [JL94].

where $\mathbf{W}$ is a wrapping operator. In the traditional homomorphic technique, it is possible to estimate the phase using the minimum phase assumption (see [JL94] for more details).

- Generalized homomorphic technique:

  Compared with the traditional homomorphic method, the generalized homomorphic technique explores wavelet-based denoising methods/wavelet filtering to estimate the amplitude [Tax95, BML12]. In order to estimate the phase of the PSF, a variety of phase unwrapping techniques have been developed for ultrasound PSF in the literature, see e.g., [MA01, MA03]. It is also interesting to note that the inverse filtering techniques can avoid the wrapped phase problem (see [MT07] for details).

Non-blind image deconvolution

US image deconvolution aims at estimating the TRF $\mathbf{x}$ from the RF data $\mathbf{y}$ using the linear model (1.13). A review of ultrasound image deconvolution can be found in [MA07]. US image deconvolution is a typical ill-posed problem. Imposing a regularization constraint is one traditional way to cope with this problem. Given the image formation model in (1.13), the image deconvolution problem can

be formulated as the following optimization problem

$$\min_{\mathbf{x}} \underbrace{f(\mathbf{y}-\mathbf{H}\mathbf{x})}_{\text{data fidelity}} + \quad \tau \quad \underbrace{g(\mathbf{x})}_{\text{regularization}} \tag{1.19}$$

where $f(\mathbf{y}-\mathbf{H}\mathbf{x})$ is the data fidelity term, i.e., the likelihood of the observations, related to the noise distribution, $g(\mathbf{x})$ is the regularization constraint, which usually reflects the prior knowledge about $\mathbf{x}$ and τ is the regularization parameter which weights the importance between the data fidelity term and the regularization term. Given an additive white Gaussian noise (AWGN), the data fidelity term can be rewritten as

$$f(\mathbf{y}-\mathbf{H}\mathbf{x}) = \frac{1}{2}\|\mathbf{y}-\mathbf{H}\mathbf{x}\|_2^2 \tag{1.20}$$

where $\|\cdot\|_2$ stands for the standard ℓ_2-norm. In US imaging, Gaussian and Laplacian distributions have been widely explored as prior information for the TRF $\mathbf{x}$, leading to ℓ_2-norm [JT08] and ℓ_1-norm [MT07], [YZX12a] constrained optimization problems.

- ℓ_2-norm regularized deconvolution

  Considering Gaussian prior for the TRF $\mathbf{x}$ and an AWGN, the image deconvolution problem can be rewritten as

  $$\min_{\mathbf{x}} \frac{1}{2}\|\mathbf{y}-\mathbf{H}\mathbf{x}\|_2^2 + \tau\|\mathbf{x}\|_2^2. \tag{1.21}$$

  The analytical solution of (1.21) can be implemented in the frequency domain, i.e.,

  $$X(\omega_1,\omega_2) = \frac{Y(\omega_1,\omega_2)H^H(\omega_1,\omega_2)}{|H(\omega_1,\omega_2)|^2+\tau} \tag{1.22}$$

  where $\cdot^H$ denotes the complex conjugate. This type of deconvolution is well known as Wiener filtering [ZWZ97].

- ℓ_1-norm regularized deconvolution

  Given AWGN and Laplacian prior for the TRF, we obtain the following image deconvolution problem

  $$\min_{\mathbf{x}} \frac{1}{2}\|\mathbf{y}-\mathbf{H}\mathbf{x}\|_2^2 + \tau\|\mathbf{x}\|_1 \tag{1.23}$$

The cost function in (1.23) is non-differential, thus the traditional gradient-based algorithms cannot be considered directly. However, the variable splitting based algorithms developed for non-differential problems such as the alternating direction method of multipliers (ADMM) [BPC+11a], the forward-backward algorithm (FBA) [CP11], the fast iterative shringkage-thresholding algorithm (FISTA) [BT09], etc. can be employed.

- Total variation regularized deconvolution

  Total variation (TV) is widely used in image processing as a prior due to its good properties for edge preservation [NWY10, MBK12]. In order to give its definition, we first introduce the gradient operators $\nabla\mathbf{x}$, where $\nabla := [\partial_{\mathrm{h}}, \partial_{\mathrm{v}}]^T$ and ∂_{h} and ∂_{v} are the horizontal and vertical gradients. For an image $\boldsymbol{x} \in \mathbb{R}^{m\times n}$, under the periodic boundary conditions, the numerical definitions of the gradient operators are

$$(\partial_{\mathrm{h}}\boldsymbol{x})(i,j) = \begin{cases} \boldsymbol{x}(i+1,j) - \boldsymbol{x}(i,j) & \text{if } i < m \\ \boldsymbol{x}(m,j) - \boldsymbol{x}(1,j) & \text{if } i = m \end{cases} \tag{1.24}$$

$$(\partial_{\mathrm{v}}\boldsymbol{x})(i,j) = \begin{cases} \boldsymbol{x}(i,j+1) - \boldsymbol{x}(i,j) & \text{if } j < n \\ \boldsymbol{x}(i,n) - \boldsymbol{x}(i,1) & \text{if } j = n. \end{cases} \tag{1.25}$$

  The gradient operators can be rewritten as two matrices $\mathbf{D}_{\mathrm{h}}$ and $\mathbf{D}_{\mathrm{v}}$ corresponding to the horizontal and vertical discrete differences of an image, respectively. Using these notations, the TV prior can be defined as

$$\|\mathbf{x}\|_{\mathrm{TV}} = \sqrt{\|\partial_{\mathrm{h}}\mathbf{x}\|^2 + \|\partial_{\mathrm{v}}\mathbf{x}\|^2} = \sqrt{\|\mathbf{D}_{\mathrm{h}}\mathbf{x}\|^2 + \|\mathbf{D}_{\mathrm{v}}\mathbf{x}\|^2}. \tag{1.26}$$

  Given the TV prior and under the assumption of AWGN, we can rewrite the image deconvolution problem as (1.27), which involves a nondifferential cost function.

$$\min_{\mathbf{x}} \frac{1}{2}\|\mathbf{y} - \mathbf{H}\mathbf{x}\|_2^2 + \tau\|\mathbf{x}\|_{\mathrm{TV}}. \tag{1.27}$$

  The methods that have been proposed to tackle problem (1.27) include the variable splitting algorithms such as the ADMM, FBA, primal-dual algorithms [CCC+10], etc.

In addition to these traditional image priors considered for US images, different kinds of priors depending on the type of applications have been studied. For instance, generalized Gaussian distributions have been used for tissue characterization in [AMP+11], for joint US image deconvolution and segmentation in [ZBKT16] and for US image compressed sensing in [CZBK15]. The Huber model is proposed in [MR15] as a prior information for US image deconvolution. The Rayleigh distribution has been explored for US image segmentation in [PDBT12].

1.3.4 Image segmentation

Image segmentation aims at partitioning an image into multiple regions or categories. More precisely, image segmentation is the process of assigning a label to every pixel in an image such that pixels with the same label share certain characteristics, e.g., color, intensity, motion or texture. Segmentation can be used for object recognition or the locating of object boundaries in a variety of applications.

The image segmentation problem can be formulated in Bayesian or variational frameworks. There are three general approaches for segmentation, i.e., thresholding, edge-based methods and region-based methods [GH95, Wan09].

- Thresholding: Thresholding techniques are the simplest image segmentation methods, where histogram thresholding may be applied to an image directly or combined with pre/post processing techniques. Several popular methods are commonly used including the maximum entropy method, the maximum variance method [Ots79, SS04], or k-means clustering [AV07].

- Edge-based methods: With these techniques, the edges of images, which are assumed to be the object boundaries, are detected in order to identify the objects of interest. The edge-based methods range from the simple methods based on edge detection (e.g., gradient operators, Hilbert transform [PD03]) to more sophisticated methods based on watershed segmentation [VS91].

- Region-based methods: Generally, region-based techniques are based on the assumption that the neighboring pixels within one region have similar attributes. The aim of region detection is to provide the possibility to characterize the detected object by parameter analysis (shape,

position, size, etc.). The region-based methods can be roughly categorized into region merging, region splitting and region growing schemes [SDR10].

Segmentation techniques in ultrasound imaging

Since ultrasound images suffer from a relatively low data quality caused by attenuation, speckle and shadows, the methods used in literature exploit specific constraints or priors. Some widely used constraints include the intensity based priors, geometric priors or the statistical analysis of the ultrasound images. A variety of segmentation methodologies developed for medical US images have embedded these constraints into Bayesian approaches, active contours, active appearance models, level-sets, machine learning, clustering or graph based frameworks. In addition, it is interesting to note that most of the segmentation methods are developed for the traditional B-mode ultrasound images. A review of US image segmentation methods until 2006 can be found in [NB06]. Other interesting reviews on US image segmentation until 2010 are [Nob10, SDR10]. It is also important to note that for specific clinical applications including breast, carotid, prostate, ventricle, etc., different segmentation methods should be considered to obtain satisfying segmentation performances. For instance, an evaluation platform for left ventricle segmentation in 3D echocardiography has been conducted in [BHA+14]. A review of the breast cancer detection and segmentation methods can also be found in [CSJ+10].

Bayesian algorithms: Pereyra et. al. proposed a Bayesian method based on the statistical analysis (mixture of α-Rayleigh distributions) of B-mode ultrasound images [Per12]. Precisely, a Markov chain Monte Carlo (MCMC) method was investigated to jointly estimate the mixture parameters and a label map associated with the US image pixels. In this thesis, we will study a similar framework to ultrasound RF images. Note that the statistical analysis of RF images (mixtures of generalized Gaussian distributions) were also studied in [Ale10]. More detailed explanations about this Bayesian framework for ultrasound image segmentation will be presented in Chapter 2.

1.3.5 Single image super-resolution

Single image super-resolution (SR), also known as image scaling up or image enhancement, aims at estimating a high-resolution (HR) image from a low-resolution (LR) observed image [PPK03]. This resolution enhancement problem is still an ongoing research problem with applications in various fields, such as remote sensing [MBD15], video surveillance [YH10], hyperspectral [AAM05], microwave[YLTV15] or medical imaging [MBK12].

In the single image SR problem, the observed LR image is modeled as a noisy version of the blurred and decimated HR image (to be estimated) as follows,

$$\mathbf{y} = \mathbf{SHx} + \mathbf{n} \tag{1.28}$$

where the vector $\mathbf{y} \in \mathbb{R}^{N_l \times 1}$ ($N_l = m_l \times n_l$) denotes the LR observed image and $\mathbf{x} \in \mathbb{R}^{N_h \times 1}$ ($N_h = m_h \times n_h$) is the vectorized HR image to be estimated, with $N_h > N_l$. The vectors $\mathbf{y}$ and $\mathbf{x}$ are obtained by stacking the corresponding images (LR image $\in \mathbb{R}^{m_l \times n_l}$ and HR image $\in \mathbb{R}^{m_h \times n_h}$) into column vectors in a lexicographic order. Note that the vector $\mathbf{n} \in \mathbb{R}^{N_l \times 1}$ is an independent identically distributed (*i.i.d.*) additive white Gaussian noise (AWGN) and that the matrices $\mathbf{S} \in \mathbb{R}^{N_l \times N_h}$ and $\mathbf{H} \in \mathbb{R}^{N_h \times N_h}$ represent the decimation and the blurring/convolution operations respectively. More specifically, $\mathbf{H}$ is a block circulant matrix with circulant blocks, which corresponds to cyclic convolution boundaries, and left multiplying by $\mathbf{S}$ performs down-sampling with an integer factor d ($d = d_r \times d_c$), i.e., $N_h = N_l \times d$. The decimation factors d_r and d_c represent the numbers of discarded rows and columns from the input images satisfying the following relationships $m_h = m_l \times d_r$ and $n_h = n_l \times d_c$. Note that the image formation model (3.1) has been widely considered in single image SR problems, see, e.g., [YWHM10, SSXS08, SSXS11, NWY10, ZGTL12].

The methods dedicated to single image SR can be classified into three categories [YWHM10, SSXS08, TLBL10].

- Interpolation-based approaches

  The first category includes the interpolation-based algorithms using nearest neighbor interpolation, bicubic interpolation [TBU00] or adaptive interpolation techniques [ZW08, MY10].

Despite their simplicity and easy implementation, it is well-known that these algorithms generally over-smooth the high frequency details.

- Learning-based approaches

  The second type of methods consider learning-based (or example-based) algorithms that learn the relations between LR and HR image patches from a given database [FPC00, GBI09, HSA15, ZEP12, YWHM10]. Note that the effectiveness of the learning-based algorithms highly depends on the training image database and these algorithms have generally a high computational complexity.

- Reconstruction-based approaches

  Reconstruction-based approaches that are considered in this manuscript belong to the third category of SR approaches [SSXS08, SSXS11, TLBL10, NWY10]. These approaches formulate the image SR as a reconstruction problem, either by incorporating priors in a Bayesian framework or by introducing regularizations into the ill-posed inverse problem. Also, the traditional image priors presented above for the deconvolution problems can be implemented for the single image SR problems.

This PhD thesis will concentrate on the reconstruction-based methods for single image SR due to its efficiency in terms of computational time. Note also that there are limited works on single image SR in ultrasound imaging, while multi-frame image SR is studied more widely. Among the existing methods for single image SR, [MBK12] proposed to solve the problem in an ADMM framework for US imaging. In this thesis, we have developed a general method which is valid for both ultrasound and natural images is developed (see Chapter 3).

1.4 Conclusion

This chapter presented some background about medical ultrasound imaging, ranging from the physic principle to the linear image formation model. Also, several widely considered post-processing techniques have been discussed allowing ultrasound image quality to be improved. These post-processing

techniques, include speckle reduction, image deconvolution, image segmentation and single image super-resolution that can be formulated as ill-posed problems. The aim of this thesis is to study new post-processing methods for ultrasound images.

Chapter 2

Joint deconvolution and segmentation of ultrasound images

Part of this chapter has been adapted from the journal paper [ZBKT16] and the conference paper [ZBKT14].

Contents

2.1 Introduction 38
2.1.1 Problem Statement 38
2.1.2 Related Work 39
2.1.3 Proposed method 40
2.2 Bayesian Model for Joint Deconvolution and Segmentation 40
2.2.1 Likelihood 42
2.2.2 Prior Distributions 42
2.2.3 Joint posterior distribution 44
2.3 Sampling the posterior and computing the Bayesian estimators 44
2.3.1 Hybrid Gibbs sampler 45
2.3.2 Parameter estimation 48
2.3.3 Computational complexity analysis 49
2.4 Experimental results 49
2.4.1 Evaluation metrics 49
2.4.2 Sampler convergence 51
2.4.3 Computational complexity 52
2.4.4 Synthetic data 52
2.4.5 Joint Deconvolution and Segmentation 55
2.5 Conclusions 68

2.1 Introduction

Ultrasound imaging is a well-established medical imaging modality widely used for clinical diagnosis, visualization of anatomical structures, tissue characterization and blood flow measurements. The popularity of US imaging compared to other imaging modalities such as computed tomography (CT) or magnetic resonance imaging (MRI) is mainly due to its efficiency, low cost and safety [Dha11]. Despite these advantages and the recent advances in instrumentation [TF14a] and beamforming [RAHA14], it also has some limitations, mainly related to its poor signal-to-noise ratio, limited contrast and spatial resolution. Furthermore, US images are characterized by speckle, which considerably reduces their quality and may lead to interpretation issues. For this reason, several despeckling methods can be found in the US literature [GK15, MT06]. Despite its negative effect, speckle has also been extensively used as a source of information in applications such as image segmentation and tissue characterization [NB06, PDBT12]. Specifically, it has been shown that the statistical properties of the speckle are strictly correlated with the tissue structures [AMP+11, Sza04]. Thus, methods allowing image restoration using the statistical properties of the speckle noise are also an interesting research track in US imaging [NPK+07, AMP+11].

2.1.1 Problem Statement

As stated in Chapter 1, RF ultrasound image formation can be modeled using the following linear model

$$\mathbf{y} = \mathbf{H}\mathbf{x} + \mathbf{n}. \tag{2.1}$$

where the vectors $\mathbf{y}$, $\mathbf{x}$ and $\mathbf{n}$ are the TRF to be estimated, the observed RF ultrasound image and the measurement noise respectively, the huge matrix $\mathbf{H} \in \mathbb{R}^{N\times N}$ is associated with the system PSF. Due to the physical corrections related to image formation (e.g., time gain compensation, dynamic beamforming), in most of soft tissues, $\mathbf{H}$ can be assumed shift invariant. Moreover, cyclic convolution is considered in this manuscript for computational purpose, leading to a block circulant matrix of circulant blocks (BCCB) $\mathbf{H}$[1]. Note that the PSF is unknown in practical applications and that its

[1]Some existing works [NPK+07, MA05, AMP+11, NO98] assume that the PSF in US imaging is shift-variant mainly along the axial direction. In this case, US images are generally divided into several local regions along the axial direction.

estimation has been extensively explored in US imaging. A typical approach in US imaging, also adopted in this manuscript, is to estimate the PSF in a pre-processing step before applying the deconvolution algorithm (see, e.g., [AMP+11, JMGS93]).

2.1.2 Related Work

US image deconvolution aims at estimating the TRF $\mathbf{x}$ from the RF data $\mathbf{y}$, which is a typical ill-posed problem. Imposing a regularization constraint is one traditional way to cope with this problem. The regularization constraint usually reflects the prior knowledge about $\mathbf{x}$. In US imaging, Gaussian and Laplacian distributions have been widely explored as prior information for the TRF $\mathbf{x}$, leading to ℓ_2-norm [JT08] and ℓ_1-norm [MT07], [YZX12a] constrained optimization problems.

Due to the tight relationship between image deconvolution and segmentation, it is interesting to consider these two operations jointly. This idea has been recently exploited for piecewise homogeneous images using the Mumford-Shah model [BSK04, BCC+11, CYZ14], the Potts model [AMD10, SWFU15] or the generalized linear models [PCS13] in Bayesian or variational frameworks. Moreover, segmentation-based regularizations have been considered in [Mig06] to improve the image reconstruction performance. However, due to the intrinsic granular appearance of US data, these methods are not always efficient to simultaneously restore and segment US images. In order to develop US image deconvolution and segmentation methods, it is common to take advantage of the statistical properties of the TRF. Except the traditional Gaussian and Laplace distributions mentioned above, distributions that have been considered for US images include the homodyned K [HO09], Nakagami [LN11] and generalized Gaussian distributions [BTDF07]. In particular, Alessandrini *et. al.* recently investigated a deconvolution method for US images based on generalized Gaussian distributions (GGDs) using the expectation maximization (EM) algorithm [APMS11, AMP+11]. This method assumed that the US image can be divided into different regions characterized by GDDs with different parameters. Despite its accuracy when compared to several state-of-the-art US image deconvolution methods, the framework in [APMS11] has two major drawbacks that we propose to tackle in this

In each region, the local PSF is assumed shift-invariant. The global blurring matrix is built in this case by combining these local shift-invariant PSFs.

chapter. First, it is well-known that the EM algorithm can easily converge to a local minimum of the cost function and is sensible to the initial values of the parameters to be tuned, which may lead to inaccurate estimates. Second, the EM algorithm can only be applied to cases where a mask (or label map) of the homogeneous regions is available. Note that a US image deconvolution method based on Markov chain Monte Carlo (MCMC) methods was recently investigated in [ZBKT14]. However, the proposed method also required an *a priori* label map for the different image regions. Due to the tight relationships between segmentation and deconvolution, we think that combining these two operations can increase their performance, which is the objective of this chapter.

2.1.3 Proposed method

Compared with the US image deconvolution method of [ZBKT14], this chapter defines a Potts Markov random field for the hidden image labels, assigns GGD priors to the image TRF, and investigates a joint segmentation and deconvolution method for US images. Thus, the proposed algorithm generalizes the results of [ZBKT14] to situations where a label map is unknown. Additional motivations for the proposed model are provided below. First, it uses a GGD-Potts model to regularize the ill-posed joint deconvolution and segmentation problem. Second, it exploits the local statistical properties of different image regions, which are usually related with the anatomical image structures. Finally, the proposed model is able to capture the spatial correlations between neighboring pixels. To our knowledge, the proposed method represents a first attempt for a joint segmentation and deconvolution in US imaging. The complicated form of the resulting posterior distribution makes it too difficult to compute closed form expressions of the corresponding Bayesian estimators. Therefore, a Markov chain Monte Carlo (MCMC) method based on a Gibbs sampler is investigated to sample the posterior distribution of interest and build the estimators of its unknown parameters.

2.2 Bayesian Model for Joint Deconvolution and Segmentation

This section introduces the Bayesian model investigated in this chapter for the joint deconvolution and segmentation of US images. We assume that the US TRF $\mathbf{x} = (x_1, \cdots, x_N)^T$ can be divided into

K statistical homogeneous regions, denoted as $\{\mathcal{R}_1, ..., \mathcal{R}_K\}$ and we introduce a hidden label field $\mathbf{z} = (z_1, \cdots, z_N)^T \in \mathbb{R}^N$ mapping the image into these K regions. More precisely, $z_i = k$ if and only if the corresponding pixel x_i belongs to the region $\mathcal{R}_k$, where $k \in \{1, \cdots, K\}$ and $i \in \{1, \cdots, N\}$. The conditional distribution of pixel x_i is then defined as

$$x_i | z_i = k \sim \mathcal{GGD}(x_i; \xi_k, \gamma_k) \tag{2.2}$$

where ξ_k and γ_k are the shape and scale parameters of the GGD associated with the region $\mathcal{R}_k$. We remind that a univariate GGD with shape parameter ξ and scale parameter γ denoted as $\mathcal{GGD}(\xi, \gamma)$ has the following pdf

$$p_{\text{GGD}}(x) = \frac{1}{2\gamma^{1/\xi}\Gamma(1 + 1/\xi)} \exp\left(-\frac{|x|^\xi}{\gamma}\right), \quad x \in \mathbb{R}. \tag{2.3}$$

Assuming that the pixels are independent conditionally to the knowledge of their classes, the TRF is distributed according to a mixture of GGDs with the following probability density function (pdf)

$$p(x_i) = \sum_{k=1}^{K} w_k \mathcal{GGD}(x_i; \xi_k, \gamma_k) \text{ with } w_k = P(z_i = k). \tag{2.4}$$

In addition, we assign a Potts model to the hidden field $\mathbf{z}$ to exploit the dependencies between pixels that are nearby in the image [AMD10, PDBT12, PDBT13]. The resulting model is referred to as GGD-Potts model. In the following, we define a hierarchical Bayesian model based on this GGD-Potts model for the joint segmentation and deconvolution of US images. Using the Bayes rule for the joint posterior of the unknown parameters, the following result can be obtained

$$p(\mathbf{x}, \mathbf{z}, \boldsymbol{\theta} | \mathbf{y}) \propto p(\mathbf{y} | \mathbf{x}, \boldsymbol{\theta}) p(\mathbf{x} | \mathbf{z}, \boldsymbol{\theta}) p(\mathbf{z} | \boldsymbol{\theta}) p(\boldsymbol{\theta}) \tag{2.5}$$

where $\propto$ means "proportional to", $\boldsymbol{\theta}$ is a parameter vector containing all the model parameters and hyperparameters except $\mathbf{x}$ and $\mathbf{z}$, *i.e.,* the noise variance, the shape and scale parameters. The likelihood $p(\mathbf{y}|\mathbf{x}, \boldsymbol{\theta})$ depending on the noise model and the prior distributions $p(\mathbf{x}|\mathbf{z}, \boldsymbol{\theta})$, $p(\mathbf{z}|\boldsymbol{\theta})$ based on the GGD-Potts model are detailed hereinafter.

2.2.1 Likelihood

Assuming an additive white Gaussian noise (AWGN) with a constant variance σ_n^2, the likelihood function associated with the linear model (2.1) is

$$p(\mathbf{y}|\mathbf{x},\sigma_n^2) = \frac{1}{(2\pi\sigma_n^2)^{N/2}}\exp\left(-\frac{1}{2\sigma_n^2}\|\mathbf{y}-\mathbf{H}\mathbf{x}\|_2^2\right) \tag{2.6}$$

where $\|\cdot\|_2$ is the Euclidean ℓ_2-norm.

2.2.2 Prior Distributions

Tissue reflectivity function (TRF) x

As explained beforehand, a mixture of GGD priors is assigned to the TRF. Assuming that the pixels are independent conditionally to the knowledge of their classes, we obtain the following prior for the target image

$$\begin{aligned} p(\mathbf{x}|\mathbf{z},\boldsymbol{\xi},\boldsymbol{\gamma}) &= \prod_{k=1}^{K}\prod_{i=1}^{N_k}\frac{1}{2\gamma_k^{1/\xi_k}\Gamma(1+1/\xi_k)}\exp\left(-\frac{|x_i|^{\xi_k}}{\gamma_k}\right) \\ &= \prod_{k=1}^{K}\frac{1}{\left[2\gamma_k^{1/\xi_k}\Gamma(1+1/\xi_k)\right]^{N_k}}\exp\left(-\frac{\sum_{i=1}^{N_k}|x_i|^{\xi_k}}{\gamma_k}\right) \\ &= \prod_{k=1}^{K}\frac{1}{\left[2\gamma_k^{1/\xi_k}\Gamma(1+1/\xi_k)\right]^{N_k}}\exp\left(-\frac{\|\mathbf{x}_k\|_{\xi_k}^{\xi_k}}{\gamma_k}\right) \end{aligned} \tag{2.7}$$

where $\boldsymbol{\xi} = (\xi_1,\cdots,\xi_K)^T$ and $\boldsymbol{\gamma} = (\gamma_1,\cdots,\gamma_K)^T$, ξ_k and γ_k are the shape and scale parameters of the kth region $\mathcal{R}_k$, N_k is the number of pixels in $\mathcal{R}_k$, $\mathbf{x}_k$ contains all the pixels assigned to $\mathcal{R}_k$, $\Gamma(\cdot)$ is the gamma function and $\|\mathbf{x}_k\|_\xi = (\sum_{i=1}^{N_k}|x_i|^\xi)^{1/\xi}$ denotes the ℓ_ξ-norm.

Noise variance σ_n^2

In the presence of an AWGN, it is standard to assign a conjugate inverse gamma ($\mathcal{IG}$) prior to the noise variance, i.e.,

$$\begin{aligned} p(\sigma_n^2) \sim& \mathcal{IG}(\alpha,\nu) \\ =& \frac{\nu^\alpha}{\Gamma(\alpha)}(\sigma_n^2)^{-\alpha-1}\exp\left(-\frac{\nu}{\sigma_n^2}\right)\mathcal{I}_{\mathbb{R}+}(\sigma_n^2) \end{aligned} \tag{2.8}$$

where $\mathcal{I}_A$ is the indicator function on the set A. This prior has two adjustable parameters α, ν which make it very flexible and thus appropriate to the variance of most statistical models. The values of α and ν have been fixed by cross validation in our experiments leading to $(\alpha, \nu) = (0.1, 0.1)$.

Labels z

A Potts model (generalization of the Ising model) is considered as prior for the hidden image label field. The Potts Markov random field (MRF) has been shown to be appropriate for image segmentation [MGM06, PDBT13]. It establishes dependencies between pixels that are nearby in an image [PDBT12, PDBT13]. More specifically, adjacent labels of the image are dependent and tend to belong to the same class. The conditional distribution of z_n (associated with pixel x_n) for the Potts MRF is defined as

$$p(z_n|\mathbf{z}_{-n}) = p(z_n|\mathbf{z}_{\mathcal{V}(n)}) \tag{2.9}$$

where $\mathbf{z}_{-n} = (z_1, ..., z_{n-1}, z_{n+1}, ..., z_N)$ and $\mathcal{V}(n)$ contains the neighbors of label z_n. In this manuscript, a first order neighborhood structure (i.e., 4 nearest pixels) is considered. The whole set of random variables $\mathbf{z}$ forms a random field.

Using the Hammersley-Clifford theorem [Bes74], the prior of $\mathbf{z}$ can be expressed as a Gibbs distribution, i.e.,

$$p(\mathbf{z}) = \frac{1}{C(\beta)} \exp\left[\sum_{n=1}^{N} \sum_{n' \in \mathcal{V}(n)} \beta\delta(z_n - z_{n'})\right] \tag{2.10}$$

where β is the granularity coefficient or smooth parameter, $\delta(\cdot)$ is the Kronecker function and $C(\beta)$ is the normalizing constant (often referred to as partition function). The value of β has been fixed by cross validation, leading to $\beta = 1$.

Shape and scale parameters

The prior used for the US TRF defined in (2.7) depends on the shape and scale parameters of the GGD, which are usually referred to as hyperparameters. Following the works in [CPT+10], we have

chosen the following priors for these hyperparameters

$$p(\boldsymbol{\xi}) = \prod_{k=1}^{K} p(\xi_k) = \prod_{k=1}^{K} \frac{1}{3}\mathcal{I}_{[0,3]}(\xi_k) \tag{2.11}$$

$$p(\boldsymbol{\gamma}) = \prod_{k=1}^{K} p(\gamma_k) = \prod_{k=1}^{K} \frac{1}{\gamma_k}\mathcal{I}_{\mathbb{R}+}(\gamma_k) \tag{2.12}$$

where $k \in \{1, ..., K\}$. Note that the range $[0, 3]$ covers all the possible values of ξ_k and that $p(\gamma_k)$ is the uninformative Jeffreys prior for γ_k.

2.2.3 Joint posterior distribution

The joint posterior distribution of the unknown parameters $\mathbf{x}, \sigma_n^2, \boldsymbol{\xi}, \boldsymbol{\gamma}, \mathbf{z}$ can be determined as follows

$$\begin{aligned}
p(\mathbf{x}, \sigma_n^2, \boldsymbol{\xi}, \boldsymbol{\gamma}, \mathbf{z}|\mathbf{y}) &\propto p(\mathbf{y}|\mathbf{x}, \sigma_n^2, \boldsymbol{\xi}, \boldsymbol{\gamma}, \mathbf{z}) p(\mathbf{x}, \sigma_n^2, \boldsymbol{\xi}, \boldsymbol{\gamma}, \mathbf{z}) \\
&\propto p(\mathbf{y}|\mathbf{x}, \sigma_n^2, \boldsymbol{\xi}, \boldsymbol{\gamma}, \mathbf{z}) p(\mathbf{x}|\boldsymbol{\xi}, \boldsymbol{\gamma}, \mathbf{z}) p(\sigma_n^2) \times p(\boldsymbol{\xi}) p(\boldsymbol{\gamma}) p(\mathbf{z}) \\
&\propto \frac{1}{(2\pi\sigma_n^2)^{N/2}} \exp\left(-\frac{1}{2\sigma_n^2}\|\mathbf{y} - \mathbf{H}\mathbf{x}\|_2^2\right) \times \frac{1}{(\sigma_n^2)^{\alpha+1}} \exp\left(-\nu/\sigma_n^2\right) \\
&\quad \times \prod_{k=1}^{K} \left\{ a_k^{N_k} \exp\left(-\frac{\|\mathbf{x}_k\|_{\xi_k}^{\xi_k}}{\gamma_k}\right) \times \exp\left[\sum_{n=1}^{N} \sum_{n' \in \mathcal{V}(n)} \beta\delta(z_n - z_{n'})\right] \right. \\
&\quad \left. \times \frac{1}{3}\mathcal{I}_{[0,3]}(\xi_k) \frac{1}{\gamma_k}\mathcal{I}_{\mathbb{R}+}(\gamma_k) \right\}
\end{aligned} \tag{2.13}$$

where $a_k = \frac{1}{2\gamma_k^{1/\xi_k}\Gamma(1+1/\xi_k)}$ and the hyperparameters are supposed to be *a priori* independent. Fig. 2.1 summarizes the proposed hierarchical Bayesian model as a directed acyclic graph (DAG), in which the relationships between the parameters and hyperparameters are indicated.

2.3 Sampling the posterior and computing the Bayesian estimators

Computing closed-form expressions of the MMSE or MAP estimators for the unknown parameters $\mathbf{x}, \sigma_n^2, \boldsymbol{\xi}, \boldsymbol{\gamma}, \mathbf{z}$ from (2.13) is clearly complicated. In this case, a possible solution is to consider MCMC methods in order to generate samples asymptotically distributed according to the distribution of interest and to use the generated samples to build estimators of the unknown parameters. In this

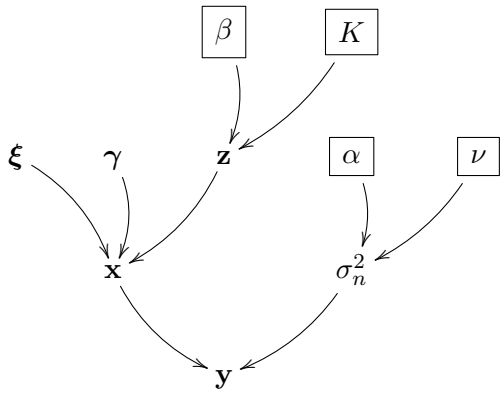

Figure 2.1: Hierarchical Bayesian model for the parameter and hyperparameter priors, where the TRF $\mathbf{x}$ is modeled by a mixture of GGDs, the hidden label field $\mathbf{z}$ follows a Potts MRF and the parameters appearing in the boxes are fixed in advance.

section, a hybrid Gibbs sampler is investigated to generate samples asymptotically distributed according to (2.13). These samples are used to compute the Bayesian estimators of the US TRF $\mathbf{x}$, hidden label field $\mathbf{z}$, noise variance σ_n^2 and GGD parameters $\boldsymbol{\xi}, \boldsymbol{\gamma}$.

2.3.1 Hybrid Gibbs sampler

The proposed hybrid Gibbs sampler is a 5-step algorithm summarized in Algorithm 1. The algorithm is explained in detail in what follows.

Algorithm 1: Hybrid Gibbs Sampler

1. Sampling the noise variance σ_n^2 according to the conditional distribution (2.14).
2. Sampling the shape parameter $\boldsymbol{\xi}$ according to the conditional distribution (2.16) with an RWMH algorithm.
3. Sampling the scale parameter $\boldsymbol{\gamma}$ using (2.18).
4. Sampling the labels $\mathbf{z}$ according to the normalized conditional distribution (2.22).
5. Sampling the TRF $\mathbf{x}$ using an HMC method.

Sampling the noise variance σ_n^2

The conditional distribution of $\sigma_n^2|\mathbf{y}, \mathbf{x}, \boldsymbol{\xi}, \boldsymbol{\gamma}, \mathbf{z}$ is the following inverse gamma distribution whose expression is derived in Appendix B.1

$$\begin{aligned} p(\sigma_n^2|\mathbf{y}, \mathbf{x}, \boldsymbol{\xi}, \boldsymbol{\gamma}, \mathbf{z}) &\propto p(\mathbf{y}|\mathbf{x}, \sigma_n^2, \boldsymbol{\xi}, \boldsymbol{\gamma}, \mathbf{z}) p(\sigma_n^2) \\ &= \mathcal{IG}\left(\alpha + N/2, \theta + \frac{1}{2}\|\mathbf{y} - \mathbf{H}\mathbf{x}\|_2^2\right). \end{aligned} \tag{2.14}$$

Generating samples according to (2.14) is straightforward.

Sampling the shape parameter vector $\boldsymbol{\xi}$

The conditional distribution of the shape parameter vector $\boldsymbol{\xi}$ satisfies the following relation

$$\begin{aligned} p(\boldsymbol{\xi}|\mathbf{y}, \mathbf{x}, \sigma_n^2, \boldsymbol{\gamma}, \mathbf{z}) &\propto p(\mathbf{y}|\mathbf{x}, \sigma_n^2, \boldsymbol{\xi}, \boldsymbol{\gamma}, \mathbf{z}) p(\mathbf{x}|\boldsymbol{\xi}, \boldsymbol{\gamma}, \mathbf{z}) p(\boldsymbol{\xi}) \\ &\propto p(\mathbf{x}|\boldsymbol{\xi}, \boldsymbol{\gamma}, \mathbf{z}) p(\boldsymbol{\xi}). \end{aligned} \tag{2.15}$$

Assuming that the shape parameters are *a priori* independent, we have

$$\begin{aligned} p(\xi_k|\mathbf{x}, \boldsymbol{\gamma}, \mathbf{z}, \boldsymbol{\xi}_{-k}) &\propto p(\mathbf{x}_k|\xi_k, \gamma_k, \mathbf{z}_k) p(\xi_k) \\ &\propto a_k^{N_k} \exp\left(-\frac{\|\mathbf{x}_k\|_{\xi_k}^{\xi_k}}{\gamma_k}\right) \mathcal{I}_{[0,3]}(\xi_k) \end{aligned} \tag{2.16}$$

where $\boldsymbol{\xi}_{-k} = (\xi_1, ..., \xi_{k-1}, \xi_{k+1}, ..., \xi_K)$ for $k \in \{1, ..., K\}$, $\mathbf{x}_k$ contains the pixels belonging to class k and $\mathbf{z}_k$ is built from the corresponding labels. Unfortunately, the conditional distribution (2.16) is not easy to sample directly. Thus, we propose to consider a random walk Metropolis Hastings (RWMH) move, which samples the parameters according to an appropriate proposal (specifies in [Has70]) and accept or reject these samples with an appropriate acceptance probability. More implementation details about this move and the resulting algorithm are given in Appendix B.2. It is also interesting to note that a proximal HMC (PHMC) algorithm for non-differential target distribution has also been studied in Appendix E.

Sampling the scale parameter vector $\boldsymbol{\gamma}$

The conditional distribution of the scale parameter vector $\boldsymbol{\gamma}$ satisfies the following relation

$$\begin{aligned} p(\boldsymbol{\gamma}|\mathbf{y},\mathbf{x},\sigma_n^2,\boldsymbol{\xi},\mathbf{z}) &\propto p(\mathbf{y}|\mathbf{x},\sigma_n^2,\boldsymbol{\xi},\boldsymbol{\gamma},\mathbf{z})p(\mathbf{x}|\boldsymbol{\xi},\boldsymbol{\gamma},\mathbf{z})p(\boldsymbol{\gamma}) \\ &\propto p(\mathbf{x}|\boldsymbol{\xi},\boldsymbol{\gamma},\mathbf{z})p(\boldsymbol{\gamma}). \end{aligned} \tag{2.17}$$

Assuming that the scale parameters are independent, we have

$$\begin{aligned} p(\gamma_k|\mathbf{x},\boldsymbol{\xi},\mathbf{z},\boldsymbol{\gamma}_{-k}) &\propto p(\mathbf{x}_k|\xi_k,\gamma_k,\mathbf{z}_k)p(\gamma_k) \\ &\propto \mathcal{IG}\left(\frac{N_k}{\xi_k}, \|\mathbf{x}_k\|_{\xi_k}^{\xi_k}\right) \end{aligned} \tag{2.18}$$

where $\boldsymbol{\gamma}_{-k} = (\gamma_1, ..., \gamma_{k-1}, \gamma_{k+1}, ..., \gamma_K)$ for $k \in \{1, ..., K\}$. Drawing samples from the inverse gamma distribution (2.18) is straightforward. More details about the derivation of (2.18) are provided in Appendix B.1.

Sampling the labels z

The conditional distribution of the labels $\mathbf{z}$ can be computed using Bayes rule

$$\begin{aligned} p(\mathbf{z}|\mathbf{y},\mathbf{x},\sigma_n^2,\boldsymbol{\xi},\boldsymbol{\gamma}) &\propto p(\mathbf{y}|\mathbf{x},\sigma_n^2,\boldsymbol{\xi},\boldsymbol{\gamma},\mathbf{z})p(\mathbf{x}|\boldsymbol{\xi},\boldsymbol{\gamma},\mathbf{z})p(\mathbf{z}) \\ &\propto p(\mathbf{x}|\boldsymbol{\xi},\boldsymbol{\gamma},\mathbf{z})p(\mathbf{z}). \end{aligned} \tag{2.19}$$

Considering the dependency between a label and its neighbors, the conditional distribution of the label z_n (corresponding to the image pixel x_n) is given as follows

$$p(z_n = k|\mathbf{z}_{-n},\mathbf{x},\boldsymbol{\xi},\boldsymbol{\gamma}) \propto p(x_n|z_n = k,\boldsymbol{\xi},\boldsymbol{\gamma})p(z_n = k|\mathbf{z}_{\mathcal{V}(n)}) \tag{2.20}$$

where $\mathbf{z}_{-n}$ is the vector $\mathbf{z}$ whose nth element has been removed and $\mathbf{z}_{\mathcal{V}(n)}$ represents the neighbors of label z_n. Note that a 4-pixel neighborhood structure has been adopted in this chapter. Denoting the left hand side of (2.20) as $\pi_{n,k}$, we have

$$\pi_{n,k} \propto a_k \exp\left(-\frac{|x_n|^{\xi_k}}{\gamma_k}\right) \exp\left(\sum_{n' \in \mathcal{V}(n)} \beta\delta(k - z_{n'})\right). \tag{2.21}$$

The normalized conditional probability of the label z_n is defined as

$$\tilde{\pi}_{n,k} = \frac{\pi_{n,k}}{\sum_{k=1}^{K} \pi_{n,k}}. \tag{2.22}$$

Finally, the label z_n can be drawn from the set $\{1, ..., K\}$ with the respective probabilities $\{\tilde{\pi}_{n,1}, ..., \tilde{\pi}_{n,K}\}$.

Sampling the TRF x

The conditional distribution of the target image we want to estimate is defined as follows

$$p(\mathbf{x}|\mathbf{y}, \sigma_n^2, \boldsymbol{\xi}, \boldsymbol{\gamma}, \mathbf{z}) \propto \exp\left(-\frac{\|\mathbf{y} - \mathbf{H}\mathbf{x}\|_2^2}{2\sigma_n^2} - \sum_{k=1}^{K} \frac{\|\mathbf{x}_k\|_{\xi_k}^{\xi_k}}{\gamma_k} \right). \tag{2.23}$$

Sampling according to (2.23) is the critical point of the proposed algorithm. Due to the high dimensionality of $\mathbf{x}$, classical Gibbs or MH moves are inefficient. Thus we propose to implement an efficient sampling strategy referred to as Hamiltonian Monte Carlo (HMC) method. The principles of this method have been presented in [Nea11] with an application to neural networks. It is widely reported that HMC generally outperforms other standard Metropolis-Hastings algorithms, particularly in high-dimensional scenarios [HG14]. This empirical observation is in agreement with recent theoretical studies showing that HMC has better scaling properties than the Metropolis adjusted Langevin algorithm (MALA) and RWMH [BPR+13]. The main steps of the HMC method with details about the way to adjust its parameters are reported in Appendix B.3.

2.3.2 Parameter estimation

Bayesian estimators of the unknown parameters are computed using the generated samples obtained by the hybrid Gibbs sampler summarized in Algorithm 1. Since the labels are discrete variables, marginal MAP estimators are chosen for the their estimations. The MMSE estimators for the other variables (the TRF $\mathbf{x}$, noise variance σ_n^2 and GGD parameters $\boldsymbol{\xi}$, $\boldsymbol{\gamma}$) are calculated. For example, the MMSE estimator of the TRF $\mathbf{x}$ is computed by

$$\hat{\mathbf{x}}_{\text{MMSE}}|\hat{\mathbf{z}}_{\text{MAP}} \triangleq E\{\mathbf{x}|\mathbf{z} = \hat{\mathbf{z}}_{\text{MAP}}\} = \int p(\mathbf{x}|\mathbf{z} = \hat{\mathbf{z}}_{\text{MAP}}) d\mathbf{x}. \tag{2.24}$$

For each pixel, we can approximate this estimator as follows

$$\hat{x}_{n,\text{MMSE}}|\hat{z}_{n,\text{MAP}} \simeq \frac{1}{M}\sum_{i=1}^{M} x_n^{(i)}|z_n^{(i)} = \hat{z}_{n,\text{MAP}} \tag{2.25}$$

where M is the number of iterations after the so-called burn-in period (see Section 2.4.2 devoted to the sampler convergence for more details) that satisfy $z_n^{(i)} = \hat{z}_{n,\text{MAP}}$, the superscript i represents the ith generated sample and the subscript n is used for the nth pixel. Note that $\hat{\mathbf{z}}_{\text{MAP}}$ is the marginal MAP estimator of the label map and that $\hat{\mathbf{x}}_{\text{MMSE}}$ is the MMSE estimator of the reflectivity. Note also that a similar estimator was implemented in [KTHD12] for image blind deconvolution.

2.3.3 Computational complexity analysis

The computational cost of the proposed Gibbs sampler is mainly due to the generation of the TRF $\mathbf{x}$ and the label map $\mathbf{z}$. In each sampling iteration, the computational complexity for sampling the TRF $\mathbf{x}$ using the HMC is of the order $\mathcal{O}((L+1)N\log N)$, where L is the number of Leapfrog iterations and N is the number of image pixels. The computational complexity for sampling the label map $\mathbf{z}$ is of the order $\mathcal{O}(KN)$, where K is the number of label classes. Thus, in total, the computation complexity for drawing a cycle of samples in the Gibbs sampler is of the order $\mathcal{O}((K+(L+1)\log N)N)$. Note that in general $(L+1)\log N \gg K$. Thus, the most time consuming step is for sampling the TRF.

2.4 Experimental results

This section presents several experiments conducted on simulated and real data using our algorithm. We have also compared our approach with several existing deconvolution algorithms previously applied in US imaging.[2]

2.4.1 Evaluation metrics

Different evaluation metrics were considered for simulated and *in vivo* US images since the TRF ground truth is only available for simulated images. These metrics are presented below.

[2] All the experiments have been conducted using MATLAB R2013a on a computer with Intel(R) Core(TM) i7-4770 CPU @3.40GHz and 8 GB RAM.

Simulated US images

- **Image deconvolution**: The performance of the TRF estimation is assessed in terms of improvement in SNR (ISNR), root mean square error (RMSE), normalized root mean square error (NRMSE), peak signal-to-noise ratio (PSNR) and image structural similarity (MSSIM). These metrics are defined as follows

$$\text{ISNR} = 10\log_{10}\frac{\|\mathbf{x}-\mathbf{y}\|^2}{\|\mathbf{x}-\hat{\mathbf{x}}\|^2}, \tag{2.26}$$

$$\text{RMSE} = \sqrt{\|\mathbf{x}-\hat{\mathbf{x}}\|^2} \tag{2.27}$$

$$\text{NRMSE} = \sqrt{\frac{\|\mathbf{x}-\hat{\mathbf{x}}\|^2}{\|\mathbf{x}\|^2}}, \tag{2.28}$$

$$\text{PSNR} = 20\log_{10}\frac{\max(\mathbf{x},\hat{\mathbf{x}})}{\text{RMSE}}, \tag{2.29}$$

$$\text{MSSIM}(\mathbf{x},\hat{\mathbf{x}}) = \frac{1}{W}\sum_{j=1}^{W}\text{SSIM}(\mathbf{x}_j,\hat{\mathbf{x}}_j) \tag{2.30}$$

  where the vectors $\mathbf{x}, \mathbf{y}, \hat{\mathbf{x}}$ are the ground truth of the TRF, the RF image and the restored TRF, respectively. Note that W is the number of local windows used to analyze the image under study, $\mathbf{x}_j$ and $\hat{\mathbf{x}}_j$ represent the local reflectivities of $\mathbf{x}$ and $\hat{\mathbf{x}}$ located in one of these windows and SSIM is the structural similarity measure of each window (defined in [WBSS04]).

- **Image segmentation**: The performance of the label estimator is assessed using the overall accuracy (OA), defined as the ratio between the number of correctly estimated labels over the total number of labels.

***In vivo* US images** Since the ground truth of the TRF and the label map are not available for *in vivo* US data, the quality of the deconvolution results is evaluated using two other metrics commonly used in US imaging: the resolution gain (RG) [YZX12a] and the contrast-to-noise ratio (CNR) [AM10, JNN+12]. The resolution gain (RG) is the ratio of the normalized autocorrelation (higher than -3 dB) of the original RF US image to the normalized autocorrelation (higher than -3

dB) of the deconvolved image/restored TRF. The definition of the CNR is given by

$$\mathrm{CNR} = \frac{|\mu_1 - \mu_2|}{\sqrt{\sigma_1^2 + \sigma_2^2}} \tag{2.31}$$

where μ_1, μ_2, σ_1 and σ_2 are the means and standard deviations of pixels located in two regions extracted from the image. The two regions are manually chosen so that they belong to different tissue structures. Moreover, as in most US studies, they are at the same depth in order to avoid issues related to wave attenuation. Note that the higher the values of RG and CNR, the better the deconvolution performance.

2.4.2 Sampler convergence

The convergence of the proposed Gibbs sampler can be monitored by determining the so-called burn-in period which refers to the first elements of the Markov chain that are discarded and not used to compute the estimators. The potential scale reduction factor (PSRF) is classically used to determine this burn-in period [GR92]. It requires to run several chains in parallel with different initializations. It is defined by

$$\mathrm{PSRF}_v = \frac{M-1}{M} + \frac{C+1}{CM}\frac{B_v}{W_v} \tag{2.32}$$

where C is the number of Markov chains considered, M is the number of iterations after the burn-in period, B_v and W_v are the intra-chain and inter-chain variances of the variable v, whose definitions are given by

$$B_v = \frac{M}{C-1}\sum_{c=1}^{C}(\bar{v} - \bar{v}_c)^2\,, \tag{2.33}$$

$$W_v = \frac{1}{C}\sum_{c=1}^{C}\frac{1}{M-1}\sum_{i=1}^{M}\left(\bar{v}_c - v_c^{(i)}\right)^2 \tag{2.34}$$

where $\bar{v} = \frac{1}{C}\sum_{c=1}^{C}\bar{v}_c$, $\bar{v}_c = \frac{1}{M}\sum_{i=1}^{M}v_c^{(i)}$ and $v_c^{(i)}$ is the ith sample of the variable v in the cth chain. Values of the PSRF below 1.2 indicate a good convergence of the sampler as suggested in [GR92]. In this work, we checked that the PSRFs of all the variables of interest were below 1.2.

2.4.3 Computational complexity

The computational complexity analysis has been included in Section 2.3.3. In this part, the running time curves versus the image size and number of regions are displayed in Fig. 2.2, which are in agreement with the previous computational complexity analysis. As illustrated in Fig. 2.2, the CPU time is more dependent on the image size than on the structure complexity.

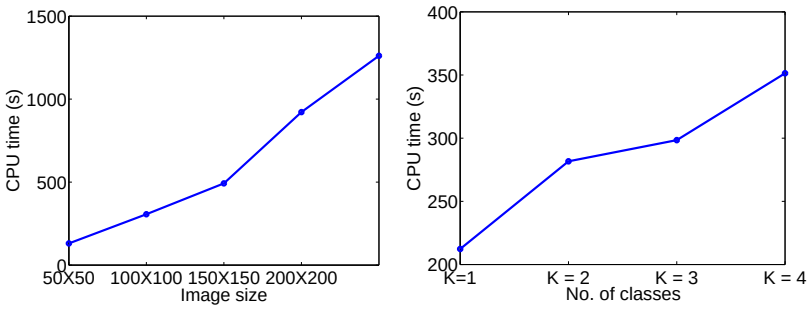

Figure 2.2: CPU time of our algorithm versus the image size (left) and the number of classes (right) for 6000 Monte Carlo iterations. Left: number of classes K = 2. Right: image size 100×100.

2.4.4 Synthetic data

Deconvolution

We first study the deconvolution performance on synthetic data with controlled ground truth, which allows the quality of the different estimators to be appreciated. Precisely, three groups of 2D synthetic images with the same image size $N = 50 \times 50$ are generated assuming that the image pixels are independent and identically distributed (*i.i.d.*) according to GGDs with different shape and scale parameters, as reported in Table 2.1. Each image has been corrupted by a 5×5 Gaussian blurring kernel with variance $\sigma_b = 3$ and an AWGN. The level of AWGN is characterized by the blurred signal-to-noise ratio (BSNR) expressed in decibels as follows

$$\text{BSNR} = 10 \log_{10} \left(\frac{\|\mathbf{Hx} - E(\mathbf{Hx})\|_2^2}{N\sigma_n^2} \right) \tag{2.35}$$

where $E(\cdot)$ is the empirical average operator (sample mean) and N is the total number of image pixels. The BSNR was set to 40 dB for the synthetic data. Regarding the MCMC algorithm, 50

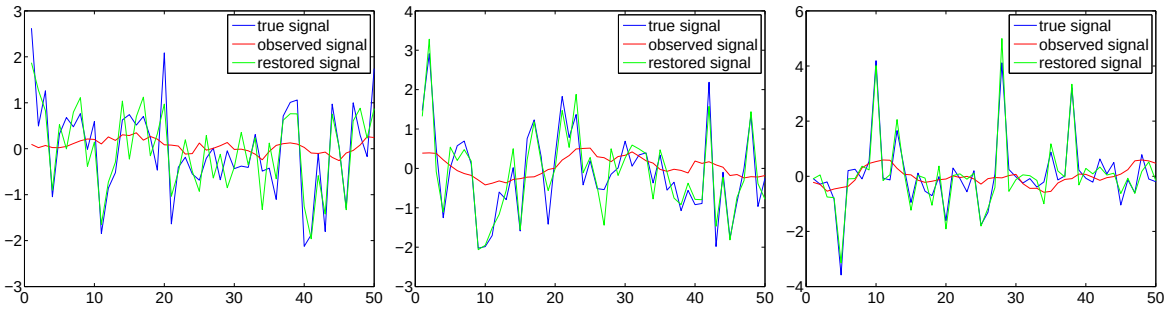

Figure 2.3: Deconvolution results for one column of the synthetic image (the red curves are the observed lines, the blue curves are the ground truth and the green curves are the restored signals using the proposed method). The GGD parameters are $\xi = 2$,$\gamma = 2$ in (a), $\xi = 1.5$,$\gamma = 1.2$ in (b) and $\xi = 0.6$,$\gamma = 0.4$ in (c).

chains of 6000 iterations including a burn-in period of 2000 iterations were run for each simulation scenario. In each Monte Carlo chain, the stepsize was initialized to $\epsilon = 10^{-5}$ and the number of leapfrog steps was uniformly sampled in the interval $[50, 70]$.

The typical deconvolution performance for one column of each of the three observed images is depicted in Fig. 2.3. These results show a good performance of the proposed image deconvolution algorithm. Fig. 2.4 shows the histograms of the generated samples from one single Markov chain for the noise variance, the GGD parameters and the hyperparameters of three synthetic images. These histograms are clearly in good agreement with the true values of the parameters indicated by the vertical lines. More quantitative results of the parameter estimation are reported in Table 2.1.

Segmentation

This section evaluates the performance of our method for the segmentation of two regions of the same size (128×64) using the overall accuracy (OA). Given that pixels in both regions are characterized by two zero-mean GGDs, the difference between the two regions is controlled by the ratios of the shape or scale parameters in the two regions. The values of OAs obtained for different ratios of GGD parameters are displayed in Fig. 2.5. Comparing the two graphs in Fig. 2.5, the variations of OA

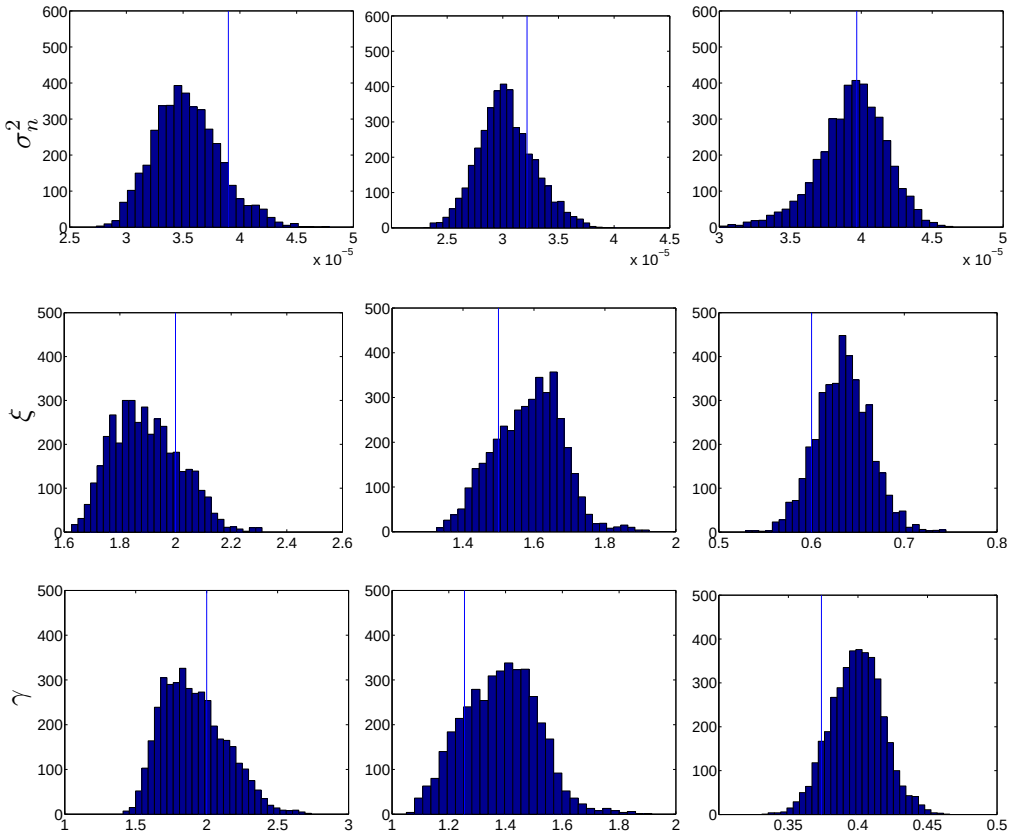

Figure 2.4: Estimated marginal posterior distributions (histograms) of the noise variance σ_n^2 (1st line), the hyperparameters ξ (2nd line) and γ (3rd line). The vertical lines represent the ground truths of the corresponding parameters. Each column corresponds to a given image.

Table 2.1: Parameter Estimations for the synthetic data

Group	Group 1			Group 2			Group 3		
Parameters	σ_n^2 $(\times 10^{-5})$	ξ	γ	σ_n^2 $(\times 10^{-5})$	ξ	γ	σ_n^2 $(\times 10^{-5})$	ξ	γ
True values	3.72	2	2	3.22	1.50	1.26	3.13	0.60	0.37
MMSE	3.65	1.98	2.00	3.63	1.41	1.16	4.15	0.59	0.37
Standard deviation	0.35	0.04	0.05	0.61	0.09	0.09	0.60	0.03	0.02

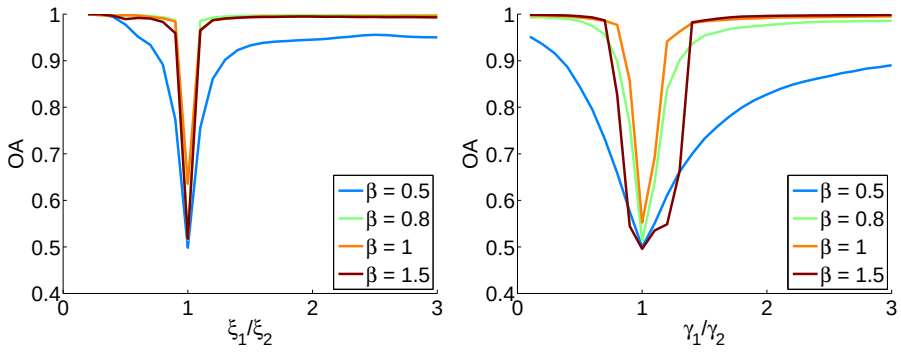

Figure 2.5: OA versus the ratios of the GGD parameters (left: scale parameters $\gamma_1 = \gamma_2 = 20$, right: shape parameters $\xi_1 = \xi_2 = 1$).

are clearly sharper for the left figure, showing that the segmentation accuracy is more sensitive to the shape parameters.

2.4.5 Joint Deconvolution and Segmentation

Comparison with existing methods

Simulated US images The proposed joint deconvolution and segmentation algorithm (denoted as "Joint$_{\text{MCMC}}$") was compared to the technique proposed in [APMS11] (that performs US deconvolution with GGD priors using the EM algorithm, denoted here by "Deconv$_{\text{EM}}$") on simulated data. Since "Deconv$_{\text{EM}}$" was proposed for statistical homogeneous regions, we assumed that the labels associated with the statistically homogeneous regions were known for "Deconv$_{\text{EM}}$". In order to test the robustness of our method to label estimation errors, we also implemented the proposed algorithm using the true labels (denoted as "Deconv$_{\text{MCMC}}$"). In this case, similar to "Deconv$_{\text{EM}}$", only the deconvolution process was performed, without label estimation. Finally, we compared our results with the ℓ_2 and ℓ_1 norm constrained optimization solutions. For the ℓ_2-norm optimization problem, a numerical solution is given by

$$\hat{\mathbf{x}} = (\mathbf{H}^T\mathbf{H} + \lambda\mathbf{I})^{-1}\mathbf{H}^T\mathbf{y} \tag{2.36}$$

where λ is the regularization parameter. Concerning the ℓ_1 norm optimization problem, numerous dedicated algorithms, e.g., ISTA [BT09], FISTA [BT09], TwIST [BDF07] or GEM [BD06] are

available in the literature. The conjugate gradient (CG) method was considered in this work. Note that the regularization parameters were fixed manually by cross validation for the ℓ_2 and ℓ_1 norm constraint optimization problems.

***In vivo* US images** Due to the fact that the ground truth for the label map is not available for *in vivo* US data, we were not able to test the methods "Deconv$_{\text{EM}}$" and "Deconv$_{\text{MCMC}}$" for these images. Instead, we considered Gaussian and Laplacian priors that have been extensively used in the US image deconvolution literature [MT07], [JT08], [YZX12a]. The analytical solution for the ℓ_2-norm optimization problem is given by (2.36). The GPSR (gradient projection for sparse reconstruction) [FNW07] algorithm is implemented for the ℓ_1 norm constrained optimization problem for the real data, where the regularization parameter is chosen as $0.1\|\mathbf{H}^T\mathbf{y}\|_\infty$, as suggested in [FNW07].

Joint deconvolution and segmentation for simulated US images

Experiments were first conducted on three groups of simulated US images with a simulation scenario inspired by [NPK+07]. The PSF was simulated with a realistic state-of-the-art ultrasound simulator Field II [Jen96] corresponding to a 3.5 MHz linear probe as shown in Fig. 2.6 (a). All images were simulated with the same PSF and contaminated by an AWGN with BSNR= 30 dB. All the simulation results presented hereinafter were obtained using 6000 Monte Carlo iterations, including a burn-in period of 2000 iterations.

- Group 1: The TRF $\mathbf{x}$ mimicking a hyperechoic (bright) round inclusion into an homogeneous medium was blurred by the simulated PSF and contaminated by an AWGN with BSNR = 30 dB. The simulated images are of size 128×128. The pixels located inside and outside the inclusion, indicated by the label map in Fig. 2.6(c), are distributed according to GGDs with parameters $(\xi, \gamma) = (0.6,1)$ (inside) and $(\xi, \gamma) = (1.8,2)$ (outside) as highlighted in Fig. 2.6(b). The simulated observed B-mode image (log-compressed envelop image of the corresponding beamformed RF data which is commonly used for visualization purpose in US imaging) is shown in Fig. 2.6(d). The quality of the deconvolution can be appreciated by comparing the estimated TRFs shown in Figs. 2.6(e)-2.6(i) obtained with the methods ℓ_2, ℓ_1, Deconv$_{\text{EM}}$,

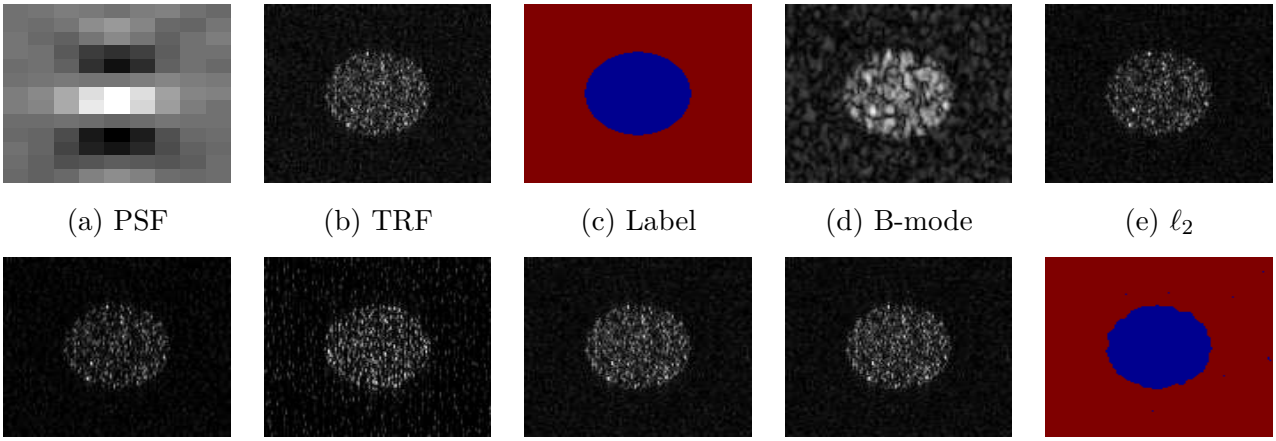

(a) PSF (b) TRF (c) Label (d) B-mode (e) ℓ_2

(f) ℓ_1 (g) $\text{Deconv}_{\text{EM}}$ (h) $\text{Deconv}_{\text{MCMC}}$ (i) $\text{Joint}_{\text{MCMC}}$ (j) $\text{Joint}_{\text{MCMC}}$

Figure 2.6: Group 1: (a) Simulated PSF; (b) Ground truth of the TRF; (c) Ground truth for label map; (d) Observed B-mode image; (e)-(i) Estimated TRFs in B-mode form obtained with methods ℓ_2, ℓ_1, $\text{Deconv}_{\text{EM}}$, $\text{Deconv}_{\text{MCMC}}$ and the proposed $\text{Joint}_{\text{MCMC}}$; (j) Estimated label map obtained with the proposed method (regularization parameters for the ℓ_2 and ℓ_1 methods set to 0.01 and 0.1).

$\text{Deconv}_{\text{MCMC}}$ and the proposed $\text{Joint}_{\text{MCMC}}$. The quality of the segmentation can be observed in Fig. 2.6(j), which shows the estimated label map obtained with the method $\text{Joint}_{\text{MCMC}}$. Finally, the performance of the GGD parameter estimators is illustrated by the histograms of the generated GGD parameters $(\boldsymbol{\xi}, \boldsymbol{\gamma})$ displayed in Fig. 2.7, where the red and green vertical lines indicate the MMSE estimates and the true values of the parameters, respectively.

- Group 2: The TRF $\mathbf{x}$ is an homogeneous medium with two hypoechoic (dark) round inclusions (see Fig. 2.8(a)) that was blurred by the same simulated PSF and contaminated by an AWGN. The size of the US reflectivity image is 100×100 and BSNR = 30 dB. The pixels located inside and outside the inclusions are distributed according to GGDs with parameter vectors $(\xi, \gamma) =$ (0.8,10) (inside) and $(\xi, \gamma) =$ (1.5,1) (outside) as highlighted in Fig. 2.8(a). The simulated observed B-mode image is shown in Fig. 2.8(c) whereas the ground truth of the label map is given in Fig. 2.8(b). Figs. 2.8(d)-2.8(h) show the estimated TRFs obtained with the methods ℓ_2, ℓ_1, $\text{Deconv}_{\text{EM}}$, $\text{Deconv}_{\text{MCMC}}$ and the proposed $\text{Joint}_{\text{MCMC}}$, confirming the good performance

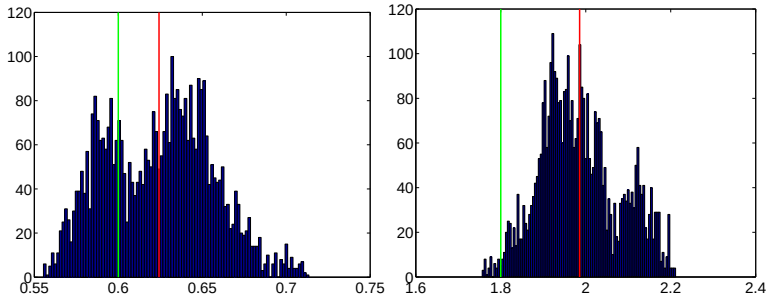

(a) $\boldsymbol{\xi}_{in}$ (b) $\boldsymbol{\xi}_{out}$

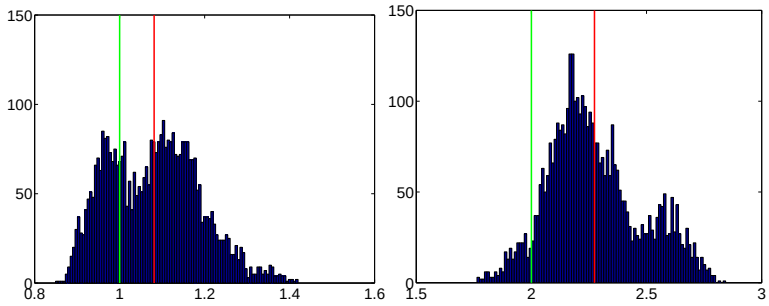

(c) $\boldsymbol{\gamma}_{in}$ (d) $\boldsymbol{\gamma}_{out}$

Figure 2.7: (Group 1) 1st line includes the histograms of shape parameters $\boldsymbol{\xi}$ for the pixels inside (left) and outside (right) the inclusion; 2nd line includes the histograms of scale parameters $\boldsymbol{\gamma}$ for the pixels inside (left) and outside (right) the inclusion; The red and green vertical lines are the MMSE estimates and the true values of the parameters $\boldsymbol{\xi}$, $\boldsymbol{\gamma}$, respectively.

Table 2.2: Hyperparameter Estimations for Simulated data (Group 2).

Method	ξ_1	ξ_2	γ_1	γ_2
Ground truth	0.8	1.5	10	1
$\text{Deconv}_{\text{EM}}$	0.60	0.96	21.10	0.42
$\text{Deconv}_{\text{MCMC}}$	0.80	2.15	10.05	1.50
$\text{Joint}_{\text{MCMC}}$	0.82	1.37	11.24	0.82

of $\text{Joint}_{\text{MCMC}}$ for the deconvolution of US images. The estimated label map obtained with the method $\text{Joint}_{\text{MCMC}}$ is shown in Fig. 2.8(i), confirming its good segmentation performance. Finally, the hyperparameter estimates of Group 2 are shown in Table 2.2, confirming the good estimation performance.

- Group 3: The third simulated image was obtained by using a clean TRF $\mathbf{x}$ of size 275×75 (see Fig. 2.9(a)) blurred by the same simulated PSF and contaminated by an AWGN such that BSNR = 30 dB. A more realistic geometry of the simulated tissues was considered, inspired by one of the *in vivo* results provided in the next section (see Fig. 2.11(i)). Three different structures were generated mimicking the skin, the tumor and the surrounding tissue (green, red and blue regions in Fig. 2.9(b)). The pixels in the different regions are distributed according to GGDs with different parameters: $(\xi, \gamma) = (0.5, 1)$ for the blue region, $(\xi, \gamma) = (1, 30)$ for the green region and $(\xi, \gamma) = (1.8, 2)$ for the red region. Figs. 2.9(d)-2.9(h) show the estimated TRFs obtained with the methods ℓ_2, ℓ_1, $\text{Deconv}_{\text{EM}}$, $\text{Deconv}_{\text{MCMC}}$ and $\text{Joint}_{\text{MCMC}}$. The estimated label map obtained with the method $\text{Joint}_{\text{MCMC}}$ is also shown in Fig. 2.9(i). Visually, we remark that all the three methods provide images with better object boundary definition (better spatial resolution) than the observed B-mode images. The quantitative results reported in Table 2.3 confirm that given the same conditions (knowledge of the true label map), our approach "$\text{Deconv}_{\text{MCMC}}$" is more accurate than the existing "$\text{Deconv}_{\text{EM}}$". Moreover, we can note that the proposed technique "$\text{Joint}_{\text{MCMC}}$" is able to estimate the label map with a precision of more than 98% and with a small quality loss for the estimated TRF.

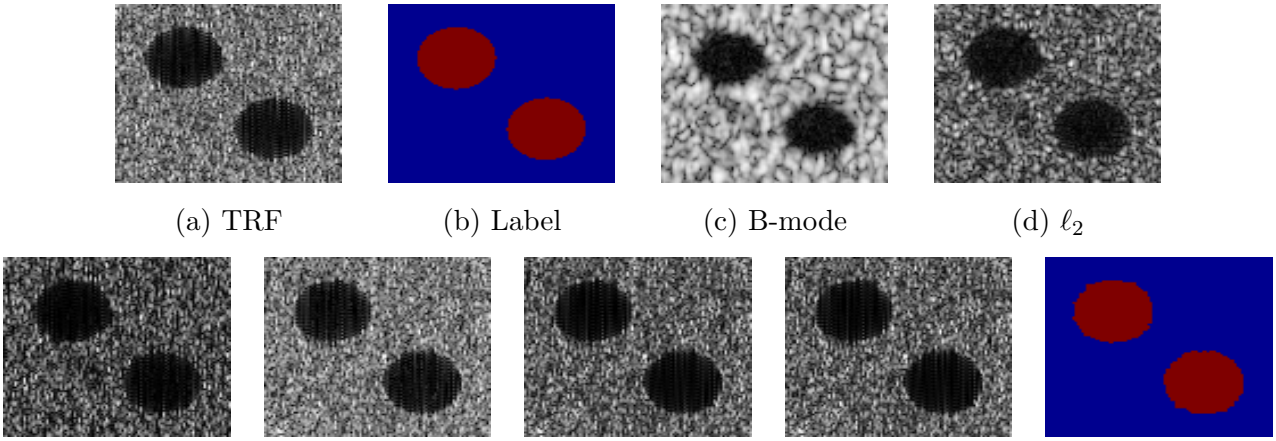

(a) TRF (b) Label (c) B-mode (d) ℓ_2

(e) ℓ_1 (f) $\text{Deconv}_{\text{EM}}$ (g) $\text{Deconv}_{\text{MCMC}}$ (h) $\text{Joint}_{\text{MCMC}}$ (i) $\text{Joint}_{\text{MCMC}}$

Figure 2.8: Group 2: (a) Ground truth of the TRF; (b) Ground truth for label map; (c) Observed B-mode image; (d)-(h) Estimated TRFs in B-mode form obtained with the methods ℓ_2, ℓ_1, $\text{Deconv}_{\text{EM}}$, $\text{Deconv}_{\text{MCMC}}$ and the proposed $\text{Joint}_{\text{MCMC}}$; (i) Estimated label map obtained with the proposed method (regularization parameters for the ℓ_2 and ℓ_1 methods set to 0.1 and 1).

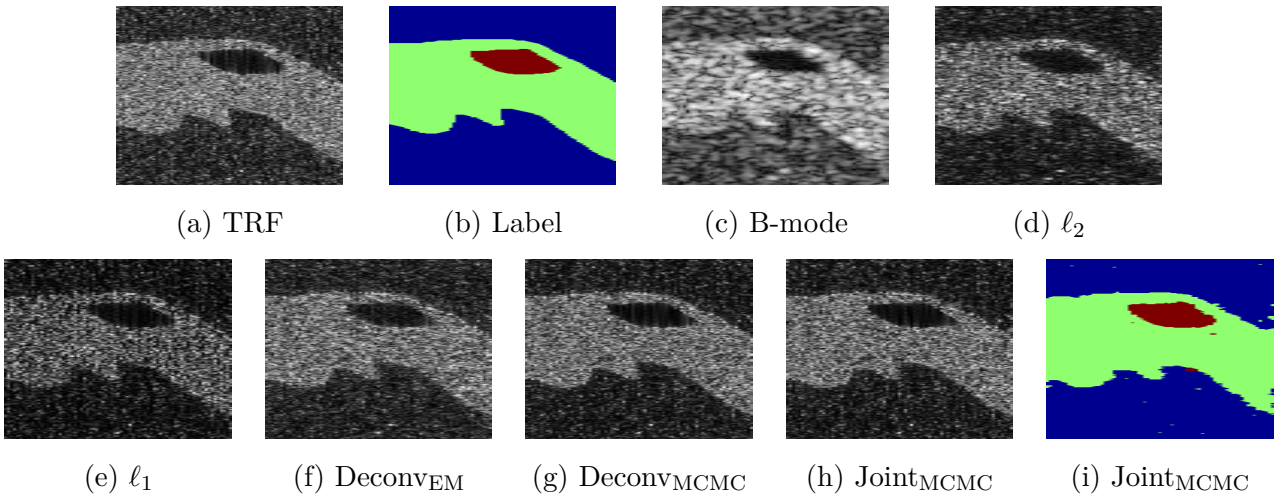

(a) TRF (b) Label (c) B-mode (d) ℓ_2

(e) ℓ_1 (f) $\text{Deconv}_{\text{EM}}$ (g) $\text{Deconv}_{\text{MCMC}}$ (h) $\text{Joint}_{\text{MCMC}}$ (i) $\text{Joint}_{\text{MCMC}}$

Figure 2.9: Group 3: (a) Ground truth of the TRF; (b) Ground truth for label map; (c) Observed B-mode image; (d)-(h) Estimated TRFs in B-mode form obtained with methods ℓ_2, ℓ_1, $\text{Deconv}_{\text{EM}}$, $\text{Deconv}_{\text{MCMC}}$ and the proposed $\text{Joint}_{\text{MCMC}}$; (i) Estimated label map obtained with the proposed method (regularization parameters for the ℓ_2 and ℓ_1 methods set to 0.1 and 1).

Table 2.3: Deconvolution Quality Assessment for Simulated data

Group	Method	ISNR (dB)	NRMSE	PSNR (dB)	MSSIM	OA
1	ℓ_2	12.83	0.52	33.19	0.98	N/A
	ℓ_1	12.83	0.52	33.19	0.98	N/A
	$\text{Deconv}_{\text{EM}}$	13.04	0.46	33.74	0.98	N/A
	$\text{Deconv}_{\text{MCMC}}$	16.21	0.35	36.57	0.99	N/A
	$\text{Joint}_{\text{MCMC}}$	16.01	0.36	36.37	0.99	0.99
2	ℓ_2	10.63	0.69	21.02	0.61	N/A
	ℓ_1	12.75	0.54	23.30	0.79	N/A
	$\text{Deconv}_{\text{EM}}$	14.31	0.45	24.70	0.82	N/A
	$\text{Deconv}_{\text{MCMC}}$	15.09	0.41	25.39	0.88	N/A
	$\text{Joint}_{\text{MCMC}}$	15.00	0.42	25.26	0.88	0.99
3	ℓ_2	9.96	0.70	21.92	0.64	N/A
	ℓ_1	11.49	0.59	23.45	0.76	N/A
	$\text{Deconv}_{\text{EM}}$	12.21	0.54	24.16	0.78	N/A
	$\text{Deconv}_{\text{MCMC}}$	12.40	0.52	24.40	0.80	N/A
	$\text{Joint}_{\text{MCMC}}$	12.38	0.53	24.37	0.79	0.98

Visually, we remark that all the three methods provide images with better object boundary definition (better spatial resolution) than the observed B-mode images. The quantitative results reported in Table 2.3 confirm that given the same conditions (knowledge of the true label map), our approach "$\text{Deconv}_{\text{MCMC}}$" is more accurate than the existing "$\text{Deconv}_{\text{EM}}$". Moreover, we can note that the proposed technique "$\text{Joint}_{\text{MCMC}}$" is able to estimate the label map with a precision of more than 98% and with a small quality loss for the estimated TRF.

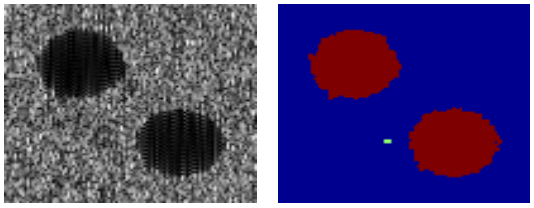

Figure 2.10: Estimated TRF (left) and label map (right) for a two-class image with $K = 3$ (ISNR = 14.46 and OA = 0.8).

Influence of the number of classes While most of the hyperparameters are automatically estimated in our Bayesian method, the number of classes K has to be tuned manually. This section studies the influence of the parameter K on the segmentation and deconvolution. For this purpose, we have reconsidered the simulated image of Group 2 by setting $K = 3$, while the TRF only contains two classes of pixels. The corresponding estimated TRFs and label maps are shown in Fig. 2.10. A visual inspection as well as the obtained ISNR show that the restored TRF in Fig. 2.10 (left) is similar to the result in Fig. 2.8 that was obtained by setting $K = 2$ using the proposed method. A slight degradation of the estimated label field can be observed, as highlighted by the OA that decreases from 0.99 to 0.8.

Joint deconvolution and segmentation for *in vivo* US images

Three groups of experiments have been conducted to evaluate the performance of the proposed method for *in vivo* US images. The images were acquired with a 20 MHz single-element US probe. In contrast to the simulation scenarios studied previously, the PSF and the TRF are not available for *in vivo* experiments. For this reason, the PSF has been estimated from the RF image using the method of [MA05]. The regions selected for the computation of CNR are shown in the red rectangles of the observed B-mode images in Figs. 2.11(a),(e),(i). All the estimated TRFs are shown in B-mode form, after envelope detection and log-compression. The envelope detection is generally performed by considering the magnitude of the analytic signal in US imaging. While it is adapted to bandlimited modulated RF signals, this envelope detector may generate artifacts on TRFs. To avoid this phenomenon, we have used a different envelope detection method for the restored TRF, *i.e.*, the

method of [PFG04] based on the detection and interpolation of local maxima.

- Group 1 - Mouse bladder: The observed B-mode image of size 400×256 is shown in Fig. 2.11(a) and displays a mouse bladder. The US transducer was placed into a small water container to ensure an efficient transmission of the US waves into the tissues. As there is no US scatterer in the water, the region located in the upper part of the image in Fig. 2.11(a) appears dark (no signal). It is also the case for the region located inside the bladder that also contains a fluid with poor reflection for the US waves. The number of homogeneous regions was set to $K = 3$ in this experiment, which is sufficient to represent the anatomical structures of the image. The number of Monte Carlo iterations was fixed to 10 000 (including 5 000 burn-in iterations). The parameters of the HMC method for the *in vivo* data were adjusted to the same values as in the previous experiments. The regularization parameters for the ℓ_2-norm and ℓ_1-norm constraint optimization problems were set to 10 and 54.39 by cross-validation. Figs. 2.11(b)-2.11(d) display the restored TRFs obtained with the ℓ_2, ℓ_1 optimization algorithms and the proposed method. The proposed method provides good restoration results, especially with clearer boundaries. Fig. 2.13(a) shows the marginal MAP estimates of the labels, which segment the estimated image into several statistically homogeneous regions. The different anatomical structures of the image can be clearly recovered. Note that the two regions corresponding to fluids are identified with the same estimated label.

- Group 2 - Skin melanoma: The second *in vivo* image (of size 400×298) represents a skin melanoma tumor acquired in the same conditions as previously, shown in Fig. 2.11(e). Water-based gel was placed between the US probe and the skin of the patient. It represents the dark regions in the upper part of the image in Fig. 2.11(e). The rest of the tissues corresponds to the skin layers. The number of homogeneous regions was fixed to $K = 4$. The number of Monte Carlo iterations was fixed to 20000 (including 10000 burn-in period) for this example. The regularization parameters for the ℓ_2-norm and ℓ_1-norm constraint optimization problems were set to 1 and 1.2×10^3 by cross-validation. Figs. 2.11(f)-2.11(h) display the restored TRFs with the different methods (ℓ_2, ℓ_1 optimization algorithms and proposed method). Note that

Fig. 2.11(h) shows an improved contrast between the tumor and the healthy skin tissue when compared to the observed B-mode image in Fig. 2.11(e). The tumor boundaries are better defined on the deconvolved image with the proposed method compared to the observed B-mode image. To better visualize the improved transition between the tumor and the healthy skin tissue, we show in Fig. 2.12 two vertical profiles passing through the tumor, corresponding to the blue line in Fig. 2.11(e), extracted from our result and observation. One can remark the sharper slopes obtained on the deconvolved image in the neighbourhood of tumor boundaries, *i.e.*, around positions 200 and 300. The marginal MAP estimates of the labels for this image are shown in Fig. 2.13(b). The four estimated labels correspond to the water-gel (light blue), the tumor (yellow) and the skin tissues (the two shades of red).

- Group 3 - Healthy skin tissue: The last *in vivo* US data represents a healthy skin image shown in Fig. 2.11(i), which is of size 832×299. The number of homogeneous regions was set to $K = 2$. The number of Monte Carlo iterations was fixed to 6000 including a burn-in period of 2000 iterations). The regularization parameters for the ℓ_2-norm and ℓ_1-norm constraint optimization problems were set to 10 and 1.5×10^4 by cross-validation. The restored TRFs obtained with the different methods (ℓ_2, ℓ_1 optimization algorithms and the proposed method) are displayed in Figs. 2.11(j)-2.11(l). The marginal MAP estimation of the label field is shown in Fig. 2.13(c).

In addition to the visual inspection, the deconvolution results were evaluated using the RG and CNR criteria and the CPU time, as reported in Table 2.4. Despite its higher computational complexity, the visual impression and the numerical results confirm that a better contrast and more defined boundaries between the different tissues is achieved with the proposed method. It is interesting to note that in addition to the restored image, our algorithm also provides a segmentation result. To our knowledge, there is no other existing method in US imaging able to achieve this joint segmentation and deconvolution performance.

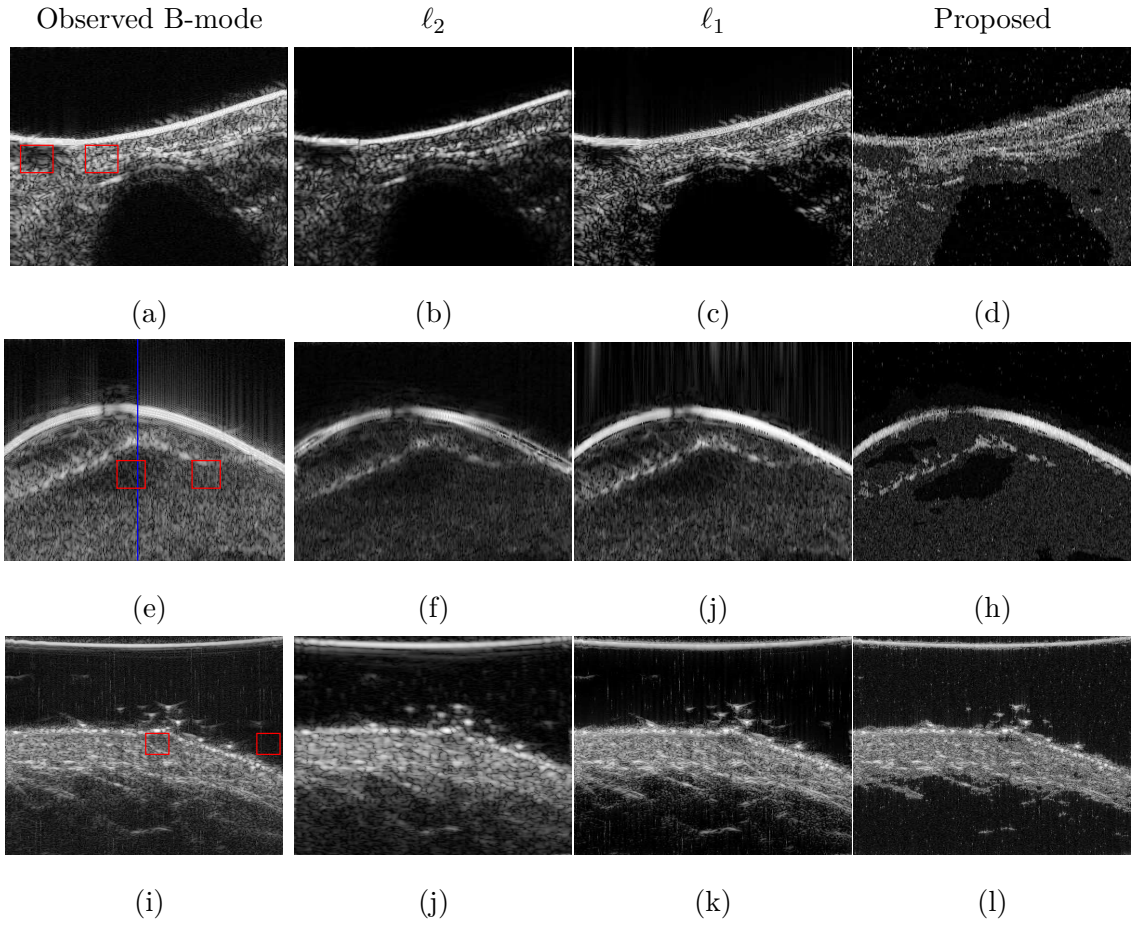

Figure 2.11: From up to down: 1st row corresponds to the mouse bladder; 2nd row is for the skin melanoma; 3rd row is for the healthy skin tissue. From left to right: Observed B-mode image, Restored B-mode images with ℓ_2-norm, ℓ_1-norm and the proposed method. The regions selected for computing CNR are shown in the red boxes in the observed B-mode images.

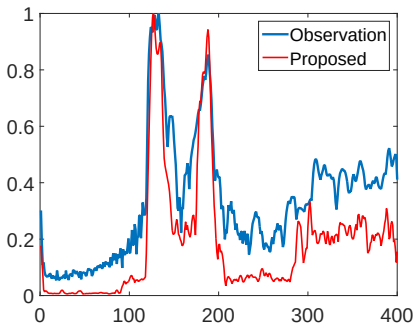

Figure 2.12: Vertical profiles passing through the skin tumor, extracted from the observed and restored images of the skin melanoma (group 2).

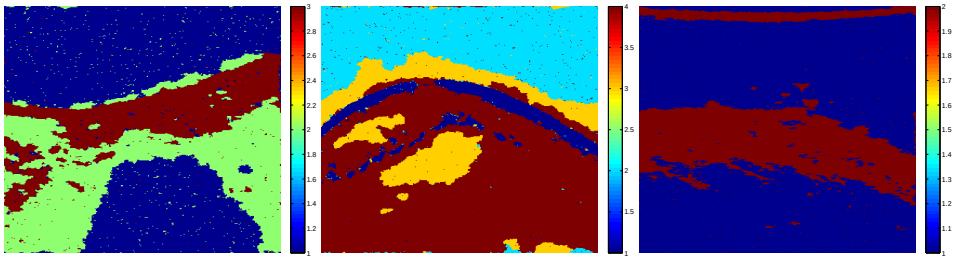

(a) (b) (c)

Figure 2.13: Marginal MAP estimates of labels. (Left) is the label map for the mouse bladder. The estimated labels in blue correspond to liquid regions whereas the other labels represent tissue regions with different statistical properties. (Middle) is the label map for the skin melanoma. The four estimated labels correspond to the water-gel (light blue), the tumor (yellow) and the skin tissues (the two shades of red). (Right) is the label map for the healthy skin tissue. The skin tissue appears in red.

Table 2.4: Deconvolution Quality for the real US data

Group	group 1 - Mouse bladder			group 2 - Skin melanoma			group 3 - Healthy skin tissue		
Metrics	RG	CNR	Time (s)	RG	CNR	Time (s)	RG	CNR	Time (s)
Observation	-	1.08	-	-	1.17	-	-	1.30	-
ℓ_2	3.82	1.00	0.006	3.01	1.09	0.007	1.07	**3.01**	0.007
ℓ_1	3.29	**1.11**	5.07	4.63	1.19	3.53	2.09	2.47	22.30
Proposed	**3.94**	0.94	3904.8	**10.01**	**1.35**	1303.4	**2.59**	2.23	6585.8

2.5 Conclusions

In this chapter, we proposed a new Bayesian method for joint deconvolution and segmentation of medical ultrasound images. This method assumed that the ultrasound image can be divided into regions with statistical homogeneous properties. Based on this assumption, a Potts model was introduced for the image labels. Independent generalized Gaussian priors were also assigned to the tissue reflectivity functions of each homogeneous region of the image. According to the author's knowledge, it is the first time a joint segmentation and deconvolution method is proposed for ultrasound images. The proposed method showed very interesting restoration results when compared to more classical optimization methods based on ℓ_2-norm or ℓ_1-norm regularizations.

Chapter 3

Fast Single Image Super-resolution

Part of this chapter has been adapted from the journal paper [ZWB+16a] and the conference paper [ZWB+16c].

Contents

3.1 Introduction . . . 69
3.2 Image Super-resolution Formulation . . . 71
3.2.1 Model of Image Formation . . . 71
3.2.2 Problem formulation . . . 72
3.3 Proposed fast super-resolution using an ℓ_2-regularization . . . 73
3.3.1 Proposed closed-form solution for the $\ell_2 - \ell_2$ problem . . . 74
3.3.2 Solution of the $\ell_2 - \ell_2$ problem in the image domain . . . 76
3.3.3 Solution of the $\ell_2 - \ell_2$ problem in the gradient domain . . . 77
3.4 Generalized fast super-resolution . . . 79
3.4.1 General form of the proposed algorithm . . . 80
3.4.2 TV regularization . . . 80
3.4.3 ℓ_1-norm regularization in the wavelet domain . . . 82
3.4.4 Learning-based ℓ_2-norm regularization . . . 83
3.5 Experimental Results . . . 83
3.5.1 Fast SR using ℓ_2-regularizations . . . 84
3.5.2 Natural images: Embedding the $\ell_2 - \ell_2$ analytical solution into the ADMM . . . 91
3.5.3 Medical ultrasound images: Embedding the $\ell_2 - \ell_2$ analytical solution into the ADMM framework . . . 99
3.6 Conclusion . . . 101

3.1 Introduction

As stated in the introduction, the image formation model for single image super-resolution can be written as

$$\mathbf{y} = \mathbf{SHx} + \mathbf{n} \tag{3.1}$$

where the vectors $\mathbf{x} \in \mathbb{R}^{N_h}$ and $\mathbf{y} \in \mathbb{R}^{N_l}$ are the high resolution (HR) and low resolution (LR) images, the matrices $\mathbf{H} \in \mathbb{R}^{N_h \times N_h}$ and $\mathbf{S} \in \mathbb{R}^{N_l \times N_h}$ are the blurring and decimation matrices. In this chapter, we propose a general method based on reconstruction techniques which is valid for both natural and medical ultrasound images. Existing reconstruction-based techniques used to solve the single image SR include the first order gradient-based methods [SSXS08, SSXS11, TLBL10, YWHM10], the iterative shrinkage thresholding-based algorithms [BT09] (also called forward-backward algorithms), proximal gradient algorithms and other variable splitting algorithms that rely on the augmented Lagrangian (AL) scheme. The AL-based algorithms include the alternating direction method of multipliers (ADMM) [NWY10, MBD15, MBK12, MO08], the split Bregman (SB) methods [YLTV15] (known to be equivalent to ADMM in certain conditions [YOGD08]) and their variants.

Particularly, Ng *et. al.* [NWY10] proposed an ADMM-based algorithm to solve a TV-regularized single image SR problem, where the decimation and blurring operators are split and solved iteratively. Due to this splitting, the cumbersome SR problem can be decomposed into an up-sampling problem and a deconvolution problem, that can be both solved efficiently. Yanovsky *et. al.* [YLTV15] proposed to solve the same problem with an SB algorithm. However, the decimation operator was handled through a gradient descent method integrated in the SB framework. Sun *et. al.* [SSXS08, SSXS11] proposed a gradient profile prior and formulated the single image SR problem as an ℓ_2-regularized optimization problem, further solved with the gradient descent method. Yang *et. al.* [YWHM10] proposed a learning-based algorithm for the single image SR by seeking a sparse representation using the patches of LR and HR images, followed by back projecting through a gradient descent method. Despite the efficiency of these methods, it is still appealing to deal with the single image SR problem in a non-iterative or more efficient way.

This chapter aims at reducing the computational cost of these methods by proposing a new approach handling the decimation and blurring operators simultaneously by exploring their intrinsic properties in the frequency domain. It is interesting to note that similar properties were explored in [RTLF10, SKM11] for multi-frame SR. However, the implementation of the matrix inversions proposed in [RTLF10, SKM11] is less efficient than those proposed in this work, as it will be demonstrated in the complexity analysis conducted in Section 3.3. More precisely, this chapter derives a

closed-form expression of the solution associated with the ℓ_2-penalized least-squares SR problem, when the observed LR image is assumed to be a noisy, subsampled and blurred version of the HR image with a spatially invariant blur. This model, referred to as $\ell_2 - \ell_2$ in what follows, underlies the restoration of an image contaminated by additive Gaussian noise and has been used intensively for the single image SR problem, see, e.g., [YWHM10, SSXS08, EV08] and the references mentioned above. The proposed solution is shown to be easily embeddable into an AL framework to handle non-Gaussian priors (i.e., non-ℓ_2 regularizations), which significantly lightens the computational burdens of several existing SR algorithms.

3.2 Image Super-resolution Formulation

3.2.1 Model of Image Formation

Consider the image formation model (3.1), two additional basic assumptions about the blurring and decimation operators are introduced. These assumptions have been widely used for image deconvolution or image SR problems (see, e.g., [EF97a, FREM04, ZEP12, YWHM10]) and are necessary for the proposed fast SR framework.

Assumption 1. *The blurring matrix* $\mathbf{H}$ *is the matrix representation of the cyclic convolution operator, i.e.,* $\mathbf{H}$ *is a block circulant matrix with circulant blocks (BCCB).*

This assumption has been widely used in the image processing literature [LS04, RTLF10, SKM11]. It is satisfied provided the underlying blurring kernel is shift-invariant and the boundary conditions make the convolution operator periodic. Note that the BCCB matrix assumption does not depend on the shape of the blurring kernel, i.e., it is satisfied for any kind of blurring, including motion blur, out-of-focus blur, atmospheric turbulence, etc. Using the cyclic convolution assumption, the blurring matrix and its conjugate transpose can be decomposed as

$$\mathbf{H} = \mathbf{F}^H \mathbf{\Lambda} \mathbf{F} \tag{3.2}$$

$$\mathbf{H}^H = \mathbf{F}^H \mathbf{\Lambda}^H \mathbf{F} \tag{3.3}$$

where the matrices $\mathbf{F}$ and $\mathbf{F}^H$ are associated with the Fourier and inverse Fourier transforms (satisfying $\mathbf{F}\mathbf{F}^H = \mathbf{F}^H\mathbf{F} = \mathbf{I}_{N_h}$) and $\mathbf{\Lambda} = \text{diag}\{\mathbf{Fh}\} \in \mathbb{C}^{N_h \times N_h}$ is a diagonal matrix, whose diagonal elements are the Fourier coefficients of the first column of the blurring matrix $\mathbf{H}$, denoted as $\mathbf{h}$. Using the decompositions (4.24) and (4.25), the blurring operator $\mathbf{Hx}$ and its conjugate $\mathbf{H}^H\mathbf{x}$ can be efficiently computed in the frequency domain, see, e.g., [Ng06, EF97b, ZBKT16].

Assumption 2. *The decimation matrix* $\mathbf{S} \in \mathbb{R}^{N_l \times N_h}$ *is a down-sampling operator, while its conjugate transpose* $\mathbf{S}^H \in \mathbb{R}^{N_h \times N_l}$ *interpolates the decimated image with zeros.*

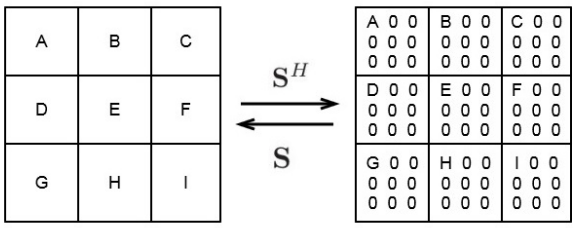

Figure 3.1: Effect of the up-sampling matrix $\mathbf{S}^H$ on a 3×3 image and of the down-sampling matrix $\mathbf{S}$ on the corresponding 9×9 image (whose scale up factor equals 3).

Once again, numerous research works have used this assumption [RTLF10, SKM11, YWHM10, ZEP12]. Fig. 3.1 shows a toy example highlighting the roles of the decimation matrix $\mathbf{S}$ and its conjugate transpose $\mathbf{S}^H$. The decimation matrix satisfies the relationship $\mathbf{S}\mathbf{S}^H = \mathbf{I}_{N_l}$. Denoting $\underline{\mathbf{S}} \triangleq \mathbf{S}^H\mathbf{S}$, multiplying an image by $\underline{\mathbf{S}}$ can be achieved by making an entry-wise multiplication with an $N_h \times N_h$ mask having ones at the sampled positions and zeros elsewhere.

3.2.2 Problem formulation

Similar to traditional image reconstruction problems, the estimation of an HR image from the observation of an LR image is an ill-posed problem. This ill-posedness is classically overcome by incorporating some appropriate prior information or regularization term. The regularization term can be chosen from a specific task of interest, the information resulting from previous experiments or from a perceptual view on the constraints affecting the unknown model parameters [Rob07, GCS+13]. Various priors or regularizations have already been advocated to regularize the image SR problem in the

literature, including: (i) traditional generic image priors such as Tikhonov [NMG01, WDT15b, EV08], total variation (TV) [NWY10, AD05, MO08] and priors prompting sparsity in transformed domains [BD06, NPK+07, JJC04, FN03], (ii) more recent image regularizations such as the gradient profile prior [SSXS08, SSXS11, TLBL10] or Fattal's edge statistics [Fat09] and (iii) learning-based priors [RB05, ZW11]. The fast approach proposed in the next section is shown to be adapted to many of the existing regularization terms.

Assuming that the noise $\mathbf{n}$ in (3.1) is AWGN and incorporating a proper regularization to the target image $\mathbf{x}$, the maximum *a posteriori* (MAP) estimator of $\mathbf{x}$ for the single image SR can be obtained by solving the following optimization problem

$$\min_{\mathbf{x}} \frac{1}{2} \underbrace{\|\mathbf{y} - \mathbf{S}\mathbf{H}\mathbf{x}\|_2^2}_{\text{data fidelity}} + \quad \tau \quad \underbrace{\phi(\mathbf{A}\mathbf{x})}_{\text{regularization}} \tag{3.4}$$

where $\|\mathbf{y} - \mathbf{S}\mathbf{H}\mathbf{x}\|_2^2$ is a *data fidelity term* associated with the model likelihood and $\phi(\mathbf{A}\mathbf{x})$ is related to the image prior information and is referred to as *regularization* or *penalty* [EHN96]. Note that the matrix $\mathbf{A}$ can be the identity matrix when the regularization is imposed on the SR image itself, the gradient operator, any orthogonal matrix or normalized tight frame, depending on the addressed application and the properties of the target image. The role of the regularization parameter τ is to weight the importance of the regularization term with respect to (w.r.t.) the data fidelity term. The next section derives a closed-form solution of the problem (3.4) for a quadratic regularizing operator $\phi(\cdot)$ when the assumptions 1 and 2 hold.

3.3 Proposed fast super-resolution using an ℓ_2-regularization

Before considering more complicated regularizations investigated in Section 3.4, we first consider the basic ℓ_2-norm regularization defined by

$$\phi(\mathbf{A}\mathbf{x}) = \|\mathbf{A}\mathbf{x} - \mathbf{v}\|_2^2 \tag{3.5}$$

where the matrix $\mathbf{A}^H\mathbf{A}$ is assumed, unless otherwise specified, to be invertible. Typical examples of appropriate matrices $\mathbf{A}$ include the Fourier transform matrix, the wavelet transform matrix, etc.

When using this ℓ_2-norm regularization, a generic form of a fast solution to problem (3.4) will be derived in Section 3.3.1. Then, two particular cases of this regularization widely used in the literature will be discussed in Sections 3.3.2 and 3.3.3.

3.3.1 Proposed closed-form solution for the $\ell_2 - \ell_2$ problem

With the regularization (3.5), the problem (3.4) transforms to

$$\min_{\mathbf{x}} \frac{1}{2}\|\mathbf{y} - \mathbf{SHx}\|_2^2 + \tau\|\mathbf{Ax} - \mathbf{v}\|_2^2 \tag{3.6}$$

whose solution is given by

$$\hat{\mathbf{x}} = (\mathbf{H}^H\underline{\mathbf{S}}\mathbf{H} + 2\tau\mathbf{A}^H\mathbf{A})^{-1}(\mathbf{H}^H\mathbf{S}^H\mathbf{y} + 2\tau\mathbf{A}^H\mathbf{v}) \tag{3.7}$$

with $\underline{\mathbf{S}} = \mathbf{S}^H\mathbf{S}$.

Direct computation of the analytical solution (3.7) requires the inversion of a high dimensional matrix, whose computational complexity is of order $\mathcal{O}(N_h^3)$. One can think of using optimization or simulation-based methods to overcome this computational difficulty. The optimization-based methods, such as the gradient-based methods [SSXS11] or, more recently, the ADMM [NWY10] and SB [YLTV15] method approximate the solution of (3.6) by iterative updates. The simulation-based methods, e.g., the Markov Chain Monte Carlo methods [FOG15, OFG12, GMI15], are drawing samples from a multivariate posterior distribution (which is Gaussian for a Tikhonov regularization) and compute the average of the generated samples to approximate the minimum mean square error (MMSE) estimator of $\mathbf{x}$. However, simulation-based methods have the major drawback of being computationally expensive, which prevents their effective use when processing large images. Moreover, because of the particular structure of the decimation matrix, the joint operator $\mathbf{SH}$ cannot be diagonalized in the frequency domain, which prevents any direct implementation of the solution (3.7) in this domain. The main contribution in this chapter is proposing a new scheme to compute (3.7) explicitly, getting rid of any statistically sampling or iterative update and leading to a fast SR method.

In order to compute the analytical solution (3.7), a property of the decimation matrix in the frequency domain is first stated in Lemma 1.

Lemma 1 (Wei *et al.*, [WDT15b])**.** *The following equality holds*

$$\mathbf{F}\underline{\mathbf{S}}\mathbf{F}^H = \frac{1}{d}\mathbf{J}_d \otimes \mathbf{I}_{N_l} \tag{3.8}$$

where $\mathbf{J}_d \in \mathbb{R}^{d\times d}$ *is a matrix of ones,* $\mathbf{I}_{N_l} \in \mathbb{R}^{N_l\times N_l}$ *is the* $N_l \times N_l$ *identity matrix and* $\otimes$ *is the Kronecker product.*

Using the property of the matrix $\mathbf{F}\underline{\mathbf{S}}\mathbf{F}^H$ given in Lemma 1 and taking into account the assumptions mentioned above, the analytical solution (3.7) can be rewritten as

$$\hat{\mathbf{x}} = \mathbf{F}^H \left(\frac{1}{d}\underline{\mathbf{\Lambda}}^H\underline{\mathbf{\Lambda}} + 2\tau\mathbf{F}\mathbf{A}^H\mathbf{A}\mathbf{F}^H\right)^{-1}\mathbf{F}\left(\mathbf{H}^H\mathbf{S}^H\mathbf{y} + 2\tau\mathbf{A}^H\mathbf{v}\right) \tag{3.9}$$

where the matrix $\underline{\mathbf{\Lambda}} \in \mathbb{C}^{N_l\times N_h}$ is defined as

$$\underline{\mathbf{\Lambda}} = [\mathbf{\Lambda}_1, \mathbf{\Lambda}_2, \cdots, \mathbf{\Lambda}_d] \tag{3.10}$$

and where the blocks $\mathbf{\Lambda}_i \in \mathbb{C}^{N_l\times N_l}$ $(i = 1, \cdots, d)$ satisfy the relationship

$$\text{diag}\{\mathbf{\Lambda}_1, \cdots, \mathbf{\Lambda}_d\} = \mathbf{\Lambda}. \tag{3.11}$$

The readers may refer to the Appendix C.1 for more details about the derivation of (3.9) from (3.7).

To further simply the expression (3.9), we propose to use the following Woodbury inverse formula.

Lemma 2 (Woodbury formula [Hag89])**.** *The following equality holds conditional on the existence of* $\mathbf{A}_1^{-1}$ *and* $\mathbf{A}_3^{-1}$

$$\begin{aligned}&(\mathbf{A}_1 + \mathbf{A}_2\mathbf{A}_3\mathbf{A}_4)^{-1}\\ &= \mathbf{A}_1^{-1} - \mathbf{A}_1^{-1}\mathbf{A}_2(\mathbf{A}_3^{-1} + \mathbf{A}_4\mathbf{A}_1^{-1}\mathbf{A}_2)^{-1}\mathbf{A}_4\mathbf{A}_1^{-1}\end{aligned} \tag{3.12}$$

where $\mathbf{A}_1$, $\mathbf{A}_2$, $\mathbf{A}_3$ *and* $\mathbf{A}_4$ *are matrices of correct sizes.*

Taking into account the Woodbury formula of Lemma 2, the analytical solution (3.9) can be computed very efficiently as stated in the following theorem.

Theorem 1. *When Assumptions 1 and 2 are satisfied, the solution of Problem* (3.6) *can be computed using the following closed-form expression*

$$\hat{\mathbf{x}} = \frac{1}{2\tau}\mathbf{F}^H\mathbf{\Psi}\mathbf{F}\mathbf{r} - \frac{1}{2\tau}\mathbf{F}^H\mathbf{\Psi}\underline{\mathbf{\Lambda}}^H\left(2\tau d\mathbf{I}_{N_l} + \underline{\mathbf{\Lambda}}\mathbf{\Psi}\underline{\mathbf{\Lambda}}^H\right)^{-1}\underline{\mathbf{\Lambda}}\mathbf{\Psi}\mathbf{F}\mathbf{r} \tag{3.13}$$

where $\mathbf{r} = \mathbf{H}^H\mathbf{S}^H\mathbf{y} + 2\tau\mathbf{A}^H\mathbf{v}$, $\mathbf{\Psi} = \mathbf{F}\left(\mathbf{A}^H\mathbf{A}\right)^{-1}\mathbf{F}^H$ *and* $\underline{\mathbf{\Lambda}}$ *is defined in* (3.10).

Proof. See Appendix C.1. □

Complexity Analysis

The most computationally expensive part for the computation of (3.13) in Theorem 1 is the implementation of FFT/iFFT. In total, four FFT/iFFT computations are required in our implementation. Comparing with the original problem (3.7), the order of computation complexity has decreased significantly from $\mathcal{O}(N_h^3)$ to $\mathcal{O}(N_h \log N_h)$, which allows the analytical solution (3.13) to be computed efficiently. Note that [RTLF10, SKM11] also addressed image SR problems by using the properties of $\underline{\mathbf{S}}$ in the frequency domain, where N_l small matrices of size $d \times d$ were inverted. The total computational complexity of the methods investigated in [RTLF10, SKM11] is $\mathcal{O}(N_h \log N_h + N_h d^2)$. Another important difference with our work is that the authors of [RTLF10] and [SKM11] decomposed the SR problem into an upsampling (including motion estimation which is not considered in this work) and a deblurring step. The operators $\mathbf{H}$ and $\mathbf{S}$ were thus considered separately, requiring two ℓ_2 regularizations for the blurred image (referred to as $\mathbf{z}$ in [RTLF10]) and the ground-truth image (referred to as $\mathbf{x}$ in [RTLF10]). On the contrary, this work considers the blurring and downsampling jointly and achieve the SR in one step, requiring only one regularization term for the unknown image. It is worthy to mention that the proposed SR solution can be extended to incorporate the warping operator considered in [RTLF10, SKM11], which can also be modelled as a BCCB matrix. This is not included in this manuscript but will be considered in future work.

In the sequel of this section, two particular instances of the ℓ_2-norm regularization are considered, defined in the image and gradient domains, respectively.

3.3.2 Solution of the $\ell_2 - \ell_2$ problem in the image domain

First, we consider the specific case where $\mathbf{A} = \mathbf{I}_{N_h}$ and $\mathbf{v} = \bar{\mathbf{x}}$, i.e., the problem (3.6) reduces to

$$\min_{\mathbf{x}} \frac{1}{2}\|\mathbf{y} - \mathbf{S}\mathbf{H}\mathbf{x}\|_2^2 + \tau\|\mathbf{x} - \bar{\mathbf{x}}\|_2^2. \tag{3.14}$$

This implies that the target image $\mathbf{x}$ is *a priori* close to the image $\bar{\mathbf{x}}$. The image $\bar{\mathbf{x}}$ can be an estimation of the HR image, e.g., an interpolated version of the observed image, a restored image

obtained with learning-based algorithms [YWHM10] or a cleaner image obtained from other sensors [WDT15a, WDT15b, EV08]. In such case, using Theorem 1, the solution of the problem (3.14) is

$$\hat{\mathbf{x}} = \frac{1}{2\tau}\mathbf{r} - \frac{1}{2\tau}\mathbf{F}^H\underline{\mathbf{\Lambda}}^H\left(2\tau d\mathbf{I}_{N_l} + \underline{\mathbf{\Lambda}}\underline{\mathbf{\Lambda}}^H\right)^{-1}\underline{\mathbf{\Lambda}}\mathbf{F}\mathbf{r} \tag{3.15}$$

with $\mathbf{r} = \mathbf{H}^H\mathbf{S}^H\mathbf{y} + 2\tau\bar{\mathbf{x}}$.

Algorithm 2 summarizes the implementation of the proposed SR solution (3.15), which is referred to as *fast super-resolution (FSR)* approach.

Algorithm 2: FSR with ℓ_2-regularization in the image-domain: implementation of the analytical solution (3.15)

Input: $\mathbf{y}$, $\mathbf{H}$, $\mathbf{S}$, $\bar{\mathbf{x}}$, τ, d

// Factorization of $\mathbf{H}$ *(FFT of the blurring kernel)*

$\mathbf{H} = \mathbf{F}^H\mathbf{\Lambda}\mathbf{F}$;

// Compute $\underline{\mathbf{\Lambda}}$

$\underline{\mathbf{\Lambda}} = [\mathbf{\Lambda}_1, \mathbf{\Lambda}_2, \cdots, \mathbf{\Lambda}_d]$;

// Calculate FFT of $\mathbf{r}$ *denoted as* $\mathbf{Fr}$

$\mathbf{Fr} = \mathbf{F}(\mathbf{H}^H\mathbf{S}^H\mathbf{y} + 2\tau\bar{\mathbf{x}})$;

// Hadamard (or entrywise) product in frequency domain

$\mathbf{x}_f = \left(\underline{\mathbf{\Lambda}}^H\left(2\tau d\mathbf{I}_{N_l} + \underline{\mathbf{\Lambda}}\underline{\mathbf{\Lambda}}^H\right)^{-1}\underline{\mathbf{\Lambda}}\right)\mathbf{Fr}$;

// Compute the analytical solution

$\hat{\mathbf{x}} = \frac{1}{2\tau}\left(\mathbf{r} - \mathbf{F}^H\mathbf{x}_f\right)$;

Output: $\hat{\mathbf{x}}$

3.3.3 Solution of the $\ell_2 - \ell_2$ problem in the gradient domain

Generic image priors defined in the gradient domain have been successfully used for image reconstruction, avoiding the common ringing artifacts see, e.g., [SSXS08, SSXS11, TLBL10]. In this part, we focus on the gradient profile prior proposed in [SSXS11] for the single image SR problem. This prior consists of considering the regularizing term $\|\nabla\mathbf{x} - \bar{\nabla\mathbf{x}}\|_2^2$. Thus the problem (3.6) can be formulated as follows

$$\min_{\mathbf{x}} \frac{1}{2}\|\mathbf{y} - \mathbf{S}\mathbf{H}\mathbf{x}\|_2^2 + \tau\|\nabla\mathbf{x} - \bar{\nabla\mathbf{x}}\|_2^2 \tag{3.16}$$

where ∇ is the discrete version of the gradient $\nabla := [\partial_{\mathrm{h}}, \partial_{\mathrm{v}}]^T$ and $\bar{\nabla}\mathbf{x}$ is the estimated gradient field. More explanations about the motivations for using the gradient field may be found in [SSXS08, SSXS11]. For an image $\boldsymbol{x} \in \mathbb{R}^{m\times n}$, under the periodic boundary conditions, the numerical definitions of the gradient operators are

$$(\partial_{\mathrm{h}}\boldsymbol{x})(i,j) = \begin{cases} \boldsymbol{x}(i+1,j) - \boldsymbol{x}(i,j) & \text{if } i < m \\ \boldsymbol{x}(m,j) - \boldsymbol{x}(1,j) & \text{if } i = m \end{cases} \tag{3.17}$$

$$(\partial_{\mathrm{v}}\boldsymbol{x})(i,j) = \begin{cases} \boldsymbol{x}(i,j+1) - \boldsymbol{x}(i,j) & \text{if } j < n \\ \boldsymbol{x}(i,n) - \boldsymbol{x}(i,1) & \text{if } j = n \end{cases} \tag{3.18}$$

where ∂_{h} and ∂_{v} are the horizontal and vertical gradients. The gradient operators can be rewritten as two BCCB matrices $\mathbf{D}_{\mathrm{h}}$ and $\mathbf{D}_{\mathrm{v}}$ corresponding to the horizontal and vertical discrete differences of an image, respectively. Therefore, two diagonal matrices $\mathbf{\Sigma}_{\mathrm{h}}$ and $\mathbf{\Sigma}_{\mathrm{v}}$ ($\mathbb{C}^{N_h\times N_h}$) are obtained by decomposing $\mathbf{D}_{\mathrm{h}}$ and $\mathbf{D}_{\mathrm{v}}$ in the frequency domain, i.e.,

$$\mathbf{D}_{\mathrm{h}} = \mathbf{F}^H\mathbf{\Sigma}_{\mathrm{h}}\mathbf{F} \text{ and } \mathbf{D}_{\mathrm{v}} = \mathbf{F}^H\mathbf{\Sigma}_{\mathrm{v}}\mathbf{F}. \tag{3.19}$$

Thus, the problem (3.16) can be transformed into

$$\min_{\mathbf{x}} \frac{1}{2}\|\mathbf{y} - \mathbf{S}\mathbf{H}\mathbf{x}\|_2^2 + \tau\|\mathbf{A}\mathbf{x} - \mathbf{v}\|_2^2 \tag{3.20}$$

with $\mathbf{A} = [\mathbf{D}_{\mathrm{h}}^T, \mathbf{D}_{\mathrm{v}}^T] \in \mathbb{R}^{2N_h\times N_h}$ and using the notation $\bar{\nabla}\mathbf{x} = \mathbf{v} = [\mathbf{v}_{\mathrm{h}}, \mathbf{v}_{\mathrm{v}}]^T \in \mathbb{R}^{2N_h\times 1}$. Note that the invertibility of $\mathbf{A}^H\mathbf{A}$ is violated here because of the periodic boundary assumption. Thus, adding a small ℓ_2-norm regularization $\tau\sigma\|\mathbf{x}\|_2^2$ (where σ is a very small constant) to (3.20) can circumvent this invertibility problem while keeping the solution close to the original regularization. Using Theorem 1, the analytical solution of (3.20) (including the additional small ℓ_2-norm term) is given by (3.13) with $\mathbf{\Psi} = \left(\mathbf{\Sigma}_{\mathrm{h}}^H\mathbf{\Sigma}_{\mathrm{h}} + \mathbf{\Sigma}_{\mathrm{v}}^H\mathbf{\Sigma}_{\mathrm{v}} + \sigma\mathbf{I}_{N_h}\right)^{-1}$.

The pseudocode used to implement this solution is summarized in Algorithm 3.

Algorithm 3: FSR with ℓ_2-regularization in the gradient-domain: implementation of the analytical solution of (3.16)

Input: $\mathbf{y}$, $\mathbf{H}$, $\mathbf{S}$, $\mathbf{D}_\mathrm{h}$, $\mathbf{D}_\mathrm{v}$, $\bar{\nabla}\mathbf{x}$, τ, d

// Factorizations of matrices $\mathbf{H}$, $\mathbf{D}_h$, $\mathbf{D}_v$

$\mathbf{H} = \mathbf{F}^H \mathbf{\Lambda} \mathbf{F}$;

$\mathbf{D}_\mathrm{h} = \mathbf{F}^H \mathbf{\Sigma}_\mathrm{h} \mathbf{F}$;

$\mathbf{D}_\mathrm{v} = \mathbf{F}^H \mathbf{\Sigma}_\mathrm{v} \mathbf{F}$;

// Compute $\underline{\mathbf{\Lambda}}$ *and* $\mathbf{\Psi}$

$\underline{\mathbf{\Lambda}} = [\mathbf{\Lambda}_1, \mathbf{\Lambda}_2, \cdots, \mathbf{\Lambda}_d]$;

$\mathbf{\Psi} = (\mathbf{\Sigma}_\mathrm{h}^H \mathbf{\Sigma}_\mathrm{h} + \mathbf{\Sigma}_\mathrm{v}^H \mathbf{\Sigma}_\mathrm{v} + \sigma \mathbf{I}_{N_h})^{-1}$;

// Calculate FFT of $\mathbf{r}$ *denoted as* $\mathbf{Fr}$

$\mathbf{Fr} = \mathbf{F}(\mathbf{H}^H \mathbf{S}^H \mathbf{y} + 2\tau \mathbf{D}^H \mathbf{v})$;

// Hadamard (or entrywise) product in the frequency domain

$\mathbf{x}_f = \left[\mathbf{\Psi} \underline{\mathbf{\Lambda}}^H \left(\mu d \mathbf{I}_{N_l} + \underline{\mathbf{\Lambda}} \mathbf{\Psi} \underline{\mathbf{\Lambda}}^H \right)^{-1} \underline{\mathbf{\Lambda}} \mathbf{\Psi} \right] \mathbf{Fr}$;

// Compute the analytical solution

$\hat{\mathbf{x}} = \frac{1}{2\tau} \left(\mathbf{F}^H \mathbf{\Psi} \mathbf{Fr} - \mathbf{F}^H \mathbf{x}_f \right)$;

Output: $\hat{\mathbf{x}}$

3.4 Generalized fast super-resolution

As mentioned previously, a large variety of non-Gaussian regularizations has been proposed for the single image SR problem, in both image or transformed domains. Many SR algorithms, e.g., [NWY10, YLTV15], require to solve an $\ell_2 - \ell_2$ problem similar to (3.6) as an intermediate step. This section shows that the solution (3.13) derived in Section 3.3 can be combined with existing SR iterative methods to significantly lighten their computational costs.

3.4.1 General form of the proposed algorithm

In order to use the analytical solution (3.13) derived for the ℓ_2-regularized SR problem into an ADMM framework, the problem (3.4) is rewritten as the following constrained optimization problem

$$\begin{aligned} \min_{\mathbf{x},\mathbf{u}} \quad & \frac{1}{2}\|\mathbf{y}-\mathbf{SHx}\|_2^2 + \tau\phi(\mathbf{u}) \\ \text{subject to} \quad & \mathbf{Ax}=\mathbf{u}. \end{aligned} \tag{3.21}$$

The AL function associated with this problem is

$$\mathcal{L}(\mathbf{x},\mathbf{u},\boldsymbol{\lambda}) = \frac{1}{2}\|\mathbf{y}-\mathbf{SHu}\|_2^2 + \tau\phi(\mathbf{u}) + \boldsymbol{\lambda}^T(\mathbf{Ax}-\mathbf{u}) + \frac{\mu}{2}\|\mathbf{Ax}-\mathbf{u}\|_2^2$$

or equivalently

$$\mathcal{L}(\mathbf{x},\mathbf{u},\mathbf{d}) = \frac{1}{2}\|\mathbf{y}-\mathbf{SHu}\|_2^2 + \tau\phi(\mathbf{u}) + \frac{\mu}{2}\|\mathbf{Ax}-\mathbf{u}+\mathbf{d}\|_2^2. \tag{3.22}$$

To solve problem (3.21), we need to minimize $\mathcal{L}(\mathbf{x},\mathbf{u},\mathbf{d})$ w.r.t. $\mathbf{x}$ and $\mathbf{u}$ and update the scaled dual variable $\mathbf{d}$ iteratively as summarized in Algorithm 4.

Note that the 3rd step updating the HR image $\mathbf{x}$ can be solved analytically using Theorem 1. The variable $\mathbf{u}$ is updated at the 4th step using the Moreau proximity operator whose definition is given by

$$\text{prox}_{\lambda,\phi}(\boldsymbol{\nu}) = \arg\min_x \phi(\boldsymbol{x}) + \frac{1}{2\lambda}\|\boldsymbol{x}-\boldsymbol{\nu}\|^2. \tag{3.23}$$

The generic optimization scheme given in Algorithm 4, including the non-iterative update of the HR image following Theorem 1, is detailed hereafter for three widely used regularization techniques, namely for the TV regularization [NWY10], the ℓ_1-norm regularization in the wavelet domain [JJC04] and the learning-based method in [YWHM10].

3.4.2 TV regularization

Using a TV prior, problem (3.4) can be rewritten as

$$\min_{\mathbf{x}} \frac{1}{2}\|\mathbf{y}-\mathbf{SHx}\|_2^2 + \tau\phi(\mathbf{Ax}) \tag{3.24}$$

Algorithm 4: Proposed generalized fast super-resolution (FSR) scheme

Input: $\mathbf{y}$, $\mathbf{S}$, $\mathbf{H}$, d, τ;

Set $k = 0$, choose $\mu > 0$, $\mathbf{u}^0$, $\mathbf{d}^0$;

Repeat

$\mathbf{x}^{k+1} = \arg\min_{\mathbf{x}} \|\mathbf{y} - \mathbf{SHx}\|_2^2 + \mu\|\mathbf{Ax} - \mathbf{u}^k + \mathbf{d}^k\|_2^2$;

$\mathbf{u}^{k+1} = \arg\min_{\mathbf{u}} \tau\phi(\mathbf{u}) + \frac{\mu}{2}\|\mathbf{Ax}^{k+1} - \mathbf{u} + \mathbf{d}^k\|_2^2$;

$\mathbf{d}^{k+1} = \mathbf{d}^k + (\mathbf{Ax}^{k+1} - \mathbf{u}^{k+1})$;

until stopping criterion is satisfied.

where the regularization term is given by

$$\phi(\mathbf{Ax}) = \|\mathbf{x}\|_{\mathrm{TV}} = \sqrt{\|\mathbf{D}_{\mathrm{h}}\mathbf{x}\|^2 + \|\mathbf{D}_{\mathrm{v}}\mathbf{x}\|^2} \tag{3.25}$$

with $\mathbf{A} = [\mathbf{D}_{\mathrm{h}}, \mathbf{D}_{\mathrm{v}}]^T \in \mathbb{R}^{2N_h \times N_h}$. We can solve (3.24) using Algorithm 4, with the auxiliary variable $\mathbf{u} = [\mathbf{u}_{\mathrm{h}}, \mathbf{u}_{\mathrm{v}}]^T \in \mathbb{R}^{2N_h \times 1}$ such that $\mathbf{Ax} = \mathbf{u}$. The resulting fast SR algorithm can be summarized into the following iterative three-step procedure

$$\begin{aligned} &\text{For } k = 0, 1, \ldots \\ &\left\lfloor \begin{aligned} &\mathbf{x}^{k+1} \in \arg\min_{\mathbf{x}} \tfrac{1}{2}\|\mathbf{y} - \mathbf{SHx}\|_2^2 + \tfrac{\mu}{2}\|\mathbf{Ax} - \mathbf{u}^k + \mathbf{d}^k\|_2^2 \\ &\mathbf{u}^{k+1} \in \arg\min_{\mathbf{u}} \tau\sqrt{\|\mathbf{u}_{\mathrm{h}}\|^2 + \|\mathbf{u}_{\mathrm{v}}\|^2} + \tfrac{\mu}{2}\|\mathbf{Ax}^{k+1} - \mathbf{u} + \mathbf{d}^k\|_2^2 \\ &\mathbf{d}^{k+1} = \mathbf{d}^k + (\mathbf{Ax}^{k+1} - \mathbf{u}^{k+1}). \end{aligned} \right. \end{aligned} \tag{3.26}$$

The optimization problems required to update $\mathbf{x}$ and $\mathbf{u}$ at each iteration are detailed below

- Update $\mathbf{x}$: Use the closed-form expression resulting from Theorem 1 according to Algorithm 3.
- Update $\mathbf{u}$: Denoting $\boldsymbol{\nu} = [\boldsymbol{\nu}_{\mathrm{h}}, \boldsymbol{\nu}_{\mathrm{v}}] \in \mathbb{R}^{N_h \times 2}$ where $\boldsymbol{\nu}_{\mathrm{h}} = \left(\mathbf{D}_{\mathrm{h}}\mathbf{x}^{k+1} + \mathbf{d}_{\mathrm{h}}^k\right)$ and $\boldsymbol{\nu}_{\mathrm{v}} = \left(\mathbf{D}_{\mathrm{v}}\mathbf{x}^{k+1} + \mathbf{d}_{\mathrm{v}}^k\right)$, use the generalized 2D soft-shrinkage operator [NWY10] ($\mathrm{prox}_{\lambda,\|\cdot\|} : \mathbb{R}^2 \to \mathbb{R}^2$) defined as

$$\mathrm{prox}_{\lambda,\|\cdot\|}(\boldsymbol{\nu}[i]) = \max(\mathbf{0}, \|\boldsymbol{\nu}[i]\| - \tau/\mu)\frac{\boldsymbol{\nu}[i]}{\|\boldsymbol{\nu}[i]\|} \tag{3.27}$$

  where $\boldsymbol{\nu}[i]$ if the ith row of the matrix $\boldsymbol{\nu}$, $i = 1, \cdots, N_h$.

The resulting pseudocodes of the proposed fast SR approach for solving (3.24) are detailed in Algorithm **??**, which is reported in Appendix C.2.

3.4.3 ℓ_1-norm regularization in the wavelet domain

Assuming that $\mathbf{x}$ can be decomposed as a linear combination of wavelets (e.g., as in[BD06]), the SR can be conducted in the wavelet domain. Denote as $\mathbf{x} = \mathbf{W}\boldsymbol{\theta}$ the wavelet decomposition of $\mathbf{x}$, where $\boldsymbol{\theta} \in \mathbb{R}^{N_h \times 1}$ is the vector containing the wavelet coefficients and multiplying by the matrices $\mathbf{W}^H$ and $\mathbf{W}$ ($\in \mathbb{R}^{N_h \times N_h}$) represent the wavelet and inverse wavelet transforms (satisfying $\mathbf{W}\mathbf{W}^H = \mathbf{W}^H\mathbf{W} = \mathbf{I}_{N_h}$). The single image SR with ℓ_1-norm regularization in the wavelet domain can be formulated as follows

$$\min_{\mathbf{x}} \frac{1}{2}\|\mathbf{y} - \mathbf{S}\mathbf{H}\mathbf{x}\|_2^2 + \tau\|\mathbf{A}\mathbf{x}\|_1 \tag{3.28}$$

where $\mathbf{A} = \mathbf{W}^H$. By introducing the additional variable $\mathbf{u} = \mathbf{W}^H\mathbf{x}$, the problem (3.28) can be solved using Algorithm 4. The resulting fast SR algorithm can be summarized into the following iterative three-step procedure

$$\begin{array}{l} \text{For } k = 0, 1, \ldots \\ \left\lfloor \begin{array}{l} \mathbf{x}^{k+1} \in \arg\min_{\mathbf{x}} \frac{1}{2}\|\mathbf{y} - \mathbf{S}\mathbf{H}\mathbf{x}\|_2^2 + \frac{\mu}{2}\|\mathbf{A}\mathbf{x} - \mathbf{u}^k + \mathbf{d}^k\|_2^2 \\ \mathbf{u}^{k+1} \in \arg\min_{\mathbf{u}} \tau\|\mathbf{u}\|_1 + \frac{\mu}{2}\|\mathbf{A}\mathbf{x}^{k+1} - \mathbf{u} + \mathbf{d}^k\|_2^2 \\ \mathbf{d}^{k+1} = \mathbf{d}^k + (\mathbf{A}\mathbf{x}^{k+1} - \mathbf{u}^{k+1}). \end{array} \right. \end{array} \tag{3.29}$$

The optimization problems required to update $\mathbf{x}$ and $\mathbf{u}$ at each iteration are detailed below

- Update $\mathbf{x}$: Use the closed-form expression resulting from Theorem 1 according to Algorithm 2.
- Update $\mathbf{u}$: The MAP estimator of $\mathbf{u}$ can be calculated by the following soft-thresholding operator

$$\text{prox}_{\lambda,|\cdot|}(\nu) = \max(0, |\nu| - \lambda)\text{sign}(\nu) \tag{3.30}$$

  where ν is an element from the vector $\boldsymbol{\nu} = \mathbf{A}\mathbf{x} + \mathbf{d}$.

The corresponding pseudocodes of the resulting fast SR algorithm with an ℓ_1-norm regularization in the wavelet domain are detailed in Algorithm 11 proposed in Appendix C.2.

3.4.4 Learning-based ℓ_2-norm regularization

The effectiveness of the learning-based regularization for image reconstruction has been proved in several studies. In particular, Yang *et. al.* [YWHM10] solved the single image SR problem by jointly training two dictionaries for the LR and HR image patches and by applying sparse coding (SC). Interestingly, the HR image $\mathbf{x}_0$ obtained by sparse coding was projected onto the solution space satisfying (3.1), leading to the following optimization problem

$$\hat{\mathbf{x}} = \arg\min_{\mathbf{x}} \frac{1}{2}\|\mathbf{y} - \mathbf{SHx}\|_2^2 + \tau\|\mathbf{x} - \mathbf{x}_0\|_2^2. \tag{3.31}$$

This optimization problem was solved using a gradient descent approach in [YWHM10]. However, it can benefit from the analytical solution provided by Theorem 1 that can be implemented using Algorithm 2.

3.5 Experimental Results

This section demonstrates the efficiency of the proposed fast SR strategy by testing it on various images with different regularization terms. The performance of the single image SR algorithms is evaluated in terms of reconstruction quality and computational complexity. Given the ability of our algorithm to solve the SR problem with less complexity than the existing methods, one may expect a gain in computational time and convergence properties. All the experiments were performed using MATLAB 2013A on a computer with Windows 7, Intel(R) Core(TM) i7-4770 CPU @3.40GHz and 8 GB RAM. It is interesting to note that the proposed algorithm is not just applicable to the ultrasound images, but is also appropriate for the natural images. Color images were processed using the illuminate channel only, as in [YWHM10]. Precisely, the RGB images were transformed into YUV coordinates and the color channels (Cb,Cr) were up-sampled using bicubic interpolation. In the illuminate channel, the HR image was blurred and down-sampled in each spatial direction with factors d_r and d_c. The resulting blurred and decimated images were then contaminated by AWGN of variance σ_n^2 with a blurred-signal-to-noise ratio defined by

$$\text{BSNR} = 10\log_{10}\left(\frac{\|\mathbf{SHx} - E(\mathbf{SHx})\|_2^2}{N\sigma_n^2}\right) \tag{3.32}$$

where N is the total number of pixels of the observed image and $E(\cdot)$ is the arithmetic mean operator.

Unless explicitly specified, the blurring kernel is a 2D-Gaussian filter of size 9×9 with variance $\sigma_h^2 = 3$, the decimation factors are $d_r = d_c = 4$ and the noise level is BSNR $= 30$dB.

The performances of the different SR algorithms are evaluated both visually and quantitatively in terms of the following metrics: RMSE, PSNR, ISNR and MSSIM. The definitions of these metrics, widely used to evaluate image reconstruction methods, have been given in Chapter 2. Note that the observation $\mathbf{y}$ has to be interpolated (bicubic interpolation is implemented here) to have the same size as the HR image when calculating the ISNR for SR problems. Note also that it is not appropriate to compute the ISNR for bicubic interpolation since it is always 0.

3.5.1 Fast SR using ℓ_2-regularizations

$\ell_2 - \ell_2$ model in the image domain

- Gaussian blurring kernel

  We first explore the single image SR problem with the "pepper" image and standard Tikhonov regularization corresponding to the optimization problem formulated in (3.14). The size of the ground truth HR image shown in Fig. 3.2(b) is 512×512. Fig. 3.2 also displays the restored images with bicubic interpolation, the proposed analytical solution given in Algorithm 2 and the ADMM of [NWY10] adapted to a Gaussian prior. The prior mean image $\bar{\mathbf{x}}$ (approximated HR image) is the up-sampled version/bicubic interpolation of the LR image (Case 1) with restoration results in Figs. 3.2(d) and 3.2(e), whereas $\bar{\mathbf{x}}$ is the ground truth (Case 2) with restoration results in Figs. 3.2(f) and 3.2(g). The regularization parameter was $\tau = 1$ in Case 1 and $\tau = 0.1$ in Case 2. The numerical results corresponding to this experiment are summarized in Table 3.1. The visual impression and the numerical results show that the reconstructed HR images obtained with our method are similar to those obtained with ADMM. However, the proposed FSR method performs much faster than ADMM. More precisely, the computational time with our method is divided by a factor of 60 for Case 1 and by a factor of 80 for Case 2. Note also that the restored images obtained with Case 2 ($\bar{\mathbf{x}}$ is the ground truth) are visually much better than the ones obtained with Case 1 ($\bar{\mathbf{x}}$ is the interpolated LR image), as expected.

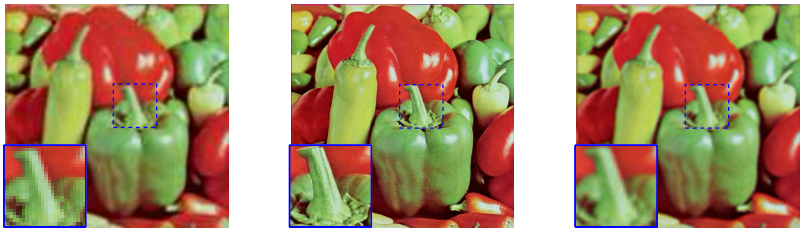

(a) Observation† (b) Ground truth (c) Bicubic interpolation

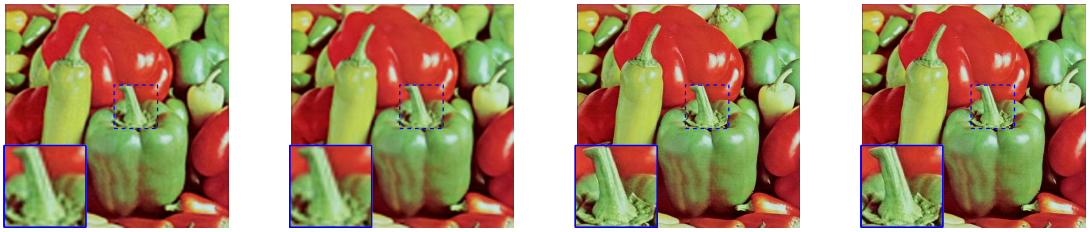

(d) Case 1: ADMM (e) Case 1: Algorithm 2 (f) Case 2: ADMM (g) Case 2: Algorithm 2

Figure 3.2: SR of the pepper image when considering an $\ell_2 - \ell_2$-model in the image domain: visual results. The prior image mean $\bar{\mathbf{x}}$ is defined as the bicubic interpolated LR image in Case 1 and as the ground truth HR image in Case 2.

†Note that the LR images have been scaled for better visualization in the figures of this chapter (i.e., the actual LR images contain d times fewer pixels than the corresponding HR images).

Table 3.1: SR assessment of the pepper image when considering an $\ell_2 - \ell_2$-model in the image domain.

Method	PSNR (dB)	ISNR (dB)	MSSIM	Time (s.)
Bicubic	25.37	-	0.59	0.002
Case 1				
ADMM	29.26	4.01	0.67	1.92
Algorithm 2	29.27	4.01	0.67	**0.02**
Case 2				
ADMM	53.84	29.27	1	0.5
Algorithm 2	53.74	29.55	1	**0.02**

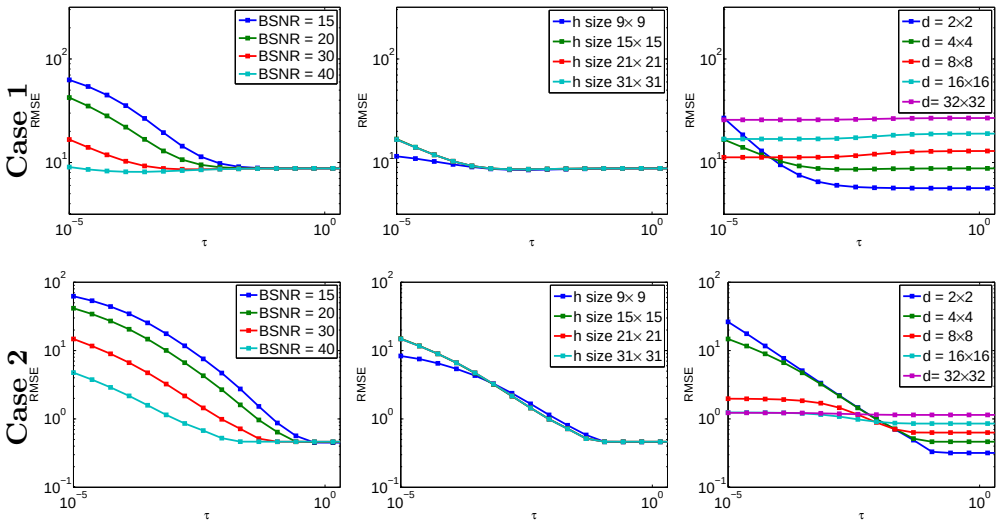

Figure 3.3: SR of the "pepper" image when considering the $\ell_2 - \ell_2$ model in the image domain: RMSE as functions of the regularization parameter τ for various noise levels (1st column), blurring kernel sizes (2nd column) and decimation factors (3rd column). The results in the 1st column were obtained for $d_r = d_c = 4$ and 9×9 kernel size; in the 2nd column, $d_r = d_c = 4$ and BSNR= 30 dB; in the 3rd column, the kernel size was 9×9 and BSNR= 30 dB.

The performance of the proposed method has been also evaluated with various experimental parameters, namely, the BSNR level, the size of the blurring kernel and the decimation factors. The corresponding RMSEs are depicted in Figs. 3.3 as functions of the regularization parameter τ for the two considered scenarios (Cases 1 and 2). Note that the same performance is obtained by the ADMM-based SR technique since it solves the same optimization problem.

- Motion blurring kernel

  This paragraph considers a dataset composed of images that have been captured by a camera placed on a tripod, whose Z-axis rotation handle has been locked and X- and Y-axis rotation handles have been loosen [LWDF09]. The corresponding dataset is available online[1]. The observed LR image, motion kernel and corresponding SR results are shown in Figs. 3.4. The size of the motion kernel is 19×19. As in the previous paragraph, the prior image $\bar{\mathbf{x}}$ is

[1] Available online at http://www.wisdom.weizmann.ac.il/~levina/papers/LevinEtalCVPR09Data.zip

the bicubic interpolation of the LR image in Case 1, while $\bar{\mathbf{x}}$ is the ground truth in Case 2. The regularization parameter is set to $\tau = 0.01$ and $\tau = 0.1$ in Cases 1 and 2, respectively. Quantitative results are reported in Table 3.2 and show that the proposed method provides competitive results w.r.t. the other methods, while being more computational efficient.

(a) Observation† (b) Ground truth (c) Bicubic interpolation

(d) Case 1: ADMM (e) Case 1: Algorithm 2 (f) Case 2: ADMM (g) Case 2: Algorithm 2

Figure 3.4: SR of the motion blurred image when considering an $\ell_2 - \ell_2$-model in the image domain: visual results. The prior image mean $\bar{\mathbf{x}}$ is defined as the bicubic interpolated LR image in Case 1 and as the ground truth HR image in Case 2.

$\ell_2 - \ell_2$ model in the gradient domain

This section compares the performance of the proposed fast SR strategy with the gradient profile regularization proposed in [SSXS08]. As shown in Section 3.3.1, Theorem 1 allows an analytical SR solution to be computed. The "face" image (of size 276×276) shown in Fig. 3.5 (b) was used for these tests. In this experiment, $\bar{\nabla}\mathbf{x}$ was calculated using the reference HR image and the regularization parameters were set to $\tau = 10^{-3}$ and $\sigma = 10^{-8}$. The proposed method is compared with the ADMM and the CG method (instead of the gradient descent (GD) method initially proposed in [SSXS11] since CG has shown to be much more efficient than GD in this experiment). The restored images using

Table 3.2: SR assessment of the motion blurred image using an $\ell_2 - \ell_2$-model in the image domain.

Method	PSNR (dB)	ISNR (dB)	MSSIM	Time (s.)
Bicubic	21.15	-	0.91	0.002
Case 1				
ADMM	27.11	5.96	0.96	0.11
Algorithm 2	27.11	5.96	0.96	**0.01**
Case 2				
ADMM	53.23	32.08	1	0.42
Algorithm 2	53.23	32.08	1	**0.01**

bicubic interpolation, ADMM, the CG method and the proposed Algorithm 3 are shown in Fig. 3.5. The corresponding numerical results are reported in Table 3.3. These results illustrate the superiority of the approach in terms of computational time. This significant difference can be explained by the non-iterative nature of the proposed method compared to CG and ADMM. Moreover, all the three methods converge to the same global minima as shown by the objective curves in Fig. 3.6. The convergence of the objective curves is in agreement with the visual and numerical results.

Table 3.3: SR of the face image when considering an $\ell_2 - \ell_2$-model in the gradient domain: quantitative results.

Method	PSNR (dB)	ISNR (dB)	MSSIM	Time (s.)
Bicubic	26.84	-	0.49	0.001
ADMM	42.82	15.98	0.98	0.71
CG	42.82	15.98	0.98	0.35
Algorithm 3	42.82	15.98	0.98	**0.009**

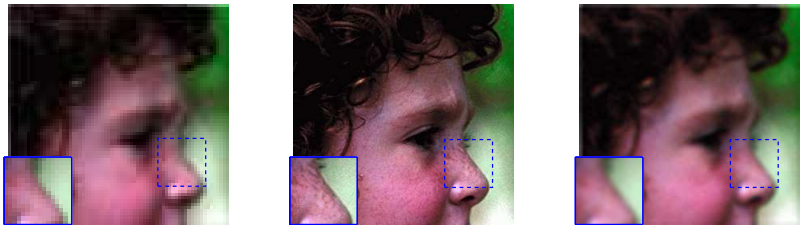

(a) Observation† (b) Ground truth (c) Bicubic interpolation

(d) ADMM (e) CG [SSXS08] (f) Algorithm 3

Figure 3.5: SR of the face image when considering an $\ell_2 - \ell_2$-model in the gradient domain: visual results.

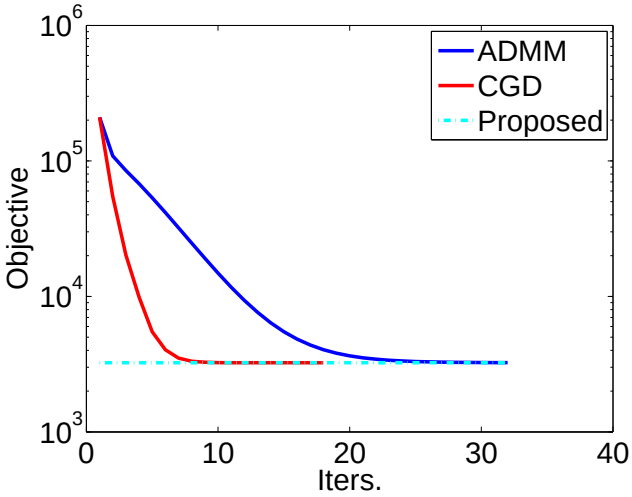

Figure 3.6: SR of the face image when considering an $\ell_2 - \ell_2$-model in the gradient domain: objective functions.

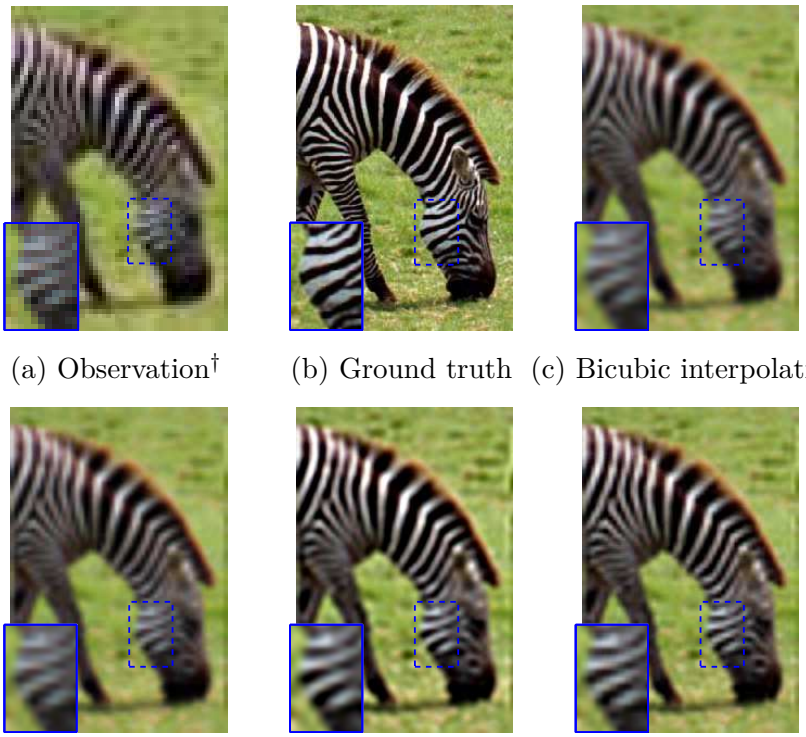

(a) Observation† (b) Ground truth (c) Bicubic interpolation

(d) SC [YWHM10] (e) SC+GD [YWHM10] (f) SC+Algorithm 2

Figure 3.7: SR of the face image when considering an $\ell_2 - \ell_2$-model in the gradient domain: visual results.

Learning-based ℓ_2-norm regularization

This section studies the performance of the algorithm obtained when the analytical solution of Theorem 1 is embedded in the learning-based method of [YWHM10]. The method investigated in [YWHM10] computed an initial estimation of the HR image via sparse coding (SC) and used a back-projection (BP) procedure to improve the SR performance. The BP operation was performed by a GD method in [YWHM10]. Here, this GD step has been replaced by the analytical solution provided by Theorem 1 and Algorithm 2. The image "zebra" was used in this experiment to compare the performance of both algorithms[2]. The LR and HR images (of size 300×200) are shown

[2]For comparison purpose, the authors used the MATLAB code corresponding to [YWHM10] available at `http://www.ifp.illinois.edu/~jyang29.`

in Fig. 3.7 (a) and 3.7 (b). The regularization parameter was set to $\tau = 0.1$. The restored images shown in Figs. 3.7 (c)-(f) were obtained using the initial SC estimation proposed in [YWHM10], the back-projected SC image combined with the gradient descent (GD) algorithm of [YWHM10] (referred to as "SC + GD") and the proposed closed-form solution (referred to as "SC + Algorithm 2"). The corresponding numerical results are reported in Table 3.4. The restored images obtained with the two back-projection approaches are clearly better than the restoration obtained with the SC method. While the quality of the images obtained with these projection approaches is similar, the use of the analytical solution of Theorem 1 allows the computational cost of the GD step to be reduced significantly.

Table 3.4: SR of the zebra image when considering a learning-based ℓ_2-norm regularization: quantitative results.

Method	PSNR (dB)	ISNR (dB)	MSSIM	Time (s.)
Bicubic	18.98	-	0.37	0.001
SC [YWHM10]	19.15	0.16	0.38	170.9
SC+GD [YWHM10]	20.76	1.78	0.47	170.9+1.23
SC+Algorithm 2	29.99	1.88	0.48	170.9+**0.01**

3.5.2 Natural images: Embedding the $\ell_2 - \ell_2$ analytical solution into the ADMM

In this second group of experiments, we consider two non-Gaussian priors that have been widely used for image reconstruction problems: the TV regularization in the spatial domain and the ℓ_1-norm regularization in the wavelet domain. In both cases, the analytical solution of Theorem 1 is embedded into a standard ADMM algorithm inspired from [NWY10] (the resulting algorithms referred to as Algorithms 10 and 11 are detailed in Appendix C.2). The stopping criterion for both implementations is chosen as the relative cost function error defined as

$$\frac{|f(\mathbf{x}^{k+1}) - f(\mathbf{x}^k)|}{f(\mathbf{x}^k)} \tag{3.33}$$

where $f(\mathbf{x}) = \frac{1}{2}\|\mathbf{y} - \mathbf{SHx}\|_2^2 + \tau\phi(\mathbf{Ax})$. Note that other stopping criteria such as those studied in [BPC+11b] could also be investigated. The 512×512 images "Lena", "monarch" and "Barbara" were considered in these experiments. The observed LR images and the HR images (ground truth) are displayed in Fig. 3.8 (first two columns).

TV-regularization

The regularization parameter was manually fixed (by cross validation) to $\tau = 2 \times 10^{-3}$ for the image "Lena", to $\tau = 1.8 \times 10^{-3}$ for the image "monarch" and to $\tau = 2.5 \times 10^{-3}$ for the image "Barbara". Figs. 3.8 show the SR results obtained using the bicubic interpolation (third column), ADMM based algorithm of [NWY10] (fourth column) and Algorithm 10 (last column). As expected, the ADMM reconstructions perform much better than a simple interpolation of the LR image that is not able to solve the upsampling and deblurring problem. The results obtained with the proposed algorithm and with the method of [NWY10] are visually very similar. This visual inspection is confirmed by the quantitative results provided in Table 3.5. However, the proposed algorithm has the advantage of being much faster than the algorithm of [NWY10] (with computational times reduced by a factor larger than 2). Moreover, Fig. 3.9 illustrates the convergence of the two algorithms. The proposed single image SR algorithm (Algorithm 10) converges faster and with less fluctuations than the algorithm of [NWY10]. This result can be explained by the fact that the algorithm in [NWY10] requires to handle more variables in the ADMM scheme than the proposed algorithm.

ℓ_1-norm regularization in the wavelet domain

This section evaluates the performance of Algorithm 11, which is compared with a generalization of the method proposed in [NWY10] to an ℓ_1-norm regularization in the wavelet domain. The motivations for working in the wavelet domain are essentially to take advantage of the sparsity of the wavelet coefficients. All experiments were conducted using the discrete Haar wavelet transform and the Rice wavelet toolbox [BCN+]. For both implementations, the regularization parameter was adjusted by cross validation, leading to $\tau = 2 \times 10^{-4}$ for the image "Lena", $\tau = 1.8 \times 10^{-4}$ for the image "Monarch" and $\tau = 2.5 \times 10^{-4}$ for the image "Barbara".

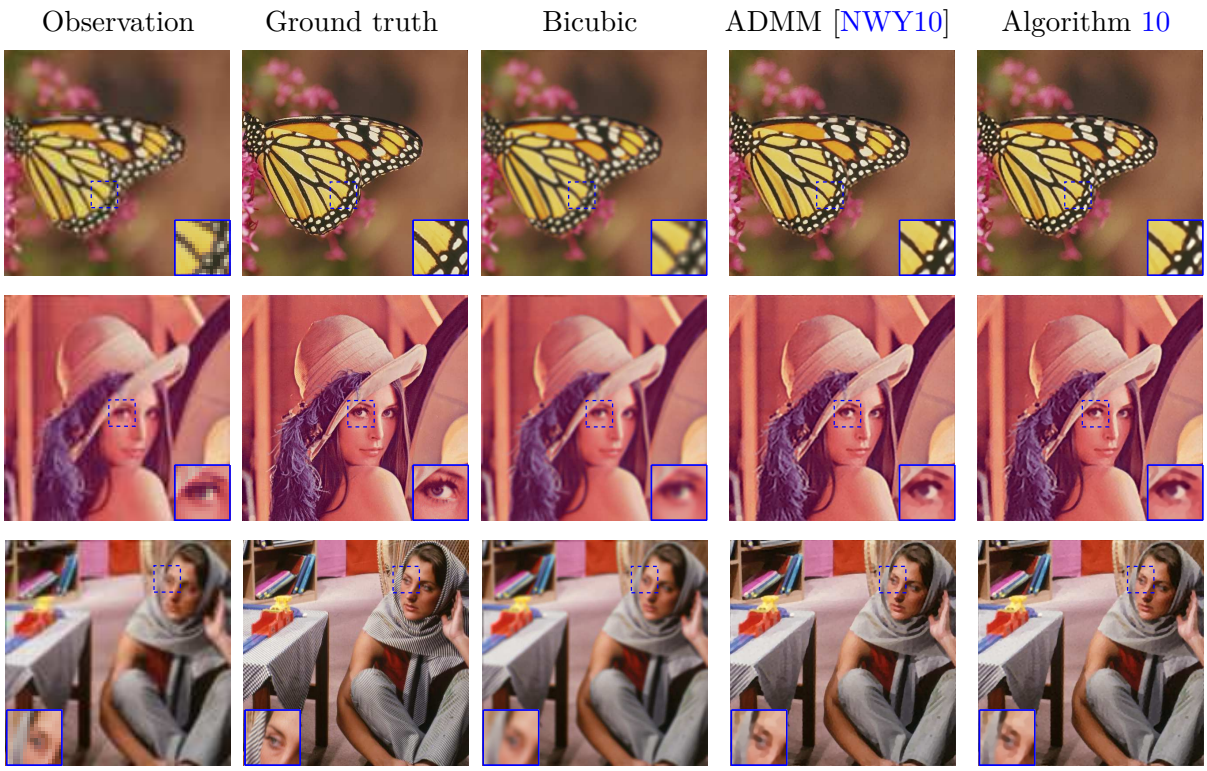

Figure 3.8: SR of the Monarch, Lena and Barbara images when considering a TV-regularization: visual results.

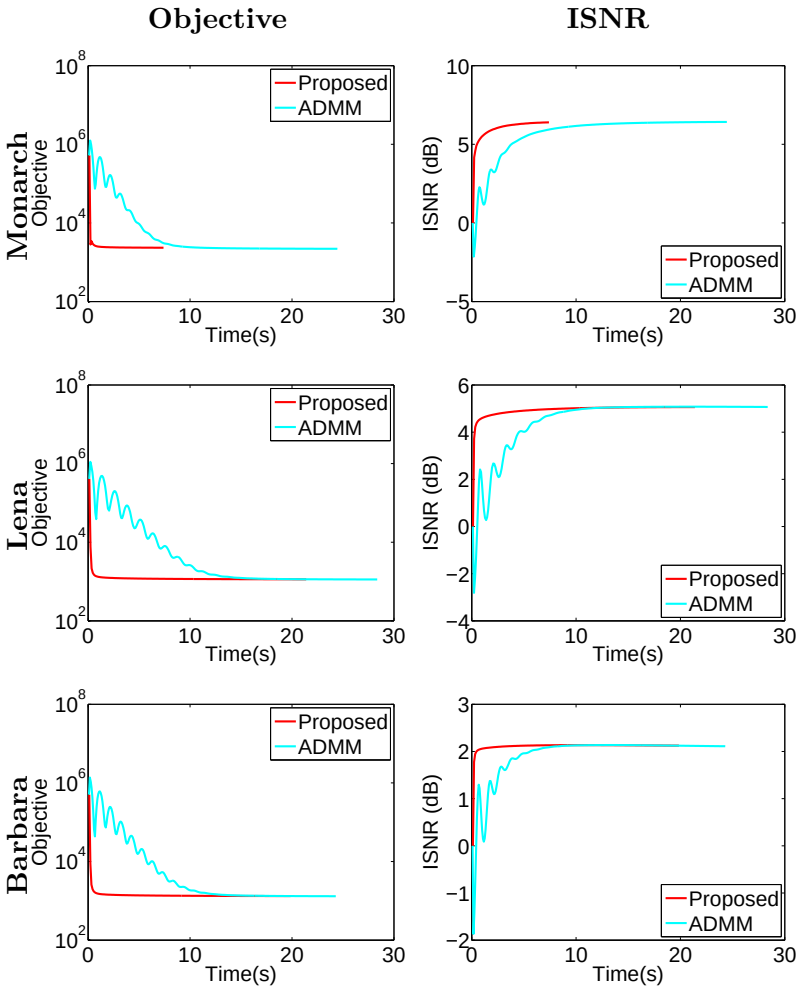

Figure 3.9: SR of the Monarch, Lena and Barbara images when considering a TV-regularization: objective function (left) and ISNR (right) vs time.

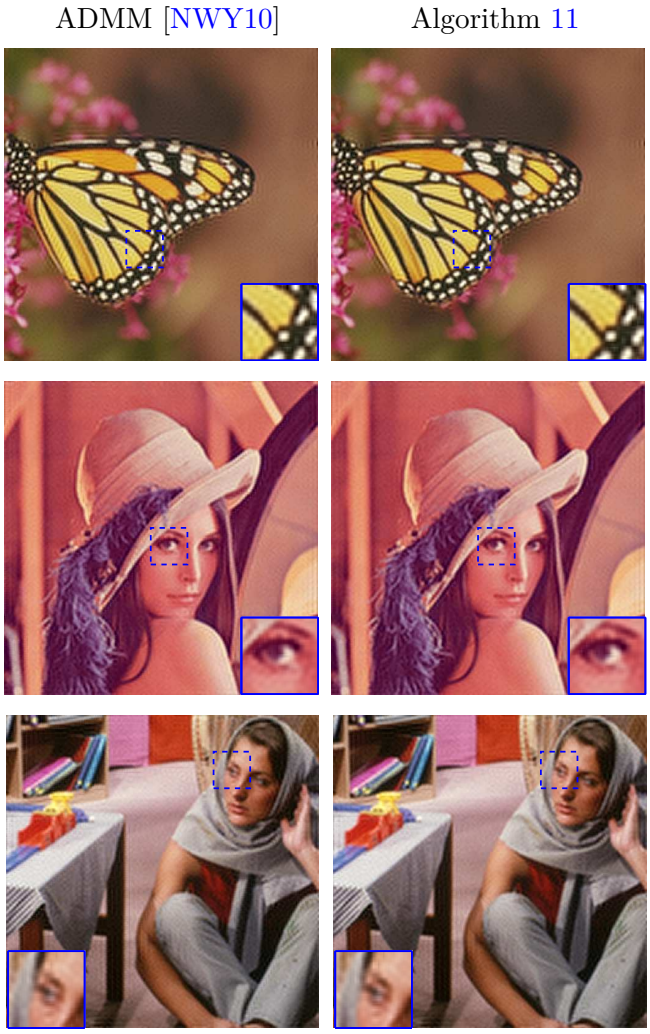

Figure 3.10: SR of the Monarch, Lena and Barbara images when considering a ℓ_1-norm regularization in the wavelet domain: visual results.

Table 3.5: SR of the Monarch, Lena and Barbara images when considering a TV-regularization: quantitative results.

Image	Method	PSNR (dB)	ISNR (dB)	MSSIM	Time (s)	Iter.
Monarch	Bicubic	23.11	-	0.75	0.002	-
	ADMM [NWY10]	29.49	6.38	0.84	78.95	812
	Algorithm 10	29.38	6.28	0.83	**19.81**	**170**
Lena	Bicubic	25.80	-	0.57	0.002	-
	ADMM [NWY10]	30.81	5.00	0.66	35.67	372
	Algorithm 10	30.91	5.11	0.66	**20.63**	**164**
Barbara	Bicubic	22.71	-	0.48	0.002	-
	ADMM [NWY10]	24.80	2.09	0.56	13.85	148
	Algorithm 10	24.84	2.13	0.56	**8.36**	**73**

Figs. 3.10 show some SR reconstruction results with an ℓ_1-norm minimization in the wavelet domain. The HR images obtained with Algorithm 11 and with the algorithm of [NWY10] adapted to the ℓ_1-norm prior are visually similar and better than a simple interpolation. The numerical results shown in Table 3.6 confirm that the two algorithms provide similar reconstruction performance. However, as in the previous case (TV regularization), the proposed algorithm is characterized by much smaller computational times than the standard ADMM implementation. The faster and smoother convergence obtained with the proposed method (Algorithm 11) can be observed in Fig. 3.11. Note that the fluctuations of the objective function and PSNR values (versus the number of iterations) obtained with the method of [NWY10] are due to the variable splitting, which requires more variables and constraints to be handled than for the proposed method.

Table 3.6: SR of the Monarch, Lena and Barbara images when considering a ℓ_1-norm regularization in the wavelet domain: quantitative results.

Image	Method	PSNR (dB)	ISNR (dB)	MSSIM	Time (sec.)	Iter.
Monarch	Bicubic	23.11	-	0.75	0.002	-
	ADMM [NWY10]*	27.08	3.97	0.74	34.08	400
	Algorithm 11	27.13	4.03	0.74	**15.02**	**177**
Lena	Bicubic	25.80	-	0.57	0.002	-
	ADMM [NWY10]	30.09	4.29	0.62	38.48	450
	Algorithm 11	30.21	4.41	0.63	**14.25**	**164**
Barbara	Bicubic	22.71	-	0.48	0.002	-
	ADMM [NWY10]	24.66	1.95	0.52	34.13	400
	Algorithm 11	24.70	2.00	0.53	**14.83**	**171**

*The algorithm of [NWY10] was originally proposed for SR using a TV regularization. This algorithm has been modified by the authors to solve the ℓ_1-norm penalized optimization problem.

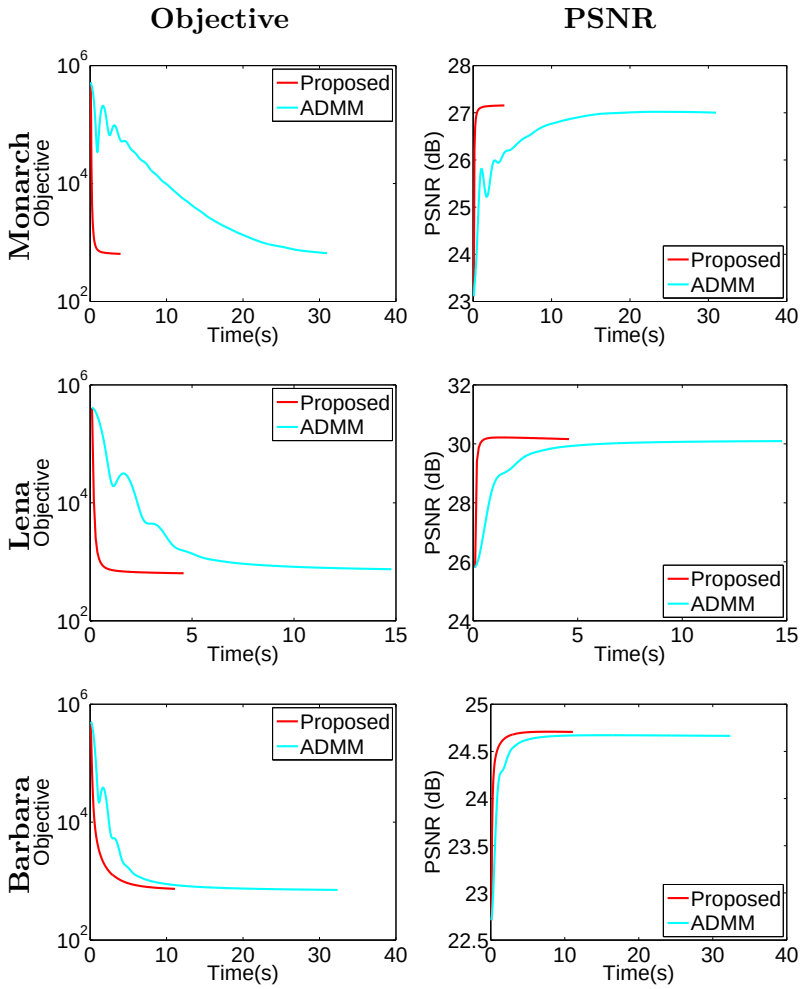

Figure 3.11: SR of the Monarch, Lena and Barbara images when considering an ℓ_1-norm regularization in the wavelet domain: objective function (left) and PSNR (right) vs time.

3.5.3 Medical ultrasound images: Embedding the $\ell_2 - \ell_2$ analytical solution into the ADMM framework

Finally, the proposed SR algorithm was tested on *in vivo* US data using ℓ_p-norm regularization. The image displayed in Fig. 3.12(a) is a mouse kidney image acquired with a probe of 25MHz central frequency. We carried out SR experiments on the region located inside the red box, shown in Fig. 3.12(b). The up-sampling factors were set to $d_r = d_c = 2$. The PSF was estimated directly from the data following [MA03]. The regularization parameter τ was set to 0.1 in this section. For the real data, we compared the proposed algorithm with a classical ADMM implementation [MBK12]. The restored images obtained with the proposed method are shown in Figs. 3.12(c)-(f), while the ones estimated with the classical method are shown in Figs. 3.12(g)-(j). The numerical results are reported in Table 3.7. According to the graphical and numerical results, the restored images with the proposed algorithm and the classical method are similar in terms of RG. However, the proposed algorithm needs less CPU time and a reduced number of iterations (when compared to the classical method) to converge.

Table 3.7: SR of the real US image

ℓ_p	Method	RG	Time (s)	Iters.
$p = 2$	Proposed	1.78	**0.009**	-
	Classical	1.78	0.53	55
$p = 1$	Proposed	**16.26**	**2.42**	190
	Classical	**16.50**	2.58	199
$p = \frac{4}{3}$	Proposed	9.72	**0.76**	28
	Classical	10.04	1.12	37
$p = \frac{3}{2}$	Proposed	5.55	**0.31**	14
	Classical	5.72	0.75	33

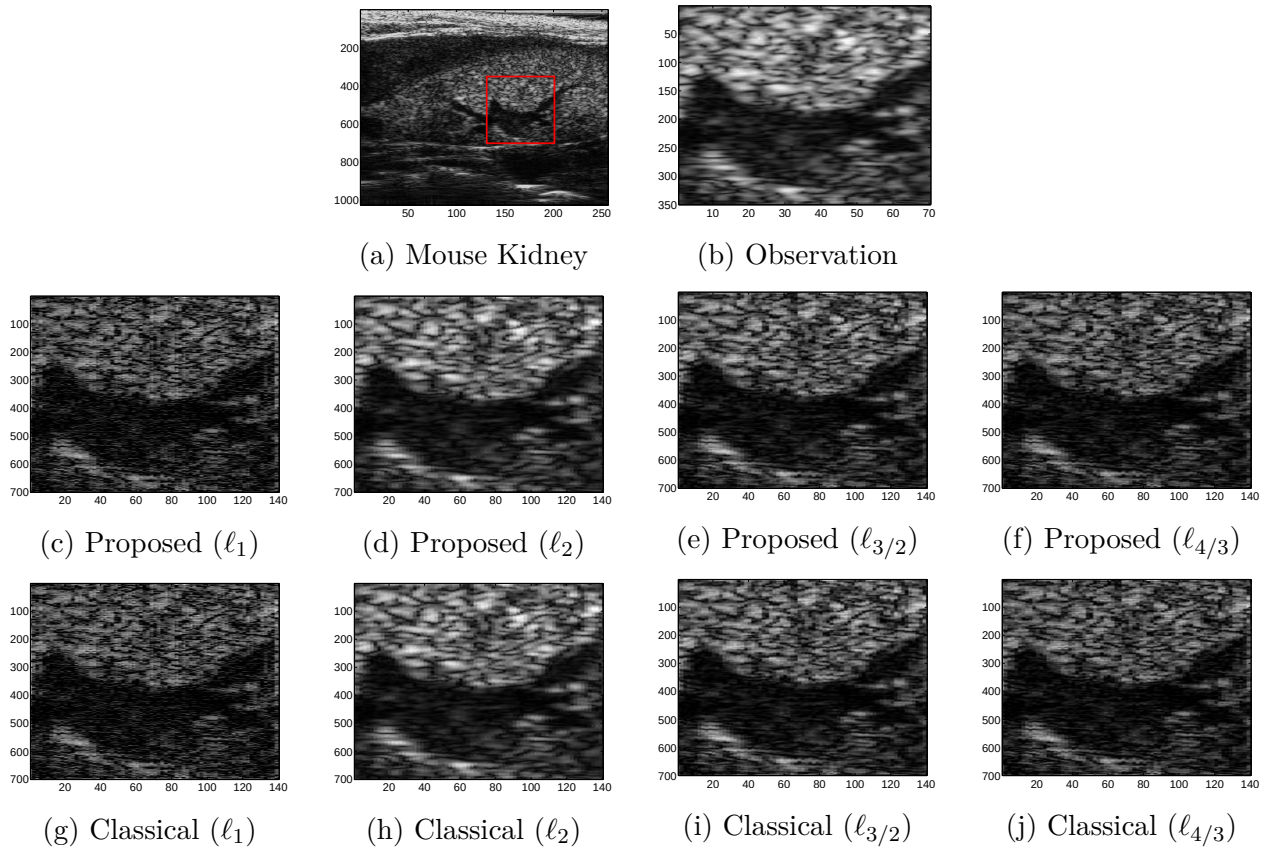

(a) Mouse Kidney (b) Observation

(c) Proposed (ℓ_1) (d) Proposed (ℓ_2) (e) Proposed ($\ell_{3/2}$) (f) Proposed ($\ell_{4/3}$)

(g) Classical (ℓ_1) (h) Classical (ℓ_2) (i) Classical ($\ell_{3/2}$) (j) Classical ($\ell_{4/3}$)

Figure 3.12: *In vivo* US image and the restored images with the proposed and classical methods using ℓ_p norm regularizers.

3.6 Conclusion

This chapter studies a new fast single image super-resolution framework based on the widely used image formation model. The proposed super-resolution approach computed the super-resolved image efficiently by exploiting intrinsic properties of the decimation and the blurring operators in the frequency domain. A large variety of priors can be handled in the proposed super-resolution scheme for both medical ultrasound and natural images. Specifically, when considering an ℓ_2-regularization, the target image was computed analytically, getting rid of any iterative steps. For more complex priors (i.e., non ℓ_2-regularization), variable splitting allowed this analytical solution to be embedded into the augmented Lagrangian framework, thus accelerating various existing schemes for single image super-resolution. Results on several medical ultrasound and natural images confirmed the computational efficiency of the proposed approach and showed its fast and smooth convergence.

Chapter 4

Blind-deconvolution of ultrasound images

Part of this chapter has been adapted from the conference papers [ZBKT15] and [ZWB+16b].

Contents

4.1 Introduction 103
4.2 Blind deconvolution using a Gaussian prior for the PSF 105
4.2.1 Hierarchical Bayesian model 105
4.2.2 Hybrid Gibbs Sampler 108
4.2.3 Simulation results 110
4.3 Blind deconvolution using a parametric model for the PSF 114
4.3.1 Parametric model of the PSF 114
4.3.2 Optimization Problem Formulation 116
4.3.3 BCD-based algorithms 117
4.3.4 Simulation results 121
4.4 Conclusion 123

4.1 Introduction

The linear model considered in the introduction and Chapter 2 was given by

$$\mathbf{y} = \mathbf{H}\mathbf{x} + \mathbf{n}. \tag{4.1}$$

where the vectors $\mathbf{y}$, $\mathbf{x}$ and $\mathbf{n}$ are the tissue reflectivity function (TRF) to be estimated, the observed RF ultrasound image and the measurement noise respectively, the huge matrix $\mathbf{H}$ is associated with the system point spread function (PSF). Several blind or semi-blind deconvolution methods have been previously proposed in the ultrasound literature using the linear model (4.1), see e.g., [CE07]. The

existing methods for ultrasound image blind deconvolution can be roughly divided into two categories. The first group involves a pre-estimation of the PSF, followed by one of the classical non-blind deconvolution algorithms. The homomorphic filter technique [JL94, Tax95, MA01] is a traditional method for the PSF estimation, which falls into this group. More recently, a hybrid method based on inverse filtering for PSF estimation has been explored [MT07, DM11]. The second class of blind deconvolution algorithms includes simultaneously estimation of the PSF and the ultrasound image. Most of the existing works fall in group 2 are using non-parametric model for the PSF estimation, see e.g., [JT08, YZX12a, RPD+15].

In this chapter, we follow the second category to estimate the ultrasound TRF and the PSF jointly. In order to estimate the PSF, two strategies are studied in this chapter. First, a Gaussian prior is proposed for the PSF and the blind deconvolution problem is formulated in a Bayesian framework. An MCMC technique is proposed to jointly estimate the PSF and the ultrasound TRF due to the intractability of the target distribution. Second, a parametric model for the US imaging system PSF is proposed. This model requires a few parameters to be estimated instead of all the PSF. The formulated problem in an optimization framework is then solved using a block-coordinate based iterative method.

Considering the ill-posedness of US image deconvolution problem, different regularization terms for the US TRF based on their *a priori* knowledge are derived in order to regularize the ill-posed problem [MR15]. Several widely considered regularizers include the Laplace distribution [MT07, YZX12a], the Gaussian distribution [JT08], the TV regularizer [MBK12] and the Huber model recently proposed in [MR15]. However, the ℓ_2-norm regularized optimization problem always produces over-smoothed results, the TV method produces piecewise smooth results, and the ℓ_1-norm regularized optimization method is known to yield sparse results [YZX12a]. In this chapter, a generalized Gaussian distribution/ℓ_p-norm ($0 < p \leqslant 2$) regularization term is proposed for the US TRF [ZWB+16b], which has been shown to be relative to US RF images [Ale10]. Moreover, it contains the traditional Gaussian and Laplacian regularization terms.

4.2 Blind deconvolution using a Gaussian prior for the PSF

Following the problem formulation in Chapter 2, we first study the case of a Gaussian prior for the PSF. Moreover, a mixture of generalized Gaussian distributions based on a hidden label field is proposed for the US TRF as in Chapter 2.

Given the linear US image formation model (4.1), an efficient implementation of the matrix-vector product is obtained by using the direct and inverse Fourier transforms as follows

$$\mathbf{H}\mathbf{x} = \mathbf{F}^T[\mathbf{F}\mathbf{h}. * \mathbf{F}\mathbf{x}] = \mathbf{F}^T[\tilde{\mathbf{h}}. * \tilde{\mathbf{x}}] \tag{4.2}$$

where the matrices $\mathbf{F}$ and $\mathbf{F}^T$ correspond to Fourier and inverse Fourier transforms, $.*$ is the Hadamard product, $\mathbf{h}$ is the first row of $\mathbf{H}$ and $\tilde{\boldsymbol{\phi}} = \mathbf{F}\boldsymbol{\phi}$ is the Fourier transform of the vector $\boldsymbol{\phi}$. The relation (4.2) is based on the property of circulant matrices (which has been illustrated in Appendix A), i.e., $\mathbf{H} = \mathbf{F}^T\boldsymbol{\Sigma}_{\boldsymbol{H}}\mathbf{F}$, where $\boldsymbol{\Sigma}_{\boldsymbol{H}} = \text{diag}(\tilde{\mathbf{h}})$. The goal of the blind deconvolution problem studied here is to estimate the reflectivity image $\mathbf{x}$ and the PSF $\mathbf{h}$ by using a hierarchical Bayesian model. It is interesting to note that this work is an extension of [ZBKT16], where the PSF was estimated in a pre-processing step.

4.2.1 Hierarchical Bayesian model

The hierarchical Bayesian model proposed in this work requires to define appropriated prior distributions for the unknown vector $\boldsymbol{\Theta} = (\mathbf{x}, \mathbf{h})$. The joint posterior distribution of $\boldsymbol{\Theta}$ can then be calculated from the product of the likelihood function and the prior distributions. The likelihood function and the prior distributions considered in this section are then investigated.

Likelihood

Assuming an AWGN sequence with covariance matrix $\sigma_n^2\mathbf{I}_{N\times N}$, the likelihood function associated with model (4.1) is

$$p(\mathbf{y}|\boldsymbol{\Theta}) = \frac{1}{(2\pi\sigma_n^2)^{N/2}} \exp\left(-\frac{1}{2\sigma_n^2}\|\mathbf{y} - \mathbf{H}\mathbf{x}\|_2^2\right) \tag{4.3}$$

where $\|\cdot\|_2$ is the usual ℓ_2-norm.

Priors

A. Reflectivity image: As stated in Chapter 2, we assume that the pixels of the US image are independent random variables distributed according to generalized Gaussian distributions (GGDs) as in Chapter 2. Moreover, the pixels of the US image belonging to different homogeneous regions are supposed to be distributed according to GGDs with different parameters. This assumption makes sense in applications such as tumor detection, where the tumor and the image background are characterized by different sets of parameters. Precisely, we introduce a label vector $\mathbf{z} \in \mathbb{R}^{N\times 1}$ to map the image into the different homogeneous regions. The ith label is such that $z_i = k$ if and only if the corresponding pixel x_i belongs to the class $k \in \{1, ..., K\}$. The conditional distribution of the pixel x_i is defined as

$$x_i|z_i = k \sim \mathcal{GGD}(\xi_k, \gamma_k)$$

where ξ_k and γ_k are the shape and scale parameters of the kth class. Conditioned on the label vector, we obtain the following prior for the reflectivity image

$$p(\mathbf{x}|\mathbf{z}, \boldsymbol{\xi}, \boldsymbol{\gamma}) = \prod_{k=1}^{K} \frac{1}{\left[2\gamma_k^{1/\xi_k}\Gamma(1+1/\xi_k)\right]^{N_k}} \exp\left(-\frac{\|\mathbf{x}_k\|_{\xi_k}^{\xi_k}}{\gamma_k}\right) \tag{4.4}$$

where $\|\mathbf{x}_k\|_\xi = (\sum_{i=1}^{N_k} |x_i|^\xi)^{1/\xi}$ denotes the ℓ_ξ-norm, $\mathbf{x}_k$ contains all the pixels assigned to class k, the shape and scale parameter vectors are denoted as $\boldsymbol{\xi} = (\xi_1, ..., \xi_K)$ and $\boldsymbol{\gamma} = (\gamma_1, ..., \gamma_K)$ with $\gamma_k = \left[\sqrt{\sigma_k^2\Gamma(1/\xi_k)/\Gamma(3/\xi_k)}\right]^{\xi_k}$ (σ_k^2 is the variance of class k), N_k is the number of pixels in class k and $\Gamma(\cdot)$ is the gamma function.

B. Point Spread Function: Due to the relationship between the blurring matrix $\mathbf{H}$ and the PSF $\mathbf{h}$, which has been illustrated in Appendix A, we estimate the PSF $\mathbf{h}$ instead of the big matrix $\mathbf{H}$. Also, the convolution model is expressed in the Fourier domain (see (4.2)), thus a Gaussian prior is chosen as the prior of $\tilde{\mathbf{h}}$, the Fourier transform of the firs t row of $\mathbf{H}$ [MBBK13]

$$p(\tilde{\mathbf{h}}) = \frac{1}{(2\pi\sigma_h^2)^{N/2}} \exp\left(-\frac{1}{2\sigma_h^2}\|\tilde{\mathbf{h}} - \tilde{\mathbf{h}}_0\|_2^2\right) \tag{4.5}$$

where $\tilde{\mathbf{h}}_0$ is the Fourier transform of the first row of the circulant matrix $\mathbf{H}_0$, which is an initial estimation of the PSF (for instance obtained with the method of [JL94]).

C. Noise variance: In the presence of AWGN, it is typical to assign a conjugate inverse gamma prior to the noise variance [ZBKT16], i.e.,

$$p(\sigma_n^2) = \frac{\nu^\alpha}{\Gamma(\alpha)} \frac{1}{(\sigma_n^2)^{\alpha+1}} \exp\left(-\frac{\nu}{\sigma_n^2}\right) \mathbf{1}_{\mathbb{R}^+}(\sigma_n^2) \tag{4.6}$$

where $\mathbf{1}_A(.)$ is the indicator function on the set A. The two adjustable parameters α, ν make this prior very flexible and appropriate for many applications.

Hyperpriors

The priors introduced above depend on some hyperparameters to be fixed *a priori* or estimated within the algorithm. In this chapter, the hyperparameters to be estimated are the GGD parameters $\boldsymbol{\xi}$, $\boldsymbol{\gamma}$ of the prior distribution for the ultrasound TRF. Note that the label field can be fixed in advance for simulated images or be estimated jointly using the method proposed in Chapter 2. We denote the hyperparameter vector to be estimated as $\boldsymbol{\Phi} = \{\boldsymbol{\xi}, \boldsymbol{\gamma}\}$. The hyperprior of $\boldsymbol{\Phi}$ is defined as $p(\boldsymbol{\Phi}) = p(\boldsymbol{\xi})p(\boldsymbol{\gamma})$ with

$$p(\boldsymbol{\xi}) = \prod_{k=1}^{K} p(\xi_k) = \prod_{k=1}^{K} \frac{1}{3} \mathbf{1}_{[0,3]}(\xi_k) \tag{4.7}$$

$$p(\boldsymbol{\gamma}) = \prod_{k=1}^{K} p(\gamma_k) = \prod_{k=1}^{K} \frac{1}{\gamma_k} \mathbf{1}_{\mathbb{R}+}(\gamma_k). \tag{4.8}$$

We should notice that the choices above cover all the possible values of the shape and scale parameters that one may encounter in practical situations [CPT+10]. Note that the priors/hyperpriors are the same as in Chapter 2 except the Gaussian prior for the PSF.

Joint posterior function

Using Bayes' rule, the joint posterior distribution of our model is proportional to the product of the likelihood and the priors. Precisely, the following result can be obtained

$$\begin{aligned} p(\boldsymbol{\Theta}, \boldsymbol{\Phi}|\mathbf{y}) &\propto p(\mathbf{y}|\boldsymbol{\Theta}, \boldsymbol{\Phi}) p(\boldsymbol{\Theta}, \boldsymbol{\Phi}) \\ &\propto p(\mathbf{y}|\mathbf{x}, \tilde{\mathbf{h}}, \sigma_n^2, \boldsymbol{\xi}, \boldsymbol{\gamma}) p(\mathbf{x}, \tilde{\mathbf{h}}, \sigma_n^2, \boldsymbol{\xi}, \boldsymbol{\gamma}) \\ &\propto p(\mathbf{y}|\mathbf{x}, \tilde{\mathbf{h}}, \sigma_n^2) p(\mathbf{x}|\boldsymbol{\xi}, \boldsymbol{\gamma}) p(\tilde{\mathbf{h}}) \end{aligned} \tag{4.9}$$

where the different probability density functions (pdfs) have been defined in (4.3), (4.4) and (4.5). Closed-form expressions of the Bayesian estimators associated with the posterior (4.9) are difficult to obtain. In such situation, one can use simulation methods which generate samples distributed according to the posterior of interest and use these samples to compute the estimators of the unknown model parameters. The next section studies a hybrid Gibbs sampler to sample (4.9).

4.2.2 Hybrid Gibbs Sampler

The hybrid Gibbs sampler is one of the most popular MCMC methods, which generates samples from a Markov chain whose target distribution is the distribution of interest (here, the distribution (4.9)). More precisely, each step of the sampler consists of generating samples according to the conditional distributions associated with the target distribution. The generated samples, after removing the burn-in period, are averaged to compute the MMSE estimates of the different unknown parameters. The hybrid Gibbs sampler implemented in this section is summarized in Algorithm 5.

Algorithm 5: Hybrid Gibbs Sampler

```
   /* Initialization                                                    */
1  /* Sampling procedure                                               */
2  for i = 1 : N_mc do
3      Sampling x according to (4.10) with an HMC method.
4      Sampling h̃ according to (4.13).
5      Sampling σ_n^2 according to (4.15).
6      Sampling ξ according to (4.16) using a Metropolis Hastings move with a truncated
         Gaussian proposal.
7      Sampling γ according to (4.17).
8  end
```

The associated conditional distributions are detailed as follows.

- Reflectivity image $\mathbf{x}$: The conditional distribution of the US reflectivity image is

$$\begin{aligned} p(\mathbf{x}|\mathbf{y},\sigma_n^2,&\mathbf{H},\mathbf{\Phi}) \propto p(\mathbf{y}|\mathbf{x},\sigma_n^2,\mathbf{H},\mathbf{\Phi})p(\mathbf{x}|\mathbf{\Phi}) \\ &\propto \exp\left(-\frac{1}{2\sigma_n^2}\|\mathbf{y}-\mathbf{H}\mathbf{x}\|_2^2 - \sum_{k=1}^{K}\frac{\|\mathbf{x}_k\|_{\xi^k}^{\xi^k}}{\gamma^k}\right). \end{aligned} \tag{4.10}$$

  Generating samples from (4.10) is complicated due to the high dimensionality of the image $\mathbf{x}$ and to the non-quadratic term $\|\mathbf{x}_k\|_{\xi^k}^{\xi^k}$. In this work, we propose to use a Hamiltonian Monte Carlo (HMC) method for this generation since this method has shown interesting results in the case of non-blind deconvolution in Chapter 2.

- Point Spread Function: We propose to sample $\tilde{\mathbf{h}}$ instead of $\mathbf{H}$ in this section. The likelihood function can be rewritten as follows

$$\begin{aligned} p(\mathbf{y}|\mathbf{x},\sigma_n^2,\mathbf{\Phi},\tilde{\mathbf{h}}) &= \frac{1}{(2\pi\sigma_n^2)^{N/2}}\exp\left(-\frac{1}{2\sigma_n^2}\|\tilde{\mathbf{y}}-\mathbf{\Sigma}_{\boldsymbol{H}}\tilde{\mathbf{x}}\|_2^2\right) \\ &= \frac{1}{(2\pi\sigma_n^2)^{N/2}}\exp\left(-\frac{1}{2\sigma_n^2}\|\tilde{\mathbf{y}}-\mathbf{\Sigma}_{\boldsymbol{X}}\tilde{\mathbf{h}}\|_2^2\right) \end{aligned} \tag{4.11}$$

  where $\mathbf{\Sigma}_{\boldsymbol{H}} = \mathrm{diag}(\tilde{\mathbf{h}})$ and $\mathbf{\Sigma}_{\boldsymbol{X}} = \mathrm{diag}(\tilde{\mathbf{x}})$. Combining with the prior of $\tilde{\mathbf{h}}$, the conditional distribution of $\tilde{\mathbf{h}}$ is given by

$$\begin{aligned} &p(\tilde{\mathbf{h}}|\mathbf{y},\mathbf{x},\sigma_n^2,\mathbf{\Phi}) \propto p(\mathbf{y}|\mathbf{x},\sigma_n^2,\mathbf{\Phi},\tilde{\mathbf{h}})p(\tilde{\mathbf{h}}) \\ &\propto \exp\left(-\frac{1}{2\sigma_n^2}\|\tilde{\mathbf{y}}-\mathbf{\Sigma}_{\boldsymbol{X}}\tilde{\mathbf{h}}\|_2^2\right)\exp\left(-\frac{1}{2\sigma_h^2}\|\tilde{\mathbf{h}}-\tilde{\mathbf{h}}_0\|_2^2\right). \end{aligned} \tag{4.12}$$

  The conditional distribution (4.12) is a multivariate Gaussian distribution

$$\mathcal{N}(\tilde{\mathbf{m}}_{\text{post}},\tilde{\mathbf{R}}_{\text{post}}) \tag{4.13}$$

  with

$$\tilde{\mathbf{R}}_{\text{post}}^{-1} = \frac{\mathbf{I}}{\sigma_h^2} + \frac{|\mathbf{\Sigma}_{\boldsymbol{X}}|^2}{\sigma_n^2},\ \tilde{\mathbf{m}}_{\text{post}} = \tilde{\mathbf{R}}_{\text{post}}\left(\frac{\tilde{\mathbf{h}}_0}{\sigma_h^2} + \frac{\mathbf{\Sigma}_{\boldsymbol{X}}{}^T\tilde{\mathbf{y}}}{\sigma_n^2}\right) \tag{4.14}$$

  where the subscript "post" stands for "posterior". Note that (4.13) is easy to sample and that the circulant matrix $\mathbf{H}$ can be easily obtained from $\tilde{\mathbf{h}}$ by inverse Fourier transform and cyclic shift.

- Noise variance: The conditional distribution of the noise variance σ_n^2 is

$$\begin{aligned} p(\sigma_n^2|\mathbf{y},\mathbf{x},\boldsymbol{\xi},\boldsymbol{\gamma},\mathbf{H}) &\propto p(\mathbf{y}|\mathbf{x},\sigma_n^2,\boldsymbol{\xi},\boldsymbol{\gamma},\mathbf{H})p(\sigma_n^2) \\ &\propto \frac{1}{(\sigma_n^2)^{\frac{N}{2}+\alpha+1}} \exp\left(-\frac{1}{2\sigma_n^2}\|\mathbf{y}-\mathbf{H}\mathbf{x}\|_2^2 - \frac{\nu}{\sigma_n^2}\right). \end{aligned}$$

  It is corresponds to the inverse gamma distribution

$$\mathcal{IG}\left(\alpha + \frac{N}{2}, \nu + \frac{1}{2}\|\mathbf{y}-\mathbf{H}\mathbf{x}\|_2^2\right) \tag{4.15}$$

- Hyperparameters:

  A. Shape parameter $\boldsymbol{\xi}$: Assuming a priori independence between the different shape parameters, the conditional distribution of parameter ξ_k can be obtained as follows

$$\begin{aligned} p(\xi_k|\boldsymbol{\Theta},\boldsymbol{\gamma},\boldsymbol{\xi}_{-k}) &\propto p(\mathbf{y}|\mathbf{x},\sigma_n^2,\mathbf{H},\boldsymbol{\xi},\boldsymbol{\gamma})p(\mathbf{x}_k|\xi_k,\gamma_k)p(\xi_k) \\ &\propto a_k^{N_k} \exp\left(-\frac{\|\mathbf{x}_k\|_{\xi_k}^{\xi_k}}{\gamma_k}\right)\mathbf{1}_{[0,3]}(\xi_k) \end{aligned} \tag{4.16}$$

  where $\boldsymbol{\xi}_{-k} = (\xi_1, ..., \xi_{k-1}, \xi_{k+1}, ..., \xi_K)$ for $k \in \{1, ..., K\}$ and where $\mathbf{x}_k$ contains all the pixels assigned to the kth class. The conditional distribution (4.16) is sampled using a random walk Metropolis Hastings (RWMH) proposal [Has70], which has been detailed in Chapter 2.

  B. Scale parameter $\boldsymbol{\gamma}$: Assuming the different scale parameters are a priori independent, the conditional distributions of the scale parameters of the proposed GGDs can be written

$$\begin{aligned} p(\gamma_k|\boldsymbol{\Theta},\boldsymbol{\xi},\boldsymbol{\gamma}_{-k}) &\propto p(\mathbf{y}|\mathbf{x},\sigma_n^2,\mathbf{H},\boldsymbol{\xi},\boldsymbol{\gamma})p(\mathbf{x}_k|\xi_k,\gamma_k)p(\gamma_k) \\ &\propto \mathcal{IG}\left(\frac{N_k}{\xi_k}, \|\mathbf{x}_k\|_{\xi_k}^{\xi_k}\right) \end{aligned} \tag{4.17}$$

  where $\boldsymbol{\gamma}_{-k} = (\gamma_1, ..., \gamma_{k-1}, \gamma_{k+1}, ..., \gamma_K)$ for $k \in \{1, ..., K\}$. Drawing samples from the inverse gamma distribution (4.17) is straightforward.

4.2.3 Simulation results

In this section, we present results obtained with synthetic and real US images to validate the performance of the proposed algorithm.

Simulated US images

The US images have been generated following the approach described in [NPK+07]. Specifically, the RF image is obtained by 2D convolution of a reflectivity image (of size 50×50) shown in Fig. 4.1(a) and a known PSF (of size 11×11) simulated by Field II (developed by Jensen *et. al.* [Jen96]), highlighted in Fig. 4.2(a). The samples of $\mathbf{x}$ are independent and identically distributed according to GGDs with different parameters inside and outside the disk located in the center of the image ($\mathcal{GGD}(\xi_{\text{in}} = 1.8, \gamma_{\text{in}} = 50)$ and $\mathcal{GGD}(\xi_{\text{out}} = 0.6, \gamma_{\text{out}} = 0.4)$). Moreover, the RF image is contaminated by an AWGN corresponding to a blurred-signal-to-noise-ratio (BSNR) of $40dB$.

Figs. 4.1 show the images estimated by the proposed method and the method of [ZBKT14]. Note that the method of [ZBKT14] requires to estimate the PSF in a preprocessing step using the algorithm in [JL94] and that it was shown to provide better deconvolution results than the EM algorithm in [APMS11]. The objective of this experiment is to evaluate whether the performance of the joint estimation of the image and PSF can be improved or not when compared to the case where the PSF is estimated in a preprocessing step. Visually, one can observe that the reflectivity image estimated with our method is very similar to the true one, both in native and B-mode representations. Quantitative results reported in Table 4.1 show (in terms of ISNR, NRMSE and PSNR) that we obtain a better performance with the proposed method when compared to [ZBKT14]. Note that the higher the values of ISNR, PSNR, the better the performance. Conversely, the lower the NRMSE, the better.

Table 4.1: Performance of reflectivity image estimation.

Methods	$\text{ISNR}_{(\text{dB})}$	$\text{NRMSE}_{(\text{dB})}$	$\text{PSNR}_{(\text{dB})}$
Proposed	8.7597	0.8018	18.5373
[ZBKT14]	4.1089	1.3696	18.0123

The results in Fig. 4.2 allow the performance of the PSF estimation to be appreciated. Figs. 4.2(b), 4.2(c) display the estimated PSFs obtained with the method of [ZBKT14] and our approach. The interest of estimating the PSF jointly with the image is confirmed by the quantitative metrics provided in Table 4.2 comparing the true PSF with its estimates obtained with the proposed method

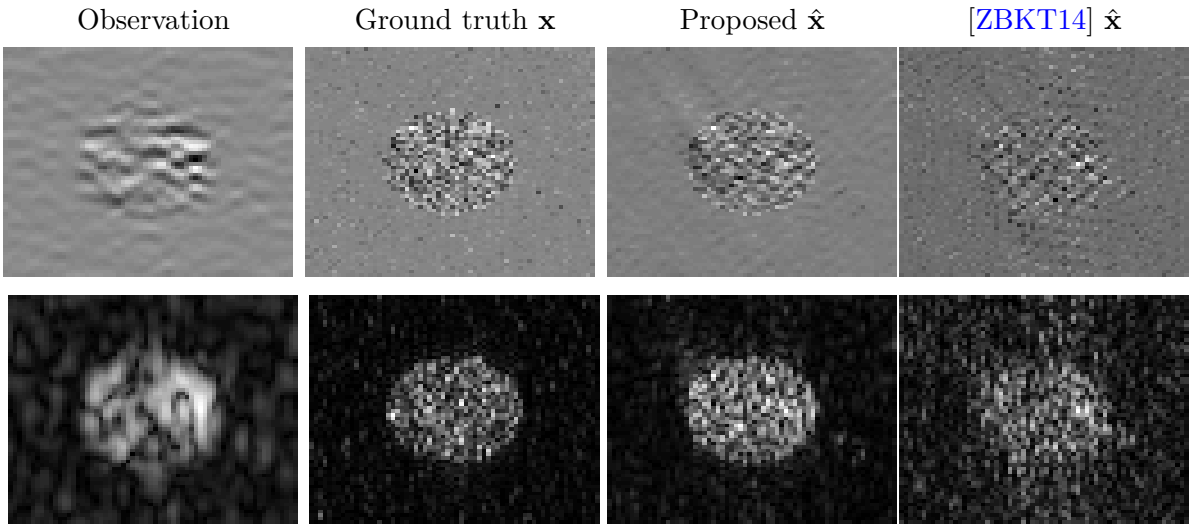

Figure 4.1: Observation, ground truth and estimated US images (top: RF images, bottom: B-mode images).

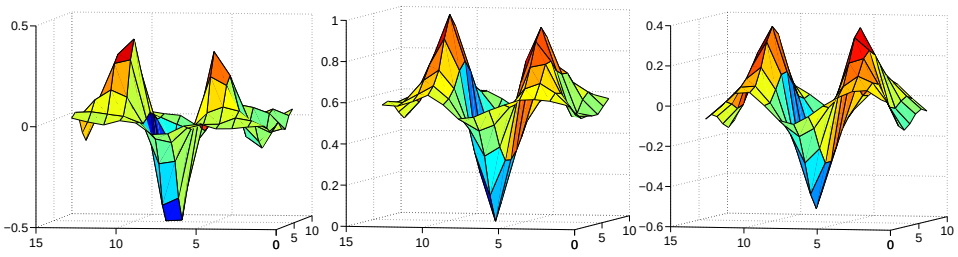

(a) Ground truth $\mathbf{h}$ (b) Proposed $\hat{\mathbf{h}}$ [ZBKT14] $\hat{\mathbf{h}}$

Figure 4.2: Ground truth and estimated PSFs.

Table 4.2: Performance of PSF estimation.

Methods	NRMSE(dB)	PSNR(dB)
Proposed	0.7392	9.2301
[ZBKT14]	0.7805	8.7575

and the method of [ZBKT14].

Real US images

In order to validate the performance of the proposed algorithm, a group of real US images has been considered in this section. Fig. 4.3(a) shows the observation of a healthy skin tissue in B-mode. Figs. 4.3(b), 4.3(c) display the estimated PSFs using the homomorphic technique [JL94, MA01] and the proposed method. Fig. 4.3(d) shows the estimated US TRF using the non-blind deconvolution method of [ZBKT16] and the estimated PSF in Fig. 4.3(b). The restored US TRF using the proposed method is given in Fig. 4.3(e). The visual inspection of the results confirms similar results between the restored US TRF. However, in terms of the resolution gain (RG), the obtained US TRF with the proposed method outperforms the US TRF estimated from the non-blind deconvolution in [ZBKT16]. The estimation of the label field provided by our method is displayed in Fig. 4.3(f), where the skin tissue appears in red.

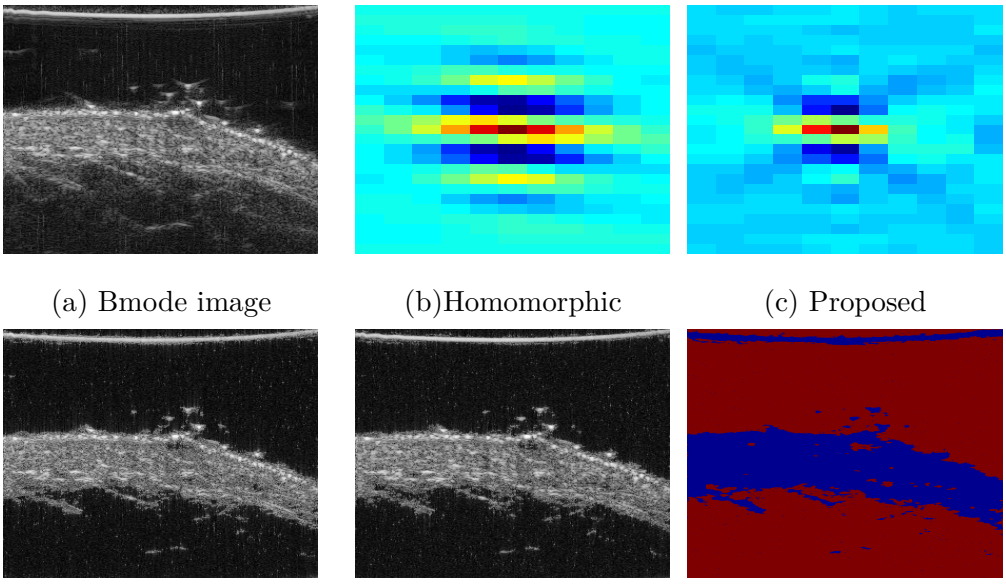

(a) Bmode image (b)Homomorphic (c) Proposed

(d) Non-blind (RF = 2.090) (e) Proposed (RG = 2.325) (f) Estimated labels

Figure 4.3: Blind deconvolution of real US image which corresponds to healthy skin tissue. (a) is the observation; (b),(c) are the estimated PSFs using the homomorphic technique and the proposed method; (d), (e) are the restored US TRF using non-blind deconvlution method and the proposed method; (f) is the estimated labels jointly.

4.3 Blind deconvolution using a parametric model for the PSF

It is interesting to note that the blind deconvolution strategy in last section is time consuming. In order to reduce the computational burden and estimate the PSF and US TRF more efficiently, a parametric model for the PSF is explored in this section. The idea of blind deconvolution using a parametric model for the PSF has been studied in [YZX12b], where a Gaussian function modulated by a sinusoidal function was proposed to model the US PSF.

4.3.1 Parametric model of the PSF

Assuming that the ultrasound impulse response is a modulated band limited signal, we propose the following parametric model for the PSF in an US imaging system

$$\mathbf{h}_{\mathrm{p}}(i,j) \equiv \mathbf{e}(i,j)\cos[\omega_0 \mathbf{t}_{\mathrm{a}}(i) + \phi] \tag{4.18}$$

with

$$\mathbf{e}(i,j) = \mathbf{t}_{\mathrm{a}}^{\zeta}(i)\exp[-\alpha \mathbf{t}_{\mathrm{a}}^2(i) - \beta \mathbf{t}_{\mathrm{l}}^2(j)] \tag{4.19}$$

where the parametric model of PSF "$\mathbf{h}_{\mathrm{p}}$" and the envelope of this model "$\mathbf{e}$" belong to $\mathbb{R}^{q\times r}$, the integers $i \in \{1,\cdots,q\}$, $j \in \{1,\cdots,r\}$ denote the pixel locations, $\omega_0 = 2\pi f_0$ is the central frequency of the transducer (assumed to be known in advance), ϕ is the phase of the system PSF, the parameters α, β, ζ determine the shape of the PSF envelope, the vectors $\mathbf{t}_{\mathrm{a}}$ and $\mathbf{t}_{\mathrm{l}}$ are the temporal axes along the axial and lateral directions (i.e., the vertical and horizontal directions in a 2D US image). Thus, the vectors $\mathbf{t}_{\mathrm{a}} \in \mathbb{R}^{q\times 1}$ and $\mathbf{t}_{\mathrm{l}} \in \mathbb{R}^{1\times r}$ determine the size of the PSF. Fig. 4.4 shows a simulated PSF with the parametric model (4.18).

With the *a priori* knowledge of the size of the PSF[1], there are just a few parameters, i.e., $\phi, \alpha, \beta, \zeta$ to estimate instead of the whole PSF pixels.

- ζ: The value of ζ can be determined by cross validation. More precisely, the value of ζ is fixed to 3 for both simulated and *in vivo* US data in this chapter.

[1]The values of q and r or the size of the PSF are always assumed to be known in advance in the problem of US image deconvolution. Moreover, since the size of the PSF is usually much smaller compared with the size of images (i.e., $q \ll m$, $r \ll n$), zero padding of the PSF is necessary for the convolution in the frequency domain. Without loss of generality, all the PSFs mentioned in this chapter hereinafter have been zero padded for the convolution computation.

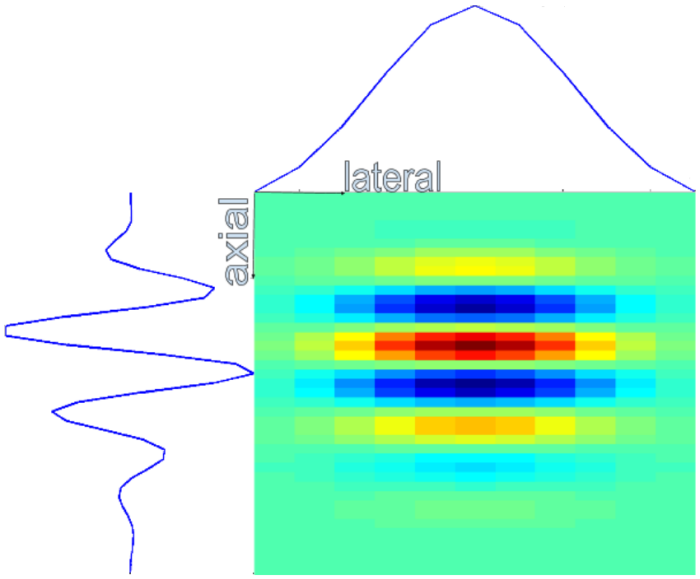

Figure 4.4: Simulated PSF with the proposed parametric model (4.18).

- α and β: We introduce the following vector $\boldsymbol{\theta} = \{\alpha, \beta\}$ as the envelope shape parameters that will be estimated in this section. Since the estimation of the two envelope shape parameters is ill-posed, we propose the following two constraints for them

$$\rho(\alpha) = \imath_{[\alpha_{\min}, \alpha_{\max}]}(\alpha) \tag{4.20}$$

$$\varrho(\beta) = \imath_{[\beta_{\min}, \beta_{\max}]}(\beta) \tag{4.21}$$

  where $\rho(\alpha)$ and $\varrho(\beta)$ are two indicator functions on the sets $[\alpha_{\min}, \alpha_{\max}]$ and $[\beta_{\min}, \beta_{\max}]$.

- ϕ: The estimation of phase term ϕ can be complicated since the phase is wrapped into $[-\pi, \pi]$ [MA01]. In this section, we estimate the phase term as the traditional cepstrum-based method, i.e., the minimum phase assumption [JL94]. It is also interesting to note that it is possible to avoid the estimation of ϕ by dealing with demodulated signals following [YZX12b].

4.3.2 Optimization Problem Formulation

Taking into account the parametric model for the PSF (4.18), we formulate the US image blind deconvolution problem as follows

$$\begin{aligned} \min_{\mathbf{x},\boldsymbol{\theta}} \quad & \Psi(\mathbf{x},\mathbf{h}) + \tau\varphi(\mathbf{x}) + \rho(\alpha) + \varrho(\beta) \\ \text{subject to} \quad & \mathbf{h} = \mathbf{h}_{\mathrm{p}} \end{aligned} \tag{4.22}$$

where $\Psi(\mathbf{x},\mathbf{h})$ is the data fidelity term, $\varphi(\mathbf{x})$ is the regularization term for the TRF and τ is the corresponding regularization parameter which weight the importance between the data fidelity term and the regularization term. Under the assumption of additive white Gaussian noise (AWGN), we have

$$\Psi(\mathbf{x},\mathbf{h}) = \frac{1}{2}\|\mathbf{y} - \mathbf{H}\mathbf{x}\|^2. \tag{4.23}$$

In order to calculate the convolution $\mathbf{H}\mathbf{x}$, we hereinafter recall the basic assumption on the PSF used in this section, which has also been considered in Section 3.2 and the literature therein.

Assumption 1. *The blurring matrix* $\mathbf{H}$ *represents a cyclic convolution, i.e.,* $\mathbf{H}$ *is a block circulant matrix with circulant blocks (BCCB).*

Using the cyclic convolution assumption, the blurring matrix and its conjugate transpose can be decomposed as

$$\mathbf{H} = \mathbf{F}^H\boldsymbol{\Lambda}\mathbf{F} \tag{4.24}$$

$$\mathbf{H}^H = \mathbf{F}^H\boldsymbol{\Lambda}^H\mathbf{F} \tag{4.25}$$

where $\boldsymbol{\Lambda} = \mathrm{diag}\{\mathbf{F}\mathbf{h}\} \in \mathbb{C}^{N\times N}$ is a diagonal matrix, whose diagonal elements are the eigenvalues of the matrix $\mathbf{H}$ or the Fourier coefficients of the first column of the blurring matrix $\mathbf{H}$, i.e., $\mathbf{h}$. Using this assumption, the linear operation $\mathbf{H}\mathbf{x}$ can also be rewritten as below

$$\begin{aligned} \mathbf{H}\mathbf{x} &= \mathbf{F}^H\boldsymbol{\Lambda}\mathbf{F}\mathbf{x} \\ &= \mathbf{F}^H\mathrm{diag}\{\mathbf{F}\mathbf{h}\}\mathbf{F}\mathbf{x} \\ &= \mathbf{F}^H\mathrm{diag}\{\mathbf{F}\mathbf{x}\}\mathbf{F}\mathbf{h} \\ &= \mathbf{X}\mathbf{h} \end{aligned} \tag{4.26}$$

where $\mathbf{X} = \mathbf{F}^H \text{diag}\{\mathbf{F}\mathbf{x}\}\mathbf{F}$ is a block circulant matrix with circulant blocks. Note that (4.26) will be used for the estimation of the PSF.

4.3.3 BCD-based algorithms

In order to solve the problem (4.22), we propose a proximal alternating minimization approach, which is within the block-coordinate descent (BCD) framework. Algorithm 6 summarizes the proposed BCD strategy, where each sub-step is addressed using proximal forward-backward (PFB) algorithm. Note that the convergence analysis of the proximal alternating linearized minimization (PALM) algorithm has been studied in [BST14].

Algorithm 6: Overall Algorithm

Input: Observation $\mathbf{y}$, Initial estimation $\mathbf{h}_0$, τ, Parameters of PSF model α_0, β_0

// Update $\mathbf{x}$ *with a known PSF*

1 $\hat{\mathbf{x}} \in \arg\min_{\mathbf{x}} \Psi(\mathbf{x}, \mathbf{h}) + \tau\varphi(\mathbf{x})$;

// Update $\mathbf{h}$ *by estimating* α, β *with a known TRF*

2 $\hat{\alpha}, \hat{\beta} \in \arg\min_{\alpha,\beta} \Psi(\mathbf{x}, \mathbf{h}) + \rho(\alpha) + \varrho(\beta)$;

3 $\hat{\mathbf{h}} = \mathbf{h}_{\text{p}}(\hat{\alpha}, \hat{\beta})$;

Output: $\hat{\mathbf{x}}$, $\hat{\mathbf{h}}$

Estimation of the TRF x

Considering AWGN, the sub-optimization problem to estimate the TRF $\mathbf{x}$ can be formulated as below

$$\hat{\mathbf{x}} \in \arg\min_{\mathbf{x}} \Psi(\mathbf{x}, \mathbf{h}) + \tau\varphi(\mathbf{x}). \tag{4.27}$$

The problem (4.27) is a typical non-blind deconvolution problem. In this section, a GGD is considered as a prior for $\mathbf{x}$ as explained in the next paragraph.

ℓ_p-norm regularizer Given a generalized Gaussian prior for the ultrasound TRF and AWGN, the problem (4.27) can be written as below

$$\hat{\mathbf{x}} \in \arg\min_{\mathbf{x}} \frac{1}{2}\|\mathbf{y} - \mathbf{H}\mathbf{x}\|^2 + \tau\|\mathbf{x}\|_p^p \tag{4.28}$$

where $\|\mathbf{x}\|_p = \sqrt[p]{|x_1|^p + \cdots + |x_N|^p}$ and $0 < p \leq 2$. The PFB method implemented to solve (4.27) is defined by the following recursions

$$\begin{aligned} &\text{For } j = 0, 1, \ldots, J-1 \\ &\left\lfloor \begin{aligned} &\bar{\mathbf{x}}^j = \mathbf{x}^j - \gamma_{\mathbf{x}} A_{\mathbf{x}}^{-1} \nabla_{\mathbf{x}} \Psi(\mathbf{x}^j, \mathbf{h}), \\ &\mathbf{x}^{j+1} = \text{prox}_{\gamma_{\mathbf{x}}^{-1} A_{\mathbf{x}}, \varphi}(\bar{\mathbf{x}}^j) \end{aligned} \right. \end{aligned} \tag{4.29}$$

where $A_{\mathbf{x}} = \|\mathbf{H}^H \mathbf{H}\|$, $\text{prox}_{\gamma_{\mathbf{x}}^{-1}, \varphi} : \mathbb{R}^n \to \mathbb{R}^n$ is a component-wise application of the proximity operator associated with the function φ, defined as

$$\text{prox}_{\gamma_{\mathbf{x}}^{-1}, \varphi}(\bar{x}) = \arg\min_x \frac{1}{2\gamma_{\mathbf{x}}} |\bar{x} - x|^2 + \tau \varphi(x) \tag{4.30}$$

where $\|\cdot\|$ is the usual Euclidean norm, x and $\bar{x}$ represent any component of the vectors $\mathbf{x}$ and $\bar{\mathbf{x}}$ respectively.

Theorem 2. *The optimization problem*

$$\arg\min_x \frac{1}{2\gamma} |\bar{x} - x|^2 + \tau |x|^p, \tag{4.31}$$

has an analytical solution that can be computed as follows

$$prox_{\gamma^{-1}, |\cdot|^p}(\bar{x}) = \begin{cases} x_* \text{sgn}(\bar{\text{x}}) \max(0, |\bar{\text{x}}| - \chi) & 0 < p \leq 1 \\ x_* \text{sgn}(\bar{x}) & 1 < p \leq 2 \end{cases} \tag{4.32}$$

with a thresholding χ given by

$$\chi = [2\lambda(1-p)]^{\frac{1}{2-p}} + \lambda p [2\lambda(1-p)]^{\frac{p-1}{2-p}} \tag{4.33}$$

where $\lambda = \tau\gamma$, x_* is the positive root of the equation

$$x + \lambda p x^{p-1} = |\bar{x}|. \tag{4.34}$$

Proof. See Appendix D. □

Fig. 4.5 shows the graph of the proximity operator when $0 < p \leq 2$. Note that (4.32) is also valid when $p > 2$ even if we are just interested in $p \in (0, 2]$ in this chapter. Note that the soft (hard)

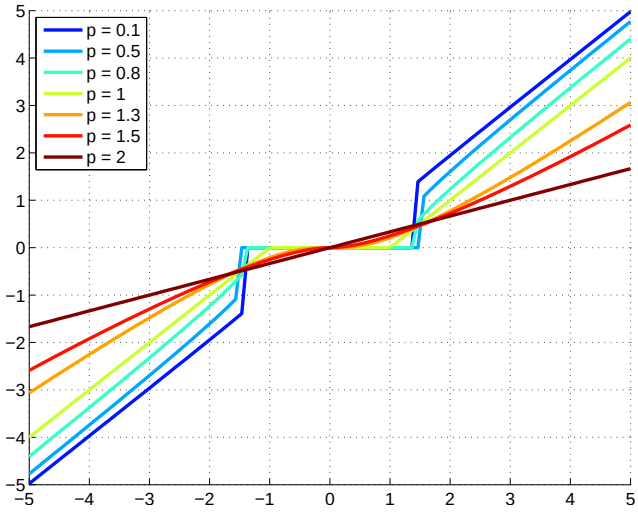

Figure 4.5: Graph of proximity operator of $|\cdot|^p$ $(0 < p \leq 2)$.

thresholding can be recovered as the special cases of (4.32) when $p \to 1$ $(p \to 0)$. We recall that the soft-thresholding operator is defined by

$$\text{prox}_{\gamma^{-1},|\cdot|}(\bar{x}) = \max(0, |\bar{x}| - \chi)\text{sgn}(\bar{x}) \tag{4.35}$$

where $\chi = \tau\gamma$. We should also note that when $p \geq 1$, the problem (4.28) is convex and can be solved by a variety of existing algorithms, including the ADMM (alternating direction method of multipliers) [BPC+11a], ISTA (iterative shrinkage-thresholding algorithm), FISTA (fast ISTA) [BT09], TwIST (two step ISTA)[BDF07] and so on.

Estimation of the PSF h

As discussed above, we can estimate the PSF by calculating the MAP estimators of the PSF envelope parameters α and β by solving the following sub-optimization problem

$$\begin{aligned} \hat{\alpha}, \hat{\beta} &\in \arg\min_{\alpha,\beta} \Psi(\mathbf{x}, \mathbf{h}) + \rho(\alpha) + \varrho(\beta) \\ &\in \arg\min_{\alpha,\beta} \|\mathbf{X}\mathbf{h} - \mathbf{y}\|^2 + \rho(\alpha) + \varrho(\beta) \end{aligned} \tag{4.36}$$

It is obviously not possible to find a closed-form solution for (4.36). Thus, an iterative method should be considered. More specifically, we propose a PFB algorithm (4.37) to estimate α, β.

$$\begin{aligned}
&\text{For } i = 0, 1, \ldots, I-1 \\
&\left\lfloor \begin{aligned}
&\bar{\alpha}^i = \alpha^i - \gamma_\alpha A_\alpha^{-1}(\mathbf{x}, \mathbf{h}^i) \nabla_\alpha \Psi(\mathbf{x}, \mathbf{h}^i), \\
&\alpha^{i+1} = \operatorname{prox}_{\gamma_\alpha^{-1} A_\alpha(\mathbf{x}, \mathbf{h}^i), \rho}(\bar{\alpha}^i), \\
&\bar{\beta}^i = \beta^i - \gamma_\beta A_\beta^{-1}(\mathbf{x}, \mathbf{h}^i) \nabla_\beta \Psi(\mathbf{x}, \mathbf{h}^i), \\
&\beta^{i+1} = \operatorname{prox}_{\gamma_\beta^{-1} A_\beta(\mathbf{x}, \mathbf{h}^i), \varrho}(\bar{\beta}^i),
\end{aligned} \right.
\end{aligned} \tag{4.37}$$

where $A_\alpha(\mathbf{x}, \mathbf{h}^i) = A_\beta(\mathbf{x}, \mathbf{h}^i) = L(\mathbf{x})\mathbf{I}_N$ with $L(\mathbf{x}) = \|\mathbf{X}^H\mathbf{X}\|_2$ and $\mathbf{I}_N \in \mathbb{R}^N$ is an identity matrix. Since the functions $\rho(\alpha)$ and $\varrho(\beta)$ are two indicator functions on convex sets, the proximity operators reduce to the Euclidean projection onto the corresponding convex sets. Define $\nabla_\alpha \Psi(\mathbf{x}, \mathbf{h}^i)$ and $\nabla_\beta \Psi(\mathbf{x}, \mathbf{h}^i)$ as the gradient of the function Ψ with respect to α and β, which can be calculated as below

$$\begin{aligned}
\nabla_\alpha \Psi(\mathbf{x}, \mathbf{h}^i) &= \left\langle \frac{\partial \Psi}{\partial \mathbf{h}^i}, \frac{\partial \mathbf{h}^i}{\partial \alpha} \right\rangle \\
&= \left\langle \mathbf{X}^H(\mathbf{X}\mathbf{h}^i - \mathbf{y}), -\mathbf{c} \odot \mathbf{t}_{\mathrm{a}}^2 \odot \exp(-\alpha \mathbf{t}_{\mathrm{a}}^2) \exp(-\beta \mathbf{t}_{\mathrm{l}}^2) \right\rangle \qquad (4.38) \\
\nabla_\beta \Psi(\mathbf{x}, \mathbf{h}^i) &= \left\langle \frac{\partial \Psi}{\partial \mathbf{h}^i}, \frac{\partial \mathbf{h}^i}{\partial \beta} \right\rangle \\
&= \left\langle \mathbf{X}^H(\mathbf{X}\mathbf{h}^i - \mathbf{y}), -\mathbf{c} \odot \exp(-\alpha \mathbf{t}_{\mathrm{a}}^2)(\mathbf{t}_{\mathrm{l}}^2 \odot \exp(-\beta \mathbf{t}_{\mathrm{l}}^2)) \right\rangle \qquad (4.39)
\end{aligned}$$

where "$\odot$" is the Hadamard product, the vector $\mathbf{c} = (\mathbf{c}(1), \cdots, \mathbf{c}(N))^T$ with its element $\mathbf{c}(n) = \mathbf{t}_{\mathrm{a}}^{\zeta}(n) \cos(\omega_0 \mathbf{t}_{\mathrm{a}}(n) + \varphi)$ $(n = 1, \cdots, N)$ and $\langle \cdot, \cdot \rangle$ represents the inner product between two vectors.

Alternating Optimization Approach

The pseudo code of the algorithm that we propose for estimating the parameters of the PSF model and the ultrasound TRF jointly is given below. Note that the PALM algorithm in [BST14] can be recovered as a special case of the proposed algorithm when $J = I = 1$.

Algorithm 7: Proposed Algorithm

Input: Observation $\mathbf{y}$, Initial estimation $\mathbf{h}_0$, τ, Parameters of PSF model α_0, β_0

for k = *0,1, ...* **do**
  $\mathbf{x}^{k,0} = \mathbf{x}^k$, $\mathbf{h}^{k,0} = \mathbf{h}^k$;
  // Update $\mathbf{x}$
  for j = *0,1, ... ,J* **do**
    $\bar{\mathbf{x}}^{k,j} = \mathbf{x}^{k,j} - \gamma_{\mathbf{x}} A_{\mathbf{x}}^{-1} \nabla_{\mathbf{x}} \Psi(\mathbf{x}^{k,j}, \mathbf{h}^k)$;
    $\mathbf{x}^{k,j+1} = \text{prox}_{\gamma_{\mathbf{x}}^{-1} A_{\mathbf{x}}, \varphi}(\bar{\mathbf{x}}^{k,j})$;
  end
  // Update $\mathbf{h}$
  $\mathbf{x}^{k+1} = \mathbf{x}^{k,J}$;
  for i = *0,1, ... ,I* **do**
    $\bar{\alpha}^{k,i} = \alpha^{k,i} - \gamma_\alpha A_\alpha^{-1} \nabla_\alpha \Psi(\mathbf{x}^{k+1}, \mathbf{h}^{k,i})$;
    $\alpha^{k,i+1} = \text{prox}_{\gamma_\alpha^{-1} A_\alpha, \rho}(\bar{\alpha}^{k,i})$;
    $\bar{\beta}^{k,i} = \beta^{k,i} - \gamma_\beta A_\beta^{-1} \nabla_\beta \Psi(\mathbf{x}^{k+1}, \mathbf{h}^{k,i})$;
    $\beta^{k,i+1} = \text{prox}_{\gamma_\beta^{-1} A_\beta, \rho}(\bar{\beta}^{k,i})$
  end
  $\alpha^{k+1} = \alpha^{k,I}$, $\beta^{k+1} = \beta^{k,I}$;
  $\mathbf{h}^{k+1} = \mathbf{h}_{\text{p}}(\alpha^{k+1}, \beta^{k+1})$;
  until meet the stopping criterion
end

Output: $\hat{\mathbf{x}} = \mathbf{x}^{k+1}$, $\hat{\mathbf{h}} = \mathbf{h}^{k+1}$

4.3.4 Simulation results

In order to study the performance of the proposed algorithm, experiments have been conducted on simulated and *in vivo* ultrasound images. Moreover, a comparison with a non-blind deconvolution algorithm, where the PSF is estimated in a pre-processing step using the cepstrum-based algorithm [MA03, JL94] has been conducted. For simulated US images, the performance of different algorithms can be evaluated by the NRMSE. However, the ground truth for the ultrasound TRF and PSF are not available for real US images. Thus, the resolution gain (RG) and visually inspection have been

used to evaluate the performance of TRF estimation quantitatively for the real images.

Simulated US images

Simulated ultrasound image $\mathbf{x}$ of size 275×75 has been generated according to generalized Gaussian distribution, as shown in Fig. 4.6(a). More details about this generation can be found in Chapter 2. The observed image shown in Fig. 4.6(e) has been blurred by a simulated PSF (displayed in Fig. 4.6(b)) using the parametric model (4.18) and contaminated by an additive white Gaussian noise with BSNR= 30 dB. Figs. 4.6(c), 4.6(d) display the estimated PSFs using the cepstrum-based method described in Chapter 1 and the proposed method. Figs. 4.6(f)-4.6(h) show the restored ultrasound TRFs using the true PSF, the estimated PSFs obtained with the cepstrum-based method and the proposed method respectively. Moreover, the prior used for the TRF is an ℓ_p-norm with $p = 0.5$ for all experiments related to simulated images. The TRFs estimated using the true PSF and the proposed method are visually very similar. The PSF obtained with the proposed method is also closer to the true PSF than the estimated PSF using the cepstrum-based method. The quantitative results displayed in Table 4.3 confirm the visual impression in terms of NRMSE. To conclude, the proposed blind deconvolution algorithm seems to provide better performance than the one obtained with the non-blind deconvolution algorithm using a PSF estimated with cepstrum-based method.

Table 4.3: Simulated US images: Performance of blind deconvolution using parametric PSF model.

		NRMSE	
Method	Prior	$\mathbf{x}$	$\mathbf{h}$
Non blind with (f)	$\ell_{0.5}$	0.97	0
Non blind with (g)	$\ell_{0.5}$	1.44	1.70
Proposed	$\ell_{0.5}$	**1.09**	**0.04**

Real US images

The proposed blind deconvolution algorithm has also been tested on real US images using an ℓ_p-norm regularization. In this experiment, an ultrasound image representing a mouse kidney has been

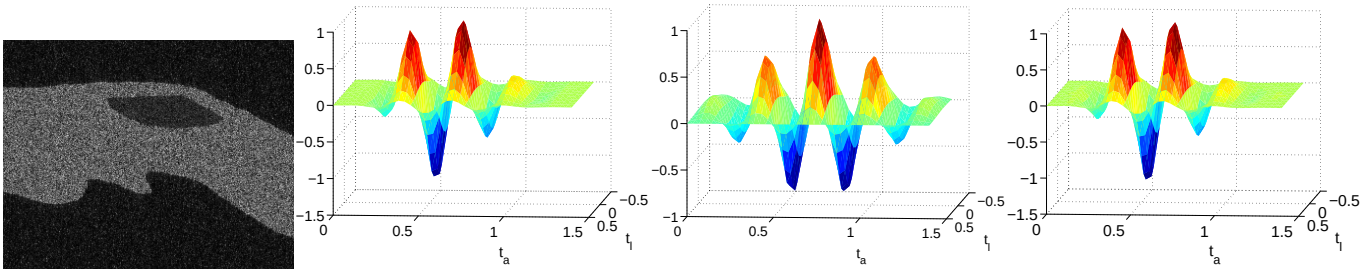

(a) True TRF (b) True PSF (c) Cepstrum (d) Proposed

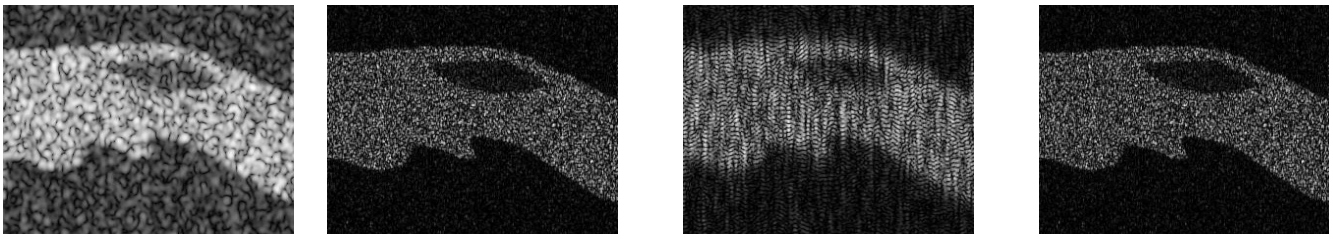

(e) Observation (f) Non blind with (b) (g) Non blind with (c) (h) Proposed

Figure 4.6: Blind deconvolution of simulated US images using a parametric model for the PSF.

acquired with a probe with 25 MHz central frequency, as shown in Fig. 4.7(a). The value of p has been fixed to 0.5, 1, 1.5 and 2 for the experiments of *in vivo* US images. The restored ultrasound TRFs shown in Figs. 4.7(b)-(i) are obtained with the non-blind (cepstrum-based method) and the proposed algorithms. In Figs. 4.7, the estimated TRFs using the proposed algorithm and the non-blind deconvolution method have clearer boundaries than the observed image in Fig. 4.7(a). Moreover, the smoothness of the restored images is proportional the the value of p according to the results presented in Fig. 4.7. The RG of the restored image is inversely proportional to the value of p.

4.4 Conclusion

This chapter studied two strategies for the blind deconvolution of medical ultrasound images. In the first strategy, a hierarchical Bayesian model for the joint estimation of an ultrasound image and the system PSF was proposed. In order to solve this ill-posed problem, generalized Gaussian priors were

assigned to the reflectivities of homogeneous regions in the image and a Gaussian prior was chosen for the PSF. The results obtained on simulated US data clearly highlight the interest of updating the PSF during the deconvolution process. In the second strategy, a parametric model was proposed for the system PSF such that a few parameters related with the model were estimated instead of the whole PSF, which reduced the computational time significantly. Moreover, an alternating optimization method based on the forward-backward splitting technique was implemented to address the formulated problem, where the proximity operator of the ℓ_p-norm function was studied. Note that the second strategy is much more efficiency in terms of the computational time compared with the first strategy. A more detailed comparison with be conducted in the future.

(a) Observation (b) Non-blind ($\ell_{0.5}$) (c) Proposed ($\ell_{0.5}$)

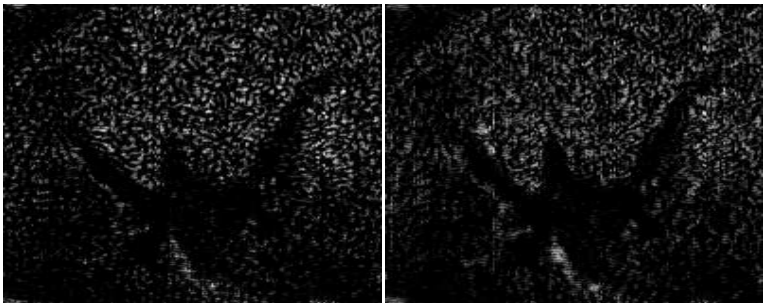

(d) Non-blind (ℓ_1) (e) Proposed (ℓ_1)

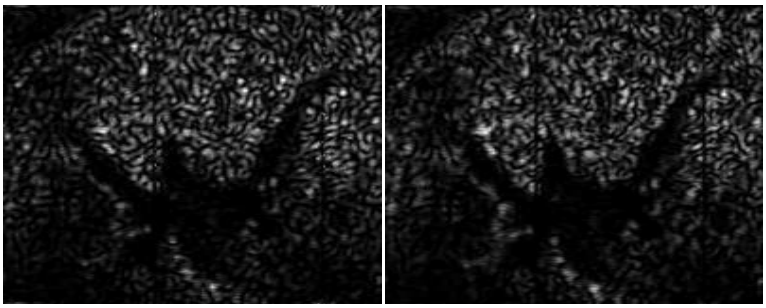

(f) Non-blind ($\ell_{1.5}$) (g) Proposed ($\ell_{1.5}$)

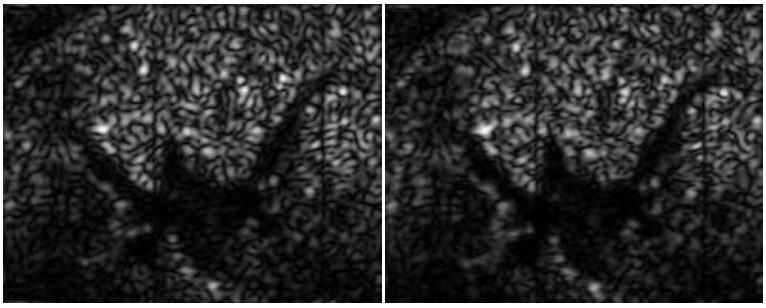

(h) Non-blind (ℓ_2) (i) Proposed (ℓ_2)

Figure 4.7: Blind deconvolution of real US images using a parametric model for the PSF.

Conclusions and perspectives

Conclusions

The objective of this thesis was to improve the medical ultrasound image quality by post-processing techniques. The main difficulty of medical ultrasound image restoration is its granular appearance due to speckle noise. In this thesis, we exploited the statistical properties of speckle to build new image restoration techniques. More precisely, the statistical characteristics of ultrasound radio-frequency images were modelled by generalized Gaussian distributions. Our main contributions related to the restoration techniques are summarized below Based on the statistical analysis of ultrasound radio-frequency images, several post-processing techniques are proposed.

The first work studied in Chapter 2 proposed a hierarchical Bayesian model for joint deconvolution and segmentation of medical ultrasound images. According to the statistical analysis of medical ultrasound radio-frequency images, a generalized Gaussian distribution was proposed as prior for the tissue reflectivity function/image to be estimated. Also, a hidden label field within the spatial information of the tissue reflectivity function was introduced for the segmentation purpose. The proposed priors were combined with the likelihood to provide a joint posterior distribution. This posterior was too complicated to compute analytical expression or the Bayesian estimators. Thus, a Gibbs sampler was investigated. Also, a Hamiltonian Monte Carlo algorithm was embedded into the Gibbs sampler to sample the high dimension tissue reflectivity function efficiently. Compared with the existing techniques for ultrasound image deconvolution, the proposed Bayesian framework joint the deconvolution and segmentation problems in a elegant way. Moreover, simulation results conducted both on simulated images and real ultrasound images showed that the deconvolution performance

benefited from the segmentation information. In this sense, the proposed method is competitive with the state-of-the-art techniques for image deconvolution.

Chapter 3 proposed a novel method for single image super-resolution. This method can be implemented not only for medical ultrasound images but also for piece-wise constant/natural images. Single image super-resolution aims at estimating a high resolution image from a blurred, down-sampled and noisy observation. Compared with the existing methods for single image super-resolution, e.g., first order gradient or splitting based algorithm, the proposed method was able to give an analytical solution for the $\ell_2 - \ell_2$ problems/Tikhonov regularized quadratic problems. Moreover, in order to handle more generic image priors, the analytical solution was embedded into an traditional alternating direction methods of multipliers (ADMM) framework. Numerical experiments showed that the novel method using the proposed analytical solution for single image super-resolution problems can increase the computational efficiency significantly than the existing methods.

Chapter 4 studied blind deconvolution of ultrasound images, which is an additionally ill-posed problem. Thus, two strategies were investigated. First, a hierarchical Bayesian framework was firstly proposed, where a Gaussian prior was introduced for the system point spread function. Due to the intractability of the joint posterior distribution, a Markov chain Monte Carlo method was explored. Simulations conducted showed that the proposed method was competitive with the existing non-blind ultrasound image deconvolution method. In order to reduce the computational burden, a parametric model for the PSF is explored in a second step. A few parameters of the model were estimated instead of the whole pixels of blurring kernel. Moreover, an alternating optimization method was proposed for the formulated problem. Compared with the first strategy, the computational complexity was reduced significantly. The experiments demonstrated the performance and efficiency of the proposed method.

Future work

The open issues and perspectives resulting from this thesis are listed in what follows.

Regularizations: It is well known that the inverse problems are ill-posed/ill-conditioned. Thus, various priors/regularizations have been considered in our works and the relative references to address

this problem. However, the regularization parameters are fixed in the optimization methods of this thesis. It is interesting how to tune these parameters adaptively.

Ultrasound image segmentation: Up to now, the segmentation of medical ultrasound images remains under exploration widely. Even through a variety of algorithms have been developed for medical ultrasound image segmentation, it is still an interesting track [BHA+14]. For instance, ultrasound image segmentation combined with machine learning techniques, or image segmentation using more precise anatomical information of the object of interest, e.g., atlas-based segmentation methods.

Multi-frame image super-resolution: In Chapter 3, a method for single image super-resolution has been explored. However, it is very interesting to deal with multi-frame image super-resolution since it is reasonable to assume that more information in the observations can help in restoration of a high resolution images. Thus, how to address multi-frame image super-resolution with the proposed method is an interesting track.

3D image analysis: All the methods proposed methods in this thesis aim at 2D images. How to extend the proposed methods to 3D images or develop new techniques especially for 3D images are of interest.

Other medical applications: Other medical image applications include not only ultrasound image analysis, e.g., motion estimation, processing specific data (brain, cardiac disease, breast, etc.) but also other medical image modalities, e.g., MRI, CT.

Appendices

Appendix A

Computation of blurring operator

Consider the following linear image formation model

$$\boldsymbol{y} = \boldsymbol{h} \circledast \boldsymbol{x} \tag{A.1}$$

where $\boldsymbol{x} \in \mathbb{R}^{m \times n}$ is the ground truth/image to be estimated, $\boldsymbol{y} \in \mathbb{R}^{m \times n}$ is the observed image and $\boldsymbol{h} \in \mathbb{R}^{p \times q}$ is a spatially invariant blurring operator. A more widely used representation of the image formation model (A.1) is given by the matrix-vector formation as below

$$\mathbf{y} = \mathbf{H}\mathbf{x} \tag{A.2}$$

where $\mathbf{x}$ and $\mathbf{y}$ ($\in \mathbb{R}^{N \times 1}$, $N = m \times n$) are column stacked vectors obtained by lexicographical ordering of $\boldsymbol{x}$ and $\boldsymbol{y}$. The blurring matrix $\mathbf{H}$ is associated with the blurring operator $\boldsymbol{h}$. As stated in Chapter 1, the blurring matrix $\mathbf{H}$ is a block circulant matrix with circulant blocks (BCCB) when cyclic boundary is considered [Gar06].

A.1 Block circulant matrix with circulant blocks

A matrix is called BCCB if each row of blocks is a periodic shift of its previous row of blocks and every block is a circulant matrix, see e.g., Fig. A.1.

Consider an example where the images $\boldsymbol{x}$, $\mathbf{y} \in \mathbb{R}^{5 \times 5}$ and the blurring operator $\boldsymbol{h} \in \mathbb{R}^{3 \times 3}$ are

$$\left[\begin{array}{ccc|ccc|ccc}
p_{22} & p_{12} & p_{32} & p_{21} & p_{11} & p_{31} & p_{23} & p_{13} & p_{33} \\
p_{32} & p_{22} & p_{12} & p_{31} & p_{21} & p_{11} & p_{33} & p_{23} & p_{13} \\
p_{12} & p_{32} & p_{22} & p_{11} & p_{31} & p_{21} & p_{13} & p_{33} & p_{23} \\
\hline
p_{23} & p_{13} & p_{33} & p_{22} & p_{12} & p_{32} & p_{21} & p_{11} & p_{31} \\
p_{33} & p_{23} & p_{13} & p_{32} & p_{22} & p_{12} & p_{31} & p_{21} & p_{11} \\
p_{13} & p_{33} & p_{23} & p_{12} & p_{32} & p_{22} & p_{11} & p_{31} & p_{21} \\
\hline
p_{21} & p_{11} & p_{31} & p_{23} & p_{13} & p_{33} & p_{22} & p_{12} & p_{32} \\
p_{31} & p_{21} & p_{11} & p_{33} & p_{23} & p_{13} & p_{32} & p_{22} & p_{12} \\
p_{11} & p_{31} & p_{21} & p_{13} & p_{33} & p_{23} & p_{12} & p_{32} & p_{22}
\end{array}\right]$$

Figure A.1: A BCCB matrix of size 9×9.

showed in (A.3).

$$\boldsymbol{x} = \begin{bmatrix} x_{11} & x_{12} & x_{13} & x_{14} & x_{15} \\ x_{21} & x_{22} & x_{23} & x_{24} & x_{25} \\ x_{31} & x_{32} & x_{33} & x_{34} & x_{35} \\ x_{41} & x_{42} & x_{43} & x_{44} & x_{45} \\ x_{51} & x_{52} & x_{53} & x_{54} & x_{55} \end{bmatrix}, \quad \boldsymbol{h} = \begin{bmatrix} h_{11} & h_{12} & h_{13} \\ h_{21} & h_{22} & h_{23} \\ h_{31} & h_{32} & h_{33} \end{bmatrix} \quad \text{and} \quad \boldsymbol{y} = \begin{bmatrix} y_{11} & y_{12} & y_{13} & y_{14} & y_{15} \\ y_{21} & y_{22} & y_{23} & y_{24} & y_{25} \\ y_{31} & y_{32} & y_{33} & y_{34} & y_{35} \\ y_{41} & y_{42} & y_{43} & y_{44} & y_{45} \\ y_{51} & y_{52} & y_{53} & y_{54} & y_{55} \end{bmatrix}. \tag{A.3}$$

In order to use the forward model (A.1) to calculate the observation $\boldsymbol{y}$, the blurring operator is rotated and its center is placed over each element in matrix $\boldsymbol{x}$. Then an element by element multiplication and summation are performed.

$$\left[\begin{array}{c|cccccc}
x_{55}h_{33} & x_{51}h_{32} & x_{52}h_{31} & x_{53} & x_{54} & x_{55} & x_{51} \\
\hline
x_{15}h_{23} & x_{11}h_{22} & x_{12}h_{21} & x_{13} & x_{14} & x_{15} & x_{11} \\
x_{25}h_{13} & x_{21}h_{12} & x_{22}h_{11} & x_{23} & x_{24} & x_{25} & x_{21} \\
x_{35} & x_{31} & x_{32} & x_{33} & x_{34} & x_{35} & x_{31} \\
x_{45} & x_{41} & x_{42} & x_{43} & x_{44} & x_{45} & x_{41} \\
x_{55} & x_{51} & x_{52} & x_{53} & x_{54} & x_{55} & x_{51} \\
\hline
x_{15} & x_{11} & x_{12} & x_{13} & x_{14} & x_{15} & x_{11}
\end{array}\right] \tag{A.4}$$

The BCCB matrix $\in \mathbb{R}^{25\times 25}$ in the linear model for image deblurring is then given by

$$\mathbf{H} = \begin{bmatrix} \mathbb{H}_2 & \mathbb{H}_1 & \bigcirc & \bigcirc & \mathbb{H}_3 \\ \mathbb{H}_3 & \mathbb{H}_2 & \mathbb{H}_1 & \bigcirc & \bigcirc \\ \bigcirc & \mathbb{H}_3 & \mathbb{H}_2 & \mathbb{H}_1 & \bigcirc \\ \bigcirc & \bigcirc & \mathbb{H}_3 & \mathbb{H}_2 & \mathbb{H}_1 \\ \mathbb{H}_1 & \bigcirc & \bigcirc & \mathbb{H}_3 & \mathbb{H}_2 \end{bmatrix} \tag{A.5}$$

where $\bigcirc \in \mathbb{R}^{5\times 5}$ is a matrix with all entries equal to 0 and the block $\mathbb{H}_k \in \mathbb{R}^{5\times 5}$ is defined as

$$\mathbb{H}_k = \begin{bmatrix} h_{2k} & h_{1k} & 0 & 0 & h_{3k} \\ h_{3k} & h_{2k} & h_{1k} & 0 & 0 \\ 0 & h_{3k} & h_{2k} & h_{1k} & 0 \\ 0 & 0 & h_{3k} & h_{2k} & h_{1k} \\ h_{1k} & 0 & 0 & h_{3k} & h_{2k} \end{bmatrix} \tag{A.6}$$

A.2 Spectral decomposition

A.2.1 General definitions

In mathematics, a matrix $\mathbf{A}$ is normal is $\mathbf{A}^H\mathbf{A} = \mathbf{A}\mathbf{A}^H$ where $(\cdot)^H$ is the conjugate operator. A normal matrix is diagonalizable by a unitary matrix[1] as below

$$\mathbf{A} = \mathbf{U}\mathbf{\Lambda}\mathbf{U}^H \tag{A.7}$$

where $\mathbf{\Lambda}$ is a diagonal matrix whose elements are the eigenvalues of $\mathbf{A}$.

A.2.2 Spectral decomposition of a BCCB matrix

Any BCCB matrix $\mathbf{H}$ is normal and has a spectral decomposition of the form

$$\mathbf{H} = \mathbf{F}^H\mathbf{\Lambda}\mathbf{F} \tag{A.8}$$

[1] A matrix $\mathbf{U}$ is unitary is $\mathbf{U}^H = \mathbf{U}^{-1}$

where $\mathbf{F}$ is 2D unitary discrete Fourier transform. Thus, the linear model (A.2) can be implemented by

$$\boldsymbol{y} = \text{ifft2D}(\text{fft2D}(\boldsymbol{x}) \cdot \text{fft2D}(\boldsymbol{h})) \tag{A.9}$$

where zero-padding is necessary to make sure all the images in (A.9) of the same size.

Appendix B

Appendices of Chapter 2

B.1 Determinations of the conditional distributions of the noise variance and scale parameters

Inverse gamma distribution A univariate inverse gamma distribution with shape parameter α and scale parameter β denoted as $\mathcal{IG}(\alpha, \beta)$ has the following pdf

$$p(x) = \frac{\beta^\alpha}{\Gamma(\alpha)} x^{-\alpha-1} \exp\left(-\frac{\beta}{x}\right) \imath_{\mathbb{R}^+}(x) \tag{B.1}$$

where $\imath_C$ is an indicator function on the set C. The conditional distribution of the noise variance and of the GGD scale parameters of the joint posterior distribution, i.e., (2.14) and (2.18) are inverse gamma distributions that are derived hereinafter.

Conditional distribution of the noise variance

$$\begin{aligned} p(\sigma_n^2|\mathbf{y}, \mathbf{x}, \boldsymbol{\xi}, \boldsymbol{\gamma}, \mathbf{z}) &\propto p(\mathbf{y}|\mathbf{x}, \sigma_n^2, \boldsymbol{\xi}, \boldsymbol{\gamma}, \mathbf{z}) p(\sigma_n^2) \\ &\propto \frac{1}{(2\pi\sigma_n^2)^{\frac{N}{2}}} \exp\left(-\frac{\|\mathbf{y} - \mathbf{H}\mathbf{x}\|_2^2}{2\sigma_n^2}\right) \times \frac{\nu^\alpha \exp\left(-\nu/\sigma_n^2\right)}{\Gamma(\alpha)(\sigma_n^2)^{\alpha+1}} \\ &\propto (\sigma_n^2)^{-\alpha-N/2-1} \times \exp\left[-\frac{1}{\sigma_n^2}\left(\nu + \frac{1}{2}\|\mathbf{y} - \mathbf{H}\mathbf{x}\|_2^2\right)\right]. \end{aligned}$$

We can recognize the following inverse gamma distribution

$$\mathcal{IG}\left(\alpha + N/2, \theta + \frac{1}{2}\|\mathbf{y} - \mathbf{H}\mathbf{x}\|_2^2\right).$$

Conditional distribution of the scale parameters

$$\begin{aligned} p(\gamma_k|\mathbf{x}, \boldsymbol{\xi}, \mathbf{z}, \boldsymbol{\gamma}_{-k}) &\propto p(\mathbf{x}_k|\xi_k, \gamma_k, \mathbf{z}_k)p(\gamma_k) \\ &\propto a_k^{N_k} \exp\left(-\frac{\|\mathbf{x}_k\|_{\xi_k}^{\xi_k}}{\gamma_k}\right) \frac{1}{\gamma_k} \mathcal{I}_{\mathbb{R}+}(\gamma_k) \\ &\propto \gamma_k^{-N_k/\xi_k - 1} \exp\left(-\frac{\|\mathbf{x}_k\|_{\xi_k}^{\xi_k}}{\gamma_k}\right). \end{aligned}$$

We can recognize the following inverse gamma distribution

$$\mathcal{IG}\left(\frac{N_k}{\xi_k}, \|\mathbf{x}_k\|_{\xi_k}^{\xi_k}\right).$$

B.2 Sampling the shape parameters with an RWMH Algorithm

In order to sample the shape parameter ξ_k following (2.16), we generate a candidate using a proposal and accept or reject this candidate with an appropriate acceptance ratio. The proposal used in this manuscript is a truncated Gaussian distribution whose mean is $\xi_k^{(t)}$ (the value of the parameter generated at the previous iteration) and whose variance δ is adjusted in order to obtain a suitable average acceptance ratio, i.e.,

$$\xi_k^* \sim \mathcal{N}(\xi_k^{(t)}, \delta)\mathcal{I}_{(0,3)}(\xi_k^*). \tag{B.2}$$

This candidate is then accepted or rejected according to the following ratio

$$\rho = \min\left\{\frac{p(\xi_k^*|\mathbf{x}, \boldsymbol{\gamma}, \mathbf{z}, \boldsymbol{\xi}_{-k})}{p(\xi_k^t|\mathbf{x}, \boldsymbol{\gamma}, \mathbf{z}, \boldsymbol{\xi}_{-k})}, 1\right\}. \tag{B.3}$$

We propose to adjust the stepsize δ every 100 iterations to achieve a reasonable acceptance rate $(30\% - 90\%)$ [Per15]. Specifically, if the acceptance ratio during the previous 100 iterations is larger than 90% (respectively smaller than 30%), than the variance δ is decreased (respectively increased) of 20% compared to its previous value. Note that to ensure the homogeneity of the Markov chain after the burn-in period, this tuning procedure is only executed during the burn-in period. The stepsize is then fixed during the following iterations.

The algorithm used to sample ξ_k is finally divided into three procedures that are summarized in Algorithm 8.

Algorithm 8: Adjusted RWMH Algorithm

```
   /* Initialization                                                    */
1  Choose an initial value ξ_0;
   /* Candidate Generation                                              */
2  for t = 1 : N_MC do
3  |  ξ_k^* ~ N(ξ_k^(t), δ) I_(0,3)(ξ_k^*);
   |  /* Accept/Reject Procedure                                        */
4  |  if rand ⩽ ρ then
5  |  |  ξ_k^(t+1) = ξ_k^*;
6  |  else
7  |  |  ξ_k^(t+1) = ξ_k^(t);
8  |  end
9  |  Adjust δ in order to obtain a suitable acceptance rate.
10 end
```

B.3 Sampling the TRF using an Hamiltonian Monte Carlo Algorithm

B.3.1 HMC Algorithm

The main idea of the Hamiltonian Monte Carlo(HMC) algorithm is to introduce a vector of momentum variables $\mathbf{p} \in \mathbb{R}^N$ that is independent of $\mathbf{x}$ and to sample the pair $(\mathbf{x}, \mathbf{p})$ instead of just sampling $\mathbf{x}$. The conditional distribution of $(\mathbf{x}, \mathbf{p})$ can be written

$$p(\mathbf{x}, \mathbf{p}|\mathbf{y}, \sigma_n^2, \boldsymbol{\xi}, \boldsymbol{\gamma}, \mathbf{z}) = p(\mathbf{x}|\mathbf{y}, \sigma_n^2, \boldsymbol{\xi}, \boldsymbol{\gamma}, \mathbf{z})p(\mathbf{p}).$$

The Hamiltonian of the system is defined as

$$H(\mathbf{x}, \mathbf{p}) \triangleq -\log p(\mathbf{x}, \mathbf{p}|\mathbf{y}, \sigma_n^2, \boldsymbol{\xi}, \boldsymbol{\gamma}, \mathbf{z}) = U(\mathbf{x}) + V(\mathbf{p})$$

where $V(\mathbf{p})$ and $U(\mathbf{x})$ are the kinetic and potential energies of the Hamiltonian system. They are defined as

$$V(\mathbf{p}) = \frac{1}{2}\mathbf{p}^T\mathbf{p} \text{ and } U(\mathbf{x}) = -\log[p(\mathbf{x}|\mathbf{y}, \sigma_n^2, \boldsymbol{\xi}, \boldsymbol{\gamma}, \mathbf{z})].$$

At the iteration $\#t$, the HMC consists of two steps:

- generate a candidate pair $(\mathbf{p}^{(\star)}, \mathbf{x}^{(\star)})$ from the current state $(\mathbf{p}^{(t)}, \mathbf{x}^{(t)})$ using a discretizing method, such as the leapfrog and Euler methods;
- accept or reject the candidate with the probability ρ

$$\rho = \min\{\exp[H(\mathbf{p}^{(t)}, \mathbf{x}^{(t)}) - H(\mathbf{p}^{(\star)}, \mathbf{x}^{(\star)})], 1\}. \tag{B.4}$$

In our experiments, we have considered the leapfrog discretizing method due to its better performance compared to the Euler method, also noticed in [Nea11]. The three steps of the leapfrog method are defined as

$$\begin{aligned} \mathbf{p}_i(t+\epsilon/2) &= \mathbf{p}_i(t) - \frac{\epsilon}{2}\frac{\partial U}{\partial \mathbf{x}_i}[\mathbf{x}(t)] \\ \mathbf{x}_i(t+\epsilon) &= \mathbf{x}_i(t) + \epsilon \mathbf{p}_i(t+\epsilon/2) \\ \mathbf{p}_i(t+\epsilon) &= \mathbf{p}_i(t+\epsilon/2) - \frac{\epsilon}{2}\frac{\partial U}{\partial \mathbf{x}_i}[\mathbf{x}(t+\epsilon)] \end{aligned}$$

where ϵ is a so-called stepsize and L is the number of leapfrog iterations. We should note that $U(\mathbf{x})$ is not differentiable when $\xi_k \leqslant 1$. To deal with this problem, a smoothing approximation has been considered, i.e., $|\cdot| \approx \sqrt{\cdot^2 + \varepsilon}$, with $\varepsilon \ll 1$. The algorithm based on the leapfrog discretization and this approximation is summarized in Algorithm 9. Compared to other MCMC algorithms, the HMC method has the noticeable advantage to generate efficiently a candidate $\mathbf{x}$ even in the case of a high dimensional and complicated distribution.

B.3.2 Tuning the parameters ϵ and L

The performance of the HMC algorithm mainly depends on the values of the parameters ϵ (stepsize) and L (number of leapfrog steps). Fortunately, these two parameters can be tuned independently in most applications [Nea11]. It is recommended to select a random number of leapfrog steps L to avoid possible periodic trajectories [Nea11]. In our algorithm, L is sampled uniformly in the interval $[50, 70]$. The leapfrog stepsize ϵ has been adjusted in order to ensure a reasonable average acceptance rate any 100 iterations. Specifically, when the acceptance rate is too large, ϵ should

be decreased and vice versa. The range of the acceptance rate has been set to $30\% - 90\%$ in the burn-in period. Note that the tuning of ϵ is just carried out during the burn-in period to ensure the Markov chain is homogeneous after the burn-in period. The acceptance rate generally belongs to the interval $60\% - 80\%$ when the Markov chain has converged, while the acceptance rate is around 25% in standard MH moves for high dimensional target distributions [GCC11].

Algorithm 9: Adjusted HMC Algorithm

`/* Initialization */`

$\mathbf{x}^{(0)} = \mathbf{y}$;

for $t = 1 : N_{MC}$ **do**

`/* Candidate generation */`

$\mathbf{p}^{(t,0)} \sim N(\mathbf{0}, \mathbf{I}^{N\times N})$;

`/* Leapfrog Method */`

for $i = 1 : L$ **do**

Set $\mathbf{p}^{(t,i)} = \mathbf{p}^{(t,i)} - \frac{\epsilon}{2}\frac{\partial U}{\partial \mathbf{x}^{(t,i)}}\mathbf{x}^{(t,i)}$;

Set $\mathbf{x}^{(t,i)} = \mathbf{x}^{(t,i)} + \epsilon\mathbf{p}^{(t,i)}$;

Set $\mathbf{p}^{(t,i)} = \mathbf{p}^{(t,i)} - \frac{\epsilon}{2}\frac{\partial U}{\partial \mathbf{x}}\mathbf{x}^{(t,i)}$;

end

$\mathbf{p}^{(*)} = \mathbf{p}^{(t,L)}$;

$\mathbf{x}^{(*)} = \mathbf{x}^{(t,L)}$;

`/* Accept/Reject Procedure */`

Compute ρ with (B.4)

if $rand \leqslant \rho$ **then**

$\mathbf{x}^{(t+1)} = \mathbf{x}^{(*)}$;

else

$\mathbf{x}^{(t+1)} = \mathbf{x}^{(t)}$;

end

Adjust ϵ in order to obtain a suitable acceptance rate.

end

Appendix C

Appendices of Chapter 3

C.1 Derivation of the analytical solution (3.13)

The computational details for obtaining the result in (3.13) from (3.7) are summarized hereinafter. First, denoting $\mathbf{r} = \mathbf{H}^H\mathbf{S}^H\mathbf{y} + 2\tau\mathbf{A}^H\mathbf{v}$, the solution (3.7) is

$$\begin{aligned}\hat{\mathbf{x}} &= (\mathbf{H}^H\underline{\mathbf{S}}\mathbf{H} + 2\tau\mathbf{A}^H\mathbf{A})^{-1}\mathbf{r} \\ &= \mathbf{F}^H\left(\mathbf{\Lambda}^H\mathbf{F}\underline{\mathbf{S}}\mathbf{F}^H\mathbf{\Lambda} + 2\tau\mathbf{F}\mathbf{A}^H\mathbf{A}\mathbf{F}^H\right)^{-1}\mathbf{F}\mathbf{r}. \end{aligned} \tag{C.1}$$

Based on Lemma 1, $\mathbf{\Lambda}^H\mathbf{F}\underline{\mathbf{S}}\mathbf{F}^H\mathbf{\Lambda}$ is computed as

$$\begin{aligned} & \mathbf{\Lambda}^H\mathbf{F}\underline{\mathbf{S}}\mathbf{F}^H\mathbf{\Lambda} \\ = \ & \frac{1}{d}\mathbf{\Lambda}^H\left(\mathbf{J}_d \otimes \mathbf{I}_{N_l}\right)\mathbf{\Lambda} && \text{(C.2)} \\ = \ & \frac{1}{d}\mathbf{\Lambda}^H\left(\left(\mathbf{1}_d\mathbf{1}_d^T\right) \otimes \left(\mathbf{I}_{N_l}\mathbf{I}_{N_l}\right)\right)\mathbf{\Lambda} && \text{(C.3)} \\ = \ & \frac{1}{d}\mathbf{\Lambda}^H\left(\mathbf{1}_d \otimes \mathbf{I}_{N_l}\right)\left(\mathbf{1}_d^T \otimes \mathbf{I}_{N_l}\right)\mathbf{\Lambda} && \text{(C.4)} \\ = \ & \frac{1}{d}\left(\mathbf{\Lambda}^H[\underbrace{\mathbf{I}_{N_l},\cdots,\mathbf{I}_{N_l}}_{d}]^T\right)\left([\underbrace{\mathbf{I}_{N_l},\cdots,\mathbf{I}_{N_l}}_{d}]\mathbf{\Lambda}\right) && \text{(C.5)} \\ = \ & \frac{1}{d}\underline{\mathbf{\Lambda}}^H\underline{\mathbf{\Lambda}}. && \text{(C.6)} \end{aligned}$$

Note that (C.3) was obtained from (C.2) by replacing $\mathbf{J}_d$ by $\mathbf{1}_d\mathbf{1}_d^T$, where $\mathbf{1}_d \in \mathbb{R}^{d\times 1}$ is a vector of ones. Obtaining (C.4) from (C.3) is straightforward using the following property of the Kronecker product $\otimes$

$$\mathcal{A}\mathcal{B} \otimes \mathcal{C}\mathcal{D} = (\mathcal{A}\otimes\mathcal{C})(\mathcal{B}\otimes\mathcal{D}).$$

In (C.5), $\mathbf{\Lambda} \in \mathbb{R}^{N_h \times N_h}$ whereas $[\mathbf{I}_{N_l}, \cdots, \mathbf{I}_{N_l}] \in \mathbb{R}^{N_l \times N_h}$ and $[\mathbf{I}_{N_l}, \cdots, \mathbf{I}_{N_l}]^T \in \mathbb{R}^{N_h \times N_l}$ are block matrices whose blocks are equal to the identity matrix $\mathbf{I}_{N_l}$. The matrix $\underline{\mathbf{\Lambda}} \in \mathbb{R}^{N_l \times N_h}$ in (C.6) is given by

$$\begin{aligned}
\underline{\mathbf{\Lambda}} &= [\mathbf{I}_{N_l}, \cdots, \mathbf{I}_{N_l}]\mathbf{\Lambda} \\
&= [\mathbf{I}_{N_l}, \cdots, \mathbf{I}_{N_l}]\text{diag}\mathbf{\Lambda}_1, \cdots, \mathbf{\Lambda}_d \\
&= [\mathbf{I}_{N_l}, \cdots, \mathbf{I}_{N_l}] \begin{bmatrix} \mathbf{\Lambda}_1 & \cdots & 0 \\ \vdots & \ddots & \vdots \\ 0 & \cdots & \mathbf{\Lambda}_d \end{bmatrix} \qquad \text{(C.7)} \\
&= [\mathbf{\Lambda}_1, \mathbf{\Lambda}_2, \cdots, \mathbf{\Lambda}_d]. \qquad \text{(C.8)}
\end{aligned}$$

As a consequence, (C.1) can be written as in (3.9), i.e.,

$$\begin{aligned}
\hat{\mathbf{x}} &= \mathbf{F}^H \left(\frac{1}{d} \underline{\mathbf{\Lambda}}^H \underline{\mathbf{\Lambda}} + 2\tau \mathbf{F}\mathbf{A}^H \mathbf{A}\mathbf{F}^H \right)^{-1} \mathbf{F}\mathbf{r} \qquad \text{(C.9)} \\
&= \mathbf{F}^H \left[\frac{1}{2\tau}\mathbf{\Psi} - \frac{1}{2\tau}\mathbf{\Psi}\underline{\mathbf{\Lambda}}^H \left(d\mathbf{I}_{N_l} + \frac{1}{2\tau}\underline{\mathbf{\Lambda}}\mathbf{\Psi}\underline{\mathbf{\Lambda}}^H \right)^{-1} \underline{\mathbf{\Lambda}}\mathbf{\Psi}\frac{1}{2\tau} \right] \mathbf{F}\mathbf{r} \qquad \text{(C.10)} \\
&= \frac{1}{2\tau}\mathbf{F}^H\mathbf{\Psi}\mathbf{F}\mathbf{r} - \frac{1}{2\tau}\mathbf{F}^H\mathbf{\Psi}\underline{\mathbf{\Lambda}}^H \left(2\tau d\mathbf{I}_{N_l} + \underline{\mathbf{\Lambda}}\mathbf{\Psi}\underline{\mathbf{\Lambda}}^H \right)^{-1} \underline{\mathbf{\Lambda}}\mathbf{\Psi}\mathbf{F}\mathbf{r} \qquad \text{(C.11)}
\end{aligned}$$

where $\mathbf{\Psi} = \mathbf{F}\left(\mathbf{A}^H\mathbf{A}\right)^{-1}\mathbf{F}^H$. The Lemma 2 is adopted from (C.9) to (C.10) with $\mathbf{A}_1 = 2\tau\mathbf{F}\mathbf{A}^H\mathbf{A}\mathbf{F}^H$, $\mathbf{A}_2 = \underline{\mathbf{\Lambda}}^H$, $\mathbf{A}_3 = \frac{1}{d}\mathbf{I}$ and $\mathbf{A}_4 = \underline{\mathbf{\Lambda}}$. Note that the matrices $\mathbf{A}_1$ and $\mathbf{A}_3$ are always invertible, implying that the Woodbury formula can be applied.

C.2 Pseudo codes of the proposed fast ADMM super-resolution methods for TV and ℓ_1-norm regularizations

Algorithm 10: FSR with TV regularization

Input: $\mathbf{y}$, $\mathbf{H}$, $\mathbf{S}$, τ, d, $\mathbf{D}_\mathrm{h}$ and $\mathbf{D}_\mathrm{v}$

Set $k=0$, choose $\mu>0$, $\mathbf{d}^0$, $\mathbf{u}^0$;

// Factorization of matrix $\mathbf{H}$

$\mathbf{H}=\mathbf{F}^H\mathbf{\Lambda}\mathbf{F}$;

$\underline{\mathbf{\Lambda}}=[\mathbf{\Lambda}_1,\mathbf{\Lambda}_2,\cdots,\mathbf{\Lambda}_d]$;

// Factorization of matrices $\mathbf{D}_\mathrm{h}$ *and* $\mathbf{D}_\mathrm{v}$

$\mathbf{D}_\mathrm{h}=\mathbf{F}^H\mathbf{\Sigma}_\mathrm{h}\mathbf{F}$;

$\mathbf{D}_\mathrm{v}=\mathbf{F}^H\mathbf{\Sigma}_\mathrm{v}\mathbf{F}$;

$\mathbf{\Psi}=(\mathbf{\Sigma}_\mathrm{h}^H\mathbf{\Sigma}_\mathrm{h}+\mathbf{\Sigma}_\mathrm{v}^H\mathbf{\Sigma}_\mathrm{v})^{-1}$;

Repeat

// Update $\mathbf{x}$ *using Theorem 1*

$\boldsymbol{\rho}_\mathrm{h}=\mathbf{u}_\mathrm{h}^k-\mathbf{d}_\mathrm{h}^k$;

$\boldsymbol{\rho}_\mathrm{v}=\mathbf{u}_\mathrm{v}^k-\mathbf{d}_\mathrm{v}^k$;

$\mathbf{Fr}=\mathbf{F}(\mathbf{H}^H\mathbf{S}^H\mathbf{y}+\mu\mathbf{D}_\mathrm{h}\boldsymbol{\rho}_\mathrm{h}+\mu\mathbf{D}_\mathrm{v}\boldsymbol{\rho}_\mathrm{v})$;

$\mathbf{x}_f=\left(\mathbf{\Psi}\underline{\mathbf{\Lambda}}^H\left(\mu d\mathbf{I}_{N_l}+\underline{\mathbf{\Lambda}}\mathbf{\Psi}\underline{\mathbf{\Lambda}}^H\right)^{-1}\underline{\mathbf{\Lambda}}\mathbf{\Psi}\right)\mathbf{Fr}$;

$\mathbf{x}^{k+1}=\frac{1}{\mu}\mathbf{F}^H\mathbf{\Psi}\mathbf{Fr}-\frac{1}{\mu}\mathbf{F}^H\mathbf{x}_f$;

// Update $\mathbf{u}$ *using the vector-soft-thresholding operator*

$\boldsymbol{\nu}=[\mathbf{D}_\mathrm{h}\mathbf{x}^{k+1}+\mathbf{d}_\mathrm{h}^k,\mathbf{D}_\mathrm{v}\mathbf{x}^{k+1}+\mathbf{d}_\mathrm{v}^k]$;

$\mathbf{u}^{k+1}[i]=\max\{\mathbf{0},\|\boldsymbol{\nu}[i]\|_2-\tau/\mu\}\frac{\boldsymbol{\nu}[i]}{\|\boldsymbol{\nu}[i]\|_2}$;

// Update the dual variables $\mathbf{d}$

$\mathbf{d}^{k+1}=\mathbf{d}^k+(\mathbf{A}\mathbf{x}^{k+1}-\mathbf{u}^{k+1})$;

$k=k+1$;

until stopping criterion is satisfied;

Output: $\hat{\mathbf{x}}=\mathbf{x}^k$.

Algorithm 11: FSR with ℓ_1-norm regularization in the wavelet domain

Input: $\mathbf{y}$, $\mathbf{H}$, $\mathbf{S}$, τ, d

Set $k = 0$, choose $\mu > 0$, $\mathbf{d}^0$, $\mathbf{u}^0$;

// Factorization of matrix $\mathbf{H}$

$\mathbf{H} = \mathbf{F}^H \mathbf{\Lambda} \mathbf{F}$;

$\underline{\mathbf{\Lambda}} = [\mathbf{\Lambda}_1, \mathbf{\Lambda}_2, \cdots, \mathbf{\Lambda}_d]$;

Repeat

// Update $\boldsymbol{\theta}$ *using Theorem 1*

$\mathbf{Fr} = \mathbf{F}(\mathbf{H}^H \mathbf{S}^H \mathbf{y} + \mu \mathbf{W}(\mathbf{u}^k - \mathbf{d}^k)$;

$\mathbf{x}_f = \left(\underline{\mathbf{\Lambda}}^H \left(\mu d \mathbf{I}_{N_l} + \underline{\mathbf{\Lambda}} \underline{\mathbf{\Lambda}}^H \right)^{-1} \underline{\mathbf{\Lambda}} \right) \mathbf{Fr}$;

$\mathbf{x}^{k+1} = \frac{1}{\mu} \mathbf{Fr} - \frac{1}{\mu} \mathbf{x}_f$;

// Update $\mathbf{u}$ *using the soft-thresholding operator*

$\boldsymbol{\nu} = \mathbf{W}^H \mathbf{x}^{k+1} + \mathbf{d}^k$;

$\mathbf{u}^{k+1} = \max\{0, |\boldsymbol{\nu}| - \tau/\mu\}$; // $|\boldsymbol{\nu}| \triangleq [|\boldsymbol{\nu}_1|, \cdots, |\boldsymbol{\nu}_M|]^T \in \mathbb{R}^{M \times 1}$

// Update the dual variables $\mathbf{d}$

$\mathbf{d}^{k+1} = \mathbf{d}^k + (\mathbf{W}^H \mathbf{x}^{k+1} - \mathbf{u}^{k+1})$;

$k = k + 1$;

until stopping criterion is satisfied;

Output: $\hat{\mathbf{x}} = \mathbf{x}^k$.

Appendix D

Calculation of proximity operators

D.1 Definition

Let $f : \mathbb{R}^N \to (-\infty, +\infty]$ be a proper and lower semicontinuous function. For every $\mathbf{x} \in \mathbb{R}^N$, the minimization problem

$$\arg\min_{\mathbf{y}} f(\mathbf{y}) + \frac{1}{2}\|\mathbf{x} - \mathbf{y}\|^2 \tag{D.1}$$

admits a unique solution, which is defined as $\text{prox}_f(\mathbf{x})$. The operator $\text{prox}_f : \mathbb{R}^N \to \mathbb{R}^N$ thus defined is the proximity operator of f. We often encounter the proximity operator of the scaled function τf, where $\tau > 0$, which can be expressed as

$$\text{prox}_{\tau f}(\mathbf{x}) = \arg\min_{\mathbf{y}} f(\mathbf{y}) + \frac{1}{2\tau}\|\mathbf{x} - \mathbf{y}\|^2 \tag{D.2}$$

This is also called the proximity operator of f with parameter τ.

D.2 Proximity operator of $|x|^p$

Since proximity operator is an element-to-element arithmetic, we just calculate the proximity operator for a scalar hereinafter. Denoting $P(x) \triangleq \frac{1}{2}|w - x|^2 + \tau|x|^p$, calculating the proximity operator of $|\cdot|^p$ can be formulated as below

$$\text{prox}_{\tau|\cdot|^p}(w) = \arg\min_{x} P(x), \tag{D.3}$$

We note that this problem has been explored in different applications, e.g., in [ALP02, MS12, ZMZ+13] for $0 < p \leq 1$ and in [CCPW07, CP11] for $p \geq 1$.

In order to solve (D.3), we first note that the variables satisfy the relationship $\text{sgn}(x) = \text{sgn}(w)$. Otherwise, the problem $P(x)$ is minimized at $x = 0$. In the following, we just consider $x > 0$ without

loss of generality. Since $P(x)$ is differential when $x > 0$, by setting $P'(x) = 0$, we have

$$g(x) \triangleq x + \tau p x^{p-1} = |w| \tag{D.4}$$

Thus, finding the minimizer of the problem (D.3) has been transferred into looking for the solution of the equation $g(x) = |w|$.

- $0 < p \leq 1$

  In order to find the solution of the equation $g(x) = |w|$, we calculate the first and second order derivatives of $g(x)$ as below

$$g'(x) = 1 - \tau p(1-p)x^{p-2}$$
$$g''(x) = \tau p(1-p)(2-p)x^{p-3} > 0$$

  By setting $g'(x) = 0$, we get the critical point of $g(x)$, i.e., $x_c = [\tau p(1-p)]^{\frac{1}{2-p}}$. Since $g''(x) > 0$ for all $x > 0$, $g(x)$ is convex for $x > 0$, as shown in Fig. D.1. Furthermore, by denoting as $x_* > 0$ a minimizer of $P(x)$, we should make sure that $P(x_*) \leq P(0)$, i.e.,

$$\begin{aligned} P(x_*) &= \frac{1}{2}|x_* - w|^2 + \tau x_*^p \\ &= \frac{1}{2}w^2 + \frac{1}{2}x_*^2 - x_*|w| + \tau x_*^p \\ &= P(0) + \frac{1}{2}x_*^p(2\tau + x_*^{2-p} - 2x_*^{1-p}w) \\ &= P(0) + \frac{1}{2}x_*^p(2\tau + x_*^{2-p} - 2\tau p - 2x_*^{2-p}) \\ &= P(0) + \frac{1}{2}x_*^p(2\tau(1-p) - x_*^{2-p}) \\ &= P(0) + \frac{1}{2}x_*^p(x_a^{2-p} - x_*^{2-p}) \end{aligned} \tag{D.5}$$

  Thus, by denoting $x_a = [2\tau(1-p)]^{\frac{1}{2-p}}$, we have $P(x_*) \leq P(0)$ iff $x_* \geq x_a$, which is equivalent to $|w| \geq g(x_a)$ since $g(x)$ is strictly increasing for $x > x_c$. Thus,

$$\text{prox}_{\tau|\cdot|^p}(w) = \begin{cases} 0 & |w| < g(x_a) \\ x_* \text{sgn}(w) & |w| \geq g(x_a) \end{cases} \tag{D.6}$$

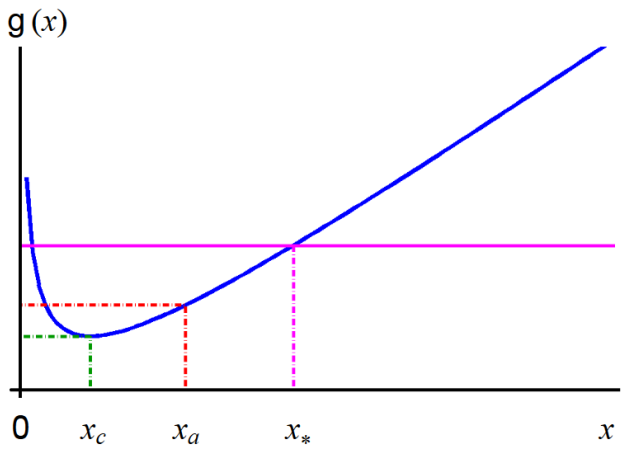

Figure D.1: Plot of $g(x)$ for $x > 0$.

or equivalently

$$\text{prox}_{\tau|\cdot|^p}(w) = x_* \text{sgn}(w) \max(0, |w| - \chi) \tag{D.7}$$

where $\chi = g(x_a) = [2\tau(1-p)]^{\frac{1}{2-p}} + \tau p[2\tau(1-p)]^{\frac{p-1}{2-p}}$ and x_* is the solution of equation $g(x) = |x|$ which satisfies $x_* \geq x_a$. However, we note that there are two solutions to $g(x) = |x|$, how to determine x_* which satisfies $x_* \geq x_a$(larger solution) seems challenging. In [MS12], a fixed point iteration method is proposed to calculate x_* from the following iteration

$$x_{k+1} = f(x_k) \quad \text{where} \quad f(x) = |w| - \tau p x^{p-1} \tag{D.8}$$

with the initial condition $x_0 \in \{x_a, |w|\}$.

- $1 < p \leq 2$

  Because the problem (D.3) is strongly convex when $1 < p \leq 2$, we have

$$\text{prox}_{|\cdot|^p}(w) = x_* \text{sgn}(w) \tag{D.9}$$

  where x_* is the unique solution to $g(x) = |w|$ which satisfies $x_* > 0$. We should also note that (D.9) is validate for $p > 2$, but we are just interested in $0 < p \leq 2$ in this thesis. Moreover, calculating the closed-form solution to $g(x) = |w|$ is complicated even though x_* is a unique positive solution. Thus, a Newton method is proposed to find the root of $g(x) = |w|$ (The

fixed point method mentioned above is not valid here since its convergence condition cannot be guaranteed for $p > 1$ [FB85]). Besides, the analytical solution of (D.3) when $p = \{4/3, 3/2\}$ is calculated in [CCPW07].

In summary, we have the proximity operator for the problem (D.3) is defined as

$$\text{prox}_{|\cdot|^p}(w) = \begin{cases} x_* \text{sgn}(w) \max(0, |w| - \chi) & 0 < p \leq 1 \\ x_* \text{sgn}(w) & 1 < p \leq 2 \end{cases} \tag{D.10}$$

Appendix E

Proximal hamiltonian Monte Carlo (PHMC) method

E.1 Proximal Metropolis adjusted Langevin algorithm

The proximal Metropolis adjusted Langevin algorithm (PMALA) was proposed by Pereyra in [Per15] to handle high-dimensional models used in several challenging problems such as image deconvolution, audio compressive sensing and so on. The basic idea of [Per15] is to combine the traditional MALA and the proximal technique which is well-known to handle the non-differential functions efficiently. The Metropolis adjusted Langevin algorithm (MALA), which comes from the discretization of the ordinary Langevin diffusion can be expressed with the following first-order Euler discretisation technique [RT96]

$$\mathbf{x}^{n+1} = \mathbf{x}^n + \frac{\epsilon}{2}\frac{\partial U}{\partial \mathbf{x}^n}(\mathbf{x}^n) + \sqrt{\epsilon}\mathbf{d}^n \tag{E.1}$$

where $U(\mathbf{x})$ is the target distribution, $\mathbf{d}$ is the realization of a zero mean Gaussian noise and ϵ is the stepsize. To form a Markov chain, it may be more convenient to rewrite (E.1) as a state transition as below

$$\mathbf{x}^{n+1}|\mathbf{x}^n \sim \mathcal{N}\left(\mathbf{x}^n + \frac{\epsilon}{2}\frac{\partial U}{\partial \mathbf{x}^n}(\mathbf{x}^n), \epsilon\mathbf{d}^n\right) \tag{E.2}$$

where $\mathbf{x}^n + \frac{\epsilon}{2}\frac{\partial U}{\partial \mathbf{x}^n}(\mathbf{x}^n)$ is the proposal density of the Markov chain. The PMALA is based on a new proposal density based on proximity operator that can be expressed as follows

$$\mathbf{x}^{n+1}|\mathbf{x}^n \sim \mathcal{N}\left(\text{prox}_U^{\epsilon/2}(\mathbf{x}^n), \epsilon\mathbf{d}^n\right) \tag{E.3}$$

After a candidate $\mathbf{x}^*$ has been generated by using (E.2) or (E.3), we accept this candidate with probability

$$\rho = \min\left\{\frac{p(\mathbf{x}^*)q(\mathbf{x}^n|\mathbf{x}^*)}{p(\mathbf{x}^n)q(\mathbf{x}^*|\mathbf{x}^n)}, 1\right\} \tag{E.4}$$

where $p(\mathbf{x}) = \exp(-U(\mathbf{x}))$ and

$$q(\mathbf{x}^*|\mathbf{x}^n) = p_{\mathcal{N}}(\mathbf{x}^*|\mathbf{x}^n + \frac{\epsilon}{2}\frac{\partial U}{\partial \mathbf{x}^n}(\mathbf{x}^n), \epsilon\mathbf{d}^n) \text{ (MALA)} \tag{E.5}$$

or

$$q(\mathbf{x}^*|\mathbf{x}^n) = p_{\mathcal{N}}(\mathbf{x}^*|\text{prox}_U^{\epsilon/2}(\mathbf{x}^n), \epsilon\mathbf{d}^n). \text{ (PMALA)} \tag{E.6}$$

Note that the generated samples have a better mixing property and higher effective sample size (lower autocorrelation) compared with the traditional MALA for deconcolution problem, as shown in [Per15]. However, the computation time could increase due to the evaluating of the proximal operator (if the proximal operator is easy to be calculated, the computation time would not increase). We also note that Schreck *et. al.* [SFCM14] proposed another proximal based MALA algorithm for Bayesian variable selection.

E.2 Proximal Hamiltonian Monte Carlo algorithm

The HMC algorithm is another efficient sampling method for high dimensional problems (for an extensive review see [Nea11]). In HMC, an auxiliary momentum variable $\mathbf{q}$ which is independent and identically distributed *i.i.d.* according to a Gaussian distribution is introduced. The negative joint log density of $(\mathbf{x}, \mathbf{q})$ is defined as follows

$$H(\mathbf{x}, \mathbf{q}) = U(\mathbf{x}) + K(\mathbf{q}) \tag{E.7}$$

where $K(\mathbf{q}) = \frac{1}{2}\mathbf{q}^T\mathbf{q}$. The physical analogy of $H(\mathbf{x}, \mathbf{q})$, $U(\mathbf{x})$ and $K(\mathbf{q})$ are the Hamiltonian, potential energy and kinetic energy respectively. A discretizing leapfrog integrator which is employed to

approximate the Hamiltonian's equations is expressed as below

$$\mathbf{q}^n(i+\epsilon/2) = \mathbf{q}^n(i) - \frac{\epsilon}{2}\frac{\partial U}{\partial \mathbf{x}^n}(\mathbf{x}^n(i)) \tag{E.8}$$

$$\mathbf{x}^n(i+\epsilon) = \mathbf{x}^n(i) + \epsilon \mathbf{q}^n(i+\epsilon/2) \tag{E.9}$$

$$\mathbf{q}^n(i+\epsilon) = \mathbf{q}^n(i+\epsilon/2) - \frac{\epsilon}{2}\frac{\partial U}{\partial \mathbf{x}^n}(\mathbf{x}^n(i+\epsilon)) \tag{E.10}$$

where ϵ is the leapfrog stepsize. Denoting $\delta = \epsilon L$ (L is the number of leapfrog steps), the generated candidate state is

$$(\mathbf{x}^*, \mathbf{q}^*) = (\mathbf{x}^n(\delta), \mathbf{q}^n(\delta)). \tag{E.11}$$

Thus, the generated candidate is accepted with the ratio

$$\rho = \min\left\{\exp[H(\mathbf{x}^n, \mathbf{q}^n) - H(\mathbf{x}^*, \mathbf{q}^*)], 1\right\}. \tag{E.12}$$

In [CBCT15], a proximal Hamiltonian Monte Carlo (PHMC) algorithm is proposed for a denoising problem. The proposed PHMC algorithm is based on a modified leapfrog method, which is given as below

$$\mathbf{q}^n(i+\epsilon/2) = \mathbf{q}^n(i) + \mathrm{prox}_U^{\epsilon/2}(\mathbf{x}^n(i)) - \mathbf{x}^n(i) \tag{E.13}$$

$$\mathbf{x}^n(i+\epsilon) = \mathbf{x}^n(i) + \epsilon \mathbf{q}^n(i+\epsilon/2) \tag{E.14}$$

$$\mathbf{q}^n(i+\epsilon) = \mathbf{q}^n(i+\epsilon/2) + \mathrm{prox}_U^{\epsilon/2}(\mathbf{x}^n(i+\epsilon)) - \mathbf{x}^n(i+\epsilon) \tag{E.15}$$

E.3 Generalization to deconvolution problem

The deconvolution problem that we are considering has the following cost function

$$U(\mathbf{x}) = f(\mathbf{x}) + \phi(\mathbf{x}) \tag{E.16}$$

where $f(\mathbf{x})$ is the data fidelity term, which is highly related to the statistical properties of the noise. Under an additive white Gaussian noise (AWGN) assumption, the data fidelity term is expressed as

$$f(\mathbf{x}) = \frac{1}{2\sigma_n^2}\|\mathbf{y} - \mathbf{H}\mathbf{x}\|_2^2 \tag{E.17}$$

which is a quadratic and differential term. The second term in (E.16) $\phi(\mathbf{x})$ is the regularization/penalty term which depends on the properties of the image to be restored.

In this section, we generalize the PMALA and PHMC algorithms to be applied to a deconvolution problem based on the forward-backward (FB) splitting method. In the PMALA and PHMC algorithms mentioned above, the main problem is to calculate $\text{prox}_U^{\epsilon/2}(\mathbf{x})$. However, it is not possible to calculate this proximal operator in deconvolution problems due to the presence of the blurring kernel. One solution is to approximate it with a one-step forward-backward splitting algorithm, i.e.,

$$\text{prox}_U^{\epsilon/2}(\mathbf{x}) \approx \text{prox}_\phi^{\frac{\epsilon}{2}}\left(\mathbf{x} - \frac{\epsilon}{2}\nabla f(\mathbf{x})\right) \tag{E.18}$$

We also note that this approximation has been implemented in [Per15] for an image deconvolution problem with a total variation (TV) prior.

With the approximation (E.18), we can generalize the Euler discretization method (in PMALA) and the Leapfrog discretization method (in PHMC) to obtain (E.19) and (E.20) respectively

- PMALA

$$\mathbf{x}^{n+1} = \text{prox}_\phi^{\epsilon/2}\left(\mathbf{x}^n - \frac{\epsilon}{2}\nabla f(\mathbf{x}^n)\right) + \sqrt{\epsilon}\mathbf{d}^n. \tag{E.19}$$

- PHMC

$$\begin{aligned}
\mathbf{q}^n(i+\epsilon/2) &= \mathbf{q}^n(i) + \text{prox}_\phi^{\epsilon/2}\left(\mathbf{x}^n(i) - \frac{\epsilon}{2}\nabla f(\mathbf{x}^n(i))\right) - \mathbf{x}^n(i) \\
\mathbf{x}^n(i+\epsilon) &= \mathbf{x}^n(i) + \epsilon\mathbf{q}^n(i+\epsilon/2) \\
\mathbf{q}^n(i+\epsilon) &= \mathbf{q}^n(i+\epsilon/2) + \text{prox}_\phi^{\epsilon/2}\left(\mathbf{x}^n(i+\epsilon) - \frac{\epsilon}{2}\nabla f(\mathbf{x}^n(i+\epsilon))\right) - \mathbf{x}^n(i+\epsilon)
\end{aligned} \tag{E.20}$$

Thus, the forward-backward based MALA and HMC algorithms for image deconvolution are summarized in Algorithms 12 and 13.

Algorithm 12: PMALA Algorithm

```
   /* Initialization Procedure                                          */
1  x^0 = y;
2  for n = 0 : N_MC − 1 do
       /* Candidate generation Procedure                                */
3      x^{n+1} = prox_φ^{ϵ/2} (x^n − (ϵ/2)∇f(x^n)) + ϵd^n;
4      x* = x^{n+1};
       /* Accept/Reject Procedure                                       */
5      Compute ρ with (E.4)
6      if rand ⩽ ρ then
7          x^{n+1} = x*;
8      else
9          x^{n+1} = x_(t);
10     end
11     Adjust ϵ in order to obtain a suitable acceptance rate.
12 end
```

Algorithm 13: PHMC Algorithm

/* Initialization Procedure */

$\mathbf{x}^0 = \mathbf{y}$;

for $n = 0 : N_{MC} - 1$ **do**

  /* Candidate generation Procedure */

  $\mathbf{x}^0(0) = \mathbf{x}^0$;

  $\mathbf{q}^0(0) \sim N(\mathbf{0}, \mathbf{I}^{N\times N})$;

  for $i = 0 : L - 1$ **do**

    Compute $\mathbf{q}^n(i+\epsilon/2) = \mathbf{q}^n(i) + \text{prox}_{\phi}^{\epsilon/2}\left(\mathbf{x}^n(i) - \frac{\epsilon}{2}\nabla f(\mathbf{x}^n(i))\right) - \mathbf{x}^n(i)$;

    Compute $\mathbf{x}^n(i+\epsilon) = \mathbf{x}^n(i) + \epsilon\mathbf{q}^n(i+\epsilon/2)$;

    Compute $\mathbf{q}^n(i+\epsilon) = \mathbf{q}^n(i+\epsilon/2) + \text{prox}_{\phi}^{\epsilon/2}\left(\mathbf{x}^n(i+\epsilon) - \frac{\epsilon}{2}\nabla f(\mathbf{x}^n(i+\epsilon))\right) - \mathbf{x}^n_{(i+\epsilon)}$;

  end

  $\mathbf{q}^* = \mathbf{q}^n(\delta)$;

  $\mathbf{x}^* = \mathbf{x}^n(\delta)$;

  /* Accept/Reject Procedure */

  Compute ρ with (E.12)

  if $rand \leqslant \rho$ **then**

    $\mathbf{x}^{n+1} = \mathbf{x}^*$;

  else

    $\mathbf{x}^{n+1} = \mathbf{x}_{(t)}$;

  end

  Adjust ϵ in order to obtain a suitable acceptance rate.

end

Bibliography

[AAM05] Toygar Akgun, Yucel Altunbasak, and Russel M. Mersereau. Super-resolution reconstruction of hyperspectral images. *IEEE Trans. Image Process.*, 14(11):1860–1875, 2005.

[AD05] Hussein A. Aly and Eric Dubois. Image up-sampling using total-variation regularization with a new observation model. *IEEE Trans. Image Process.*, 14(10):1647–1659, 2005.

[Ale10] Martino Alessandrini. *Statistical Methods for Analysis and Processing of Medical Ultrasound-applications to segmentation and restoration.* PhD thesis, Universitá Di Bologna, 2010.

[ALP02] A. Antoniadis, D. Leporini, and J.-C. Pesquet. Wavelet thresholding for some classes of non-gaussian noise. *Statistica Neerlandica*, 56(4):434–453, 2002.

[AM10] Babak Mohammadzadeh Asl and Ali Mahloojifar. Eigenspace-based minimum variance beamforming applied to medical ultrasound imaging. *IEEE Trans. Ultrason. Ferroelectr. Freq. Control*, 57(11):2381–2390, 2010.

[AMD10] Hacheme Ayasso and Ali Mohammad-Djafari. Joint NDT image restoration and segmentation using Gauss-Markov-Potts prior models and variational Bayesian computation. *IEEE Trans. Image Process.*, 19(9):2265–2277, 2010.

[AMP+11] Martino Alessandrini, Simona Maggio, Jonathan Poree, Luca De Marchi, Nicolo Speciale, Emilie Franceschini, Olivier Bernard, and Olivier Basset. A restoration framework

for ultrasonic tissue characterization. *IEEE Trans. Ultrason. Ferroelectr. Freq. Control*, 58(11):2344–2360, 2011.

[APMS11] Martino Alessandrini, A. Palladini, Luca De Marchi, and Nicolo Speciale. Expectation maximization for joint deconvolution and statistics estimation. *Acoustical Imaging*, 30(11):335–343, 2011.

[AV07] David Arthur and Sergei Vassilvitskii. K-means++: The advantages of careful seeding. In *Proceedings of the Eighteenth Annual ACM-SIAM Symposium on Discrete Algorithms*, pages 1027–1035, Philadelphia, PA, USA, 2007.

[Bas08] Adrian Basarab. *Estimation du mouvement dans des s équences d'images échographiques: application à l'élastographie de la thyroid.* PhD thesis, INSA-Lyon, 2008.

[BCC+11] Leah Bar, TonyF. Chan, Ginmo Chung, Miyoun Jung, Nahum Kiryati, Rami Mohieddine, Nir Sochen, and LuminitaA. Vese. Mumford and shah model and its applications to image segmentation andimage restoration. In Otmar Scherzer, editor, *Handbook of Mathematical Methods in Imaging*, pages 1095–1157. Springer New York, 2011.

[BCN+] Richard Baraniuk, Hyeokho Choi, Ramesh Neelamani, Vinay Ribeiro, Justin Romberg, Haitao Guo, Felix Fernandes, Brent Hendricks, Ramesh Gopinath, Markus Lang, Jan Erik Odegard, Dong Wei, and Josh Jackson. Rice wavelet toolbox.

[BD06] Jose M. Bioucas-Dias. Bayesian wavelet-based image deconvolution: A GEM algorithm exploiting a class o heavy-tailed priors. *IEEE Trans. Image Process.*, 15(4):937–951, 2006.

[BDF07] José M. Bioucas-Dias and Mario A. T. Figueiredo. A new TwIST: Two-step iterative shrinkage/thresholding algorithms for image restoration. *IEEE Trans. Image Process.*, 16(12):2992–3004, 2007.

[Bes74] Julian Besag. Spatial interaction and the statistical analysis of lattice systems. *J. Roy. Stat. Soc. Ser. B*, 36(2):192–236, 1974.

[BHA+14] Olivier Bernard, Brecht Heyde, Martino Alessandrini, Daniel Barbosa, Sorina Camarasu-Pop, Frederic Cervenansky, Sebastien Valette, Oana Mirea, Elena Galli, Marcel Geleijnse, Alexandros Papachristidis, Johan G. Bosch, and Jan D'hooge. Challenge on endocardial three-dimensial ultrasound segmentation. In *MICCAI*, 2014.

[BML12] S. Benameur, M. Mignotte, and F. Lavoie. An homomorphic filtering and expectation maximization approach for the point spread function estimation in ultrasound imaging. In *SPIE 8295, Image Processing: Algorithms and Systems X; and Parallel Processing for Imaging Applications II*, 2012.

[BPC+11a] Stephen Boyd, Neal Parikh, Eric Chu, Borja Peleato, and Jonathan Eckstein. Distributed optimization and statistical learning via the alternating direction method of multipliers. *Foundations and Trends ® in Machine Learning*, 3(1):1–122, 2011.

[BPC+11b] Stephen Boyd, Neal Parikh, Eric Chu, Borja Peleato, and Jonathan Eckstein. Distributed optimization and statistical learning via the alternating direction method of multipliers. *Found. Trends Mach. Learn.*, 3(1):1–122, 2011.

[BPR+13] Alexandros Beskos, Natesh Pillai, Gareth Roberts, Jesus-Maria Sanz-Serna, and Andrew Stuart. Optimal tuning of the hybrid monte carlo algorithm. *Bernoulli*, 19(5A):1501–1534, 11 2013.

[BSK04] Leah Bar, Nir Sochen, and Nahum Kiryati. Variational pairing of image segmentation and blind restoration. In Tomas Pajdla and Jiri Matas, editors, *Computer Vision - ECCV 2004*, Lecture Notes in Computer Science, pages 166–177. Springer Berlin Heidelberg, 2004.

[BST14] Jerome Bolte, Shoham Sabach, and Marc Teboulle. Proximal alternating linearizad

minimization for noncovex and nonsmooth problems. *Math. Program.*, pages 459–494, Aug. 2014.

[BT09] Amir Beck and Marc Teboulle. A fast iterative shringkage-thresholding algorithm for linear inverse problems. *SIAM J. Imag. Sci.*, (1):183–202, March 2009.

[BTDF07] Olivier Bernard, Basma Touil, Jan DâĂŹhooge, and Denis Friboulet. Statistical modeling of the radio-frequency signal for partially- and fully-developed speckle based on a generalized Gaussian model with application to echocardiography. *IEEE Trans. Ultrason. Ferroelectr. Freq. Control*, 54(10):2189–2194, 2007.

[CBCT15] Lotfi Chaari, Hadj Batatia, Caroline Chaux, and Jean-Yves Tourneret. Sparse signal and image recovery using a proximal Bayesian algorithm. 2015.

[CCC+10] Antonin Chambolle, Vicent Caselles, Daniel Cremers, Matteo Novaga, and Thomas Pock. An introduction to total variation for image analysis. *Theoretical foundations and numerical methods for sparse recovery*, 9:263–340, 2010.

[CCPW07] Caroline Chaux, Patrick L. Combettes, Jean-Christophe Pesquet, and Valérie R. Wajs. A variational formulation for frame-based inverse problems. *Inv. Prob.*, pages 1495–1518, 2007.

[CE07] Patrizio Campisi and Karen Egiazarian. *Blind Image Deconvolution: Theory and Application*, chapter Deconvolution of Medical Images from Microscopic to Whole Body Images. CRC Press, 2007.

[CP11] Patrick L. Combettes and Jean-Christophe Pesquet. Proximal splitting methods in signal processing. In Heinz H. Bauschke, Regina S. Burachik, Patrick L. Combettes, Veit Elser, D. Russell Luke, and Henry Wolkowicz, editors, *Fixed-Point Algorithms for Inverse Problems in Science and Engineering*, Springer Optimization and Its Applications, pages 185–212. Springer New York, 2011.

[CPR] Emilie Chouzenoux, Jean-Christophe Pesquet, and Audrey Repetti. A block coordinate variable metric forward-backward algorithm.

[CPR14] Emilie Chouzenoux, Jean-Christophe Pesquet, and Audrey Repetti. Variable metric forward-backward algorithm for minimizing the sum of a differentiable function and a convex function. *Journal of Optimization Theory and Applications*, 162:107–132, July 2014.

[CPT+10] Lotfi Chaari, Jean-Christophe Pesquet, Jean-Yves Tourneret, Philippe Ciuciu, and Amel Benazza-Benyahia. A hierarchical Bayesian model for frame representation. *IEEE Trans. Signal Process.*, 58(11):5560–5571, 2010.

[CSJ+10] H. D. Cheng, Juan Shan, Wen Ju, Yanhui, and Ling Zhang. Automated breast cancer detection and classification using ultrasound images: a survey. *Pattern Recognition*, 43:299–317, Jan. 2010.

[CSJ11] Aladin Carovac, Fahrudin Smajlovic, and Dzelaludin Junuzovic. Application of ultrasound in medicine. *Application of ultrasound in medicine*, 19(3):168–171, 2011.

[CYZ14] Raymond Chan, Hongfei Yang, and Tieyong Zeng. A two-stage image segmentation method for blurry images with poisson or multiplicative gamma noise. *SIAM Journal on Imaging Sciences*, 7(1):98–127, 2014.

[CZBK15] Zhouye Chen, Ningning Zhao, Adrian Basarab, and Denis Kouamé. Ultrasound compressive deconvolution with lp-norm prior. In *Proc. European Signal and Image Processing Conference (EUSIPCO)*, Nice, France, 2015.

[Dha11] Atam P. Dhawan. *Medical Image Analysis*, chapter Medical Image Modalites: Ultrasound Imaging. IEEE Press Series in Biomedical Engineering, New Jersey, 2nd edition edition, 2011.

[DM11] Sudipto Dolui and Oleg V. Michailovich. Blind deconvolution of medical ultrasound

images using variable splitting and proximal point methods. In *Proc. IEEE International Symposium on Biomedical Imaging (ISBI)*, pages 1–5, Chicago, IL, 2011.

[EF97a] Michael Elad and Arie Feuer. Restoration of a single superresolution image from several blurred, noisy and undersampled measured images. *IEEE Trans. Image Process.*, 6(12):1646–1658, 1997.

[EF97b] Michael Elad and Arie Feuer. Restoration of a single superresolution image from several blurred, noisy, and undersampled measured images. *IEEE Trans. Image Process.*, 6(12):1646–1658, 1997.

[EHN96] Heinz Werner Engl, Martin Hanke, and Andreas Neubauer. *Regularization of inverse problems*, volume 375. Springer Science & Business Media, 1996.

[EV08] Mehran Ebrahimi and Edward R. Vrscay. Regularization schemes involving self-similarity in imaging inverse problems. In *Proc. 4 th AIP international Conference and the 1st Congress of the IPIA*, 2008.

[Fat09] Raanan Fattal. Edge-avoiding wavelets and their applications. *ACM Trans. Graph.*, 28(3):1–10, Aug. 2009.

[FB85] J. Douglas Faires and Richard L. Burden. *Numerical analysis*. Brooks/Cole, 1985.

[FN03] Mario A. T. Figueiredo and Robert D. Nowak. An EM algorithm for wavelet-based image restoration. *IEEE Trans. Image Process.*, 12(8):906–916, 2003.

[FNW07] Mario A. T. Figueiredo, Robert D. Nowak, and Stephen J. Wright. Gradient projection for sparse reconstruction: Application to compressed sensing and other inverse problems. *IEEE Trans. Image Process.*, 1(4):586–597, Dec. 2007.

[FOG15] O. Féron, F. Orieux, and J.-F. Giovannelli. Gradient scan Gibbs sampler: an efficient algorithm for high-dimensional Gaussian distributions. 2015.

[FPC00] William T. Freeman, Egon C. Pasztor, and Owen T. Carmichael. Learning low-level vision. *Int. J. Comput. Vis.*, 40(1):25–47, Oct. 2000.

[FREM04] Sina Farsiu, Dirk Robinson, Michael Elad, and Peyman Milanfar. Advances and challenges in super-resolution. *Int. J. Imaging Syst. Technol.*, 14(2):47–57, 2004.

[Gar06] Robert M. Gary. *Toeplitz and circulant matrics: a review.* Now Publishers Inc., 2006.

[GBI09] Daniel Glasner, Shai Bagon, and Michal Irani. Super-resolution from a single image. In *Proc. IEEE Int. Conf. Comp. Vision (ICCV)*, pages 349 – 356, Kyoto, Japan, 2009.

[GCC11] Mark Girolami, Ben Calderhead, and Siu A. Chin. Riemann manifold Langevin and Hamiltonian Monte Carlo methods. *J. Roy. Stat. Soc. Ser. B*, 73:123–214, 2011.

[GCS+13] Andrew Gelman, John B Carlin, Hal S Stern, David B Dunson, Aki Vehtari, and Donald B Rubin. *Bayesian data analysis.* CRC press, Boca Raton, FL, 3 edition, 2013.

[GCTZ09] Yanhui Guo, H.D. Cheng, Jiawei Tian, and Yingtao Zhang. A novel approach to speckle reduction in ultrasound imaging. *Ultrasound in Medicine & Biology*, 35:628–640, 2009.

[GH95] C.A. Glasbey and G.W. Horgan. *Image Analysis for the Biological Sciences*, chapter Segmentation. John Wiley & Sons, Inc., 1995.

[GK15] Murat Alparslan Gungor and Irfan Karagoz. The homogeneity MAP method for speckle reduction in diagnostic ultrasound images. *Measurement*, 68:100–110, 2015.

[GMI15] Clement Gilavert, Said Moussaoui, and Jerome Idier. Efficient Gaussian sampling for solving large-scale inverse problems using MCMC. *IEEE Trans. Image Process.*, 63(1):70–80, 2015.

[GR92] A. Gelman and D.B. Rubin. Inference from iterative simulation using multiple sequences. *Stat. Sci.*, 7(4):457–511, 1992.

[Hag89] William W. Hager. Updating the inverse of a matrix. *SIAM Rev.*, pages 221–239, 1989.

[Has70] W Keith Hastings. Monte Carlo sampling methods using Markov chains and their applications. *Biometrika*, 57(1):97–109, 1970.

[HG14] Matthew D. Hoffman and Andrew Gelman. The no-U-turn sampler: Adaptively setting path lengths in Hamiltonian Monte Carlo. *Journal of Machine Learning Research*, 15(Apr):1593–1623, 2014.

[HO09] David P. Hruska and Michael L. Oelze. Improved parameter estimates based on the homodyned K distribution. *IEEE Trans. Ultrason. Ferroelectr. Freq. Control*, 56(11):2471–2481, 2009.

[HSA15] Jia-Bin Huang, Abhishek Singh, and Narendra Ahuja. Single image super-resolution from transformed self-exemplars. In *Proc. IEEE Conference on Computer Vision and Pattern Recognition (CVPR)*, Boston, Massachusetts, USA, 2015.

[Jen96] Jorgen Arendt Jensen. Field: A program for simulating ultrasound systems. *Med. Biol. Eng. Comput.*, 34:351–353, 1996.

[JJC04] C. V. Jiji, M. V. Joshi, and S. Chaudhuri. Single-frame image super-resolution using learned wavelet coefficients. *Int. J. Imaging Syst. Technol.*, 14:105–112, 2004.

[JL94] Jorgen Arendt Jensen and Sidney Leeman. Nonparametric estimation of ultrasound pulses. *IEEE Trans. Biomed. Eng.*, 41(10):929–936, Oct. 1994.

[JMGS93] Jorgen Arendt Jensen, Jan Mathorne, Torben Gravesen, and Bjarne Stage. Deconvolution of *in vivo* ultrasound B-mode images. *Ultrason. Imaging*, 15(2):122–133, Apr. 1993.

[JNN+12] Are Charles Jensen, Sven Peter Nasholm, Carl-Inge Colombo Nilsen, Andreas Austeng, and Sverre Holm. Applying Thomson's multitaper approach to reduce speckle in medical ultrasound imaging. *IEEE Trans. Ultrason. Ferroelectr. Freq. Control*, 59(10):2178–2185, 2012.

[JT08] Radovan Jirik and Torfinn Taxt. Two dimensional blind Bayesian deconvolution of medical ultrasound images. *IEEE Trans. Ultrason. Ferroelectr. Freq. Control*, 55(10):2140–2153, 2008.

[Kre10] Frederick Kremkau. *Sonography principle and instruments*. Saunders, 8 edition, 2010.

[KTHD12] Georg Kail, Jean-Yves Tourneret, Franz Hlawatsch, and Nicolas Dobigeon. Blind deconvolution of sparse pulse sequences under a minimum distance constraint: A partially collapsed Gibbs sampler method. *IEEE Trans. Signal Process.*, 60:2727 – 2743, Mar. 2012.

[LCR07] Yves Lemoigne, Alessandra Caner, and Ghita Rahal, editors. *Physics for medical imaging applicaitons*. Springer, 2007.

[LN11] A. Larrue and J.A. Noble. Nakagami imaging with small windows. In *Proc. IEEE International Symposium on Biomedical Imaging (ISBI)*, pages 887 – 890, Chicago, IL, USA, 2011.

[LS04] Zhouchen Lin and Heung-Yeung Shum. Fundamental limits of reconstruction based superresolution algorithms under local translation. *IEEE Trans. Patt. Anal. Mach. Intell.*, 26(1):83–97, 2004.

[LWDF09] A. Levin, Y. Weiss, F. Durand, and W. T. Freeman. Understanding and evaluating blind deconvolution algorithms. In *Proc. IEEE Conference on Computer Vision and Pattern Recognition (CVPR)*, Miami, FL, USA, 2009.

[MA01] Oleg Michailovich and Dan Adam. Phase unwrapping for 2-D blind deconvolution of ultrasound images. *IEEE Trans. Med. Imag.*, 23(1):7–25, 2001.

[MA03] Oleg Michailovich and Dan Adam. Robust estimation of ultrasound pulses using outlier-resistant de-noising. *IEEE Trans. Med. Imag.*, 22(3):368–381, 3 2003.

[MA05] Oleg Michailovich and Dan Adam. A novel approach to the 2-D blind deconvolution problem in medical ultrasound. *IEEE Trans. Med. Imag.*, 24:86–104, 2005.

[MA07] Oleg V. Michailovich and Dan R. Adam. *Blind image deconvolution: theory and applications*, chapter Deconvolution of medical images from microscopic to whole body images, pages 169–230. CRC Press, Taylor & Francis Group, LLC, 2007.

[MBBK13] Renaud Morin, Stephanie Bidon, Adrian Basarab, and Denis Kouame. Semi-blind deconvolution for resolution enhancement in ultrasound imaging. In *Proc. IEEE Int. Conf. on Image Process (ICIP)*, Melbourne, Australia, 2013.

[MBD15] Gabriel Martin and Jose M. Bioucas-Dias. Hyperspectral compressive acquisition in the spatial domain via blind factorization. In *Proc. IEEE Workshop on Hyperspectral Image and Signal Processing: Evolution in Remote Sensing (WHISPERS)*, Tokyo, Japan, June 2015.

[MBK12] Renaud Morin, Adrian Basarab, and Denis Kouame. Alternating direction method of multipliers framework for super-resolution in ultrasound imaging. In *Proc. IEEE International Symposium on Biomedical Imaging (ISBI)*, pages 1595–1598, Barcelona, Spain, May 2012.

[MGM06] Iain Murray, Zoubin Ghahramani, and David J. C. MacKay. MCMC for doubly-intractable distributions. In *In Proc. 22nd Annu. Conf. Uncertainty Artif. Intell (UAI)*, pages 356–366, Cambridge, MA, USA, 2006.

[Mig06] Max Mignotte. A segmentation-based regularization term for image deconvolution. *IEEE Trans. Image Process.*, 15(7):1973–1984, 2006.

[MO08] Antonio Marquina and StanleyJ. Osher. Image super-resolution by TV-regularization and Bregman iteration. *J. Sci. Comput.*, 37(3):367–382, 2008.

[Mor13] Renaud Morin. *Amélioration de la résolution en imagerie ultrasonore.* PhD thesis, University of Toulouse, 2013.

[MR15] Oleg Michailovich and Yogesh Rathi. Adaptive learning of tissue reflectivity statistics

and its application to deconvolution of medical ultrasound scans. In *Proc. IEEE Int. Ultrasonics Symposium (IUS)*, 2015.

[MS12] Goran Marjanovic and Victor Solo. On l_q optimization and matrix completion. *IEEE Trans. Signal Process.*, 60(11):5714–5724, 2012.

[MT06] Oleg Michailovich and Allen Tannenbaum. Despeckling of medical ultrasound images. *IEEE Trans. Ultrason. Ferroelectr. Freq. Control*, 53(1):64–78, 2006.

[MT07] Oleg Michailovich and Allen Tannenbaum. Blind deconvolution of medical ultrasound images: A parametric inverse filtering approach. *IEEE Trans. Image Process.*, 16(12):3005–3019, 2007.

[MY10] Stephane Mallat and Guoshen Yu. Super-resolution with sparse mixing estimators. *IEEE Trans. Image Process.*, 19(11):2889–2900, 2010.

[NB06] J. Alison Noble and Djamal Boukerroui. Ultrasound image segmentation: A survey. *IEEE Trans. Med. Imag.*, 25(8):987–1010, 2006.

[Nea11] Radford M. Neal. *Handbook of Markov chain Monte Carlo*, chapter MCMC using Hamiltonian dynamics. Chapman and Hall/CRC Handbooks of Modern Statistical Methods. 2011.

[Ng06] James Kee Huat Ng. *Restoration of Medical Pulse-Echo Ultrasound Images*. PhD thesis, Trinity College, University of Cambridge, 2006.

[NMG01] Nhat Nguyen, Peyman Milanfar, and Gene Golub. A computationally efficient superresolution image reconstruction algorithm. *IEEE Trans. Image Process.*, 10(4):573–583, 2001.

[NO98] James G. Nagy and Dianne P. O'Leary. Restoring images degraded by spatially variant blur. *SIAM J. Sci. Comput.*, 19(4):1063–1082, Jul. 1998.

[Nob10] J. Alison Noble. Ultrasound image segmentation and tissue characterization. *J. Engineering in Medicine*, pages 307–316, 2010.

[NPK+06] James Ng, Richard Prager, Nick Kingsbury, Graham Treece, and Andrew Gee. Modeling ultrasound imaging as a linear, shift-variant system. *IEEE Trans. Ultrason. Ferroelectr. Freq. Control*, 53(3):549–563, 2006.

[NPK+07] James Ng, Richard Prager, Nick Kingsbury, Graham Treece, and Andrew Gee. Wavelet restoration of medical pulse-echo ultrasound images in an EM framework. *IEEE Trans. Ultrason. Ferroelectr. Freq. Control*, 54(3):550–568, 2007.

[NWY10] Michael K. Ng, Pierre Weiss, and Xiaoming Yuan. Solving constrained total-variation image restoration and reconstruction problems via alternating direction methods. *SIAM J. Sci. Comput.*, 32:2710–2736, 2010.

[OFG12] F. Orieux, O. Féron, and J. F. Giovannelli. Sampling high-dimensional Gaussian distributions for general linear inverse problems. *IEEE Signal Process. Lett.*, 19(5):251–254, 2012.

[Opp65] A. V. Oppenheim. Superposition in a class of non-linear systems. Technical report, Research Lab. of Electronics, MIT, 1965.

[Ots79] Nobuyuki Otsu. A threshold selection method from gray-level histograms. *IEEE Trans. Systems, Man, Cybernet.*, 9:62–66, Jan. 1979.

[PCS13] Grégory Paul, Janick Cardinale, and Ivo F. Sbalzarini. Coupling image restoration and segmentation: A generalized linear model/Bregman perspective. *Int. J. Comput. Vis.*, 104(1):69–93, 2013.

[PD03] Soo-Chang Pei and Jian-Jiun Ding. The generalized radial Hilbert transform and its applications to 2-D edge detection (any direction or specified direction). In *Acoustics, Speech, and Signal Processing, 2003. Proceedings. (ICASSP '03). 2003 IEEE International Conference on*, volume 3, Apr. 2003.

[PDBT12] Marcelo Pereyra, Nicolas Dobigeon, Hadj Batatia, and Jean-Yves Tourneret. Segmentation of skin lesions in 2-D and 3-D ultrasound images using a spatially coherent generalized Rayleigh mixture model. *IEEE Trans. Med. Imag.*, 31(8):1509–1520, 2012.

[PDBT13] Marcelo Pereyra, Nicolas Dobigeon, Hadj Batatia, and Jean-Yves Tourneret. Estimating the granularity coefficient of a Potts-Markov random field within a Markov chain Monte Carlo algorithm. *IEEE Trans. Image Process.*, 22(6):2385–2397, 2013.

[Per12] Marcelo Pereyra. *Statistical modeling and processing of high frequency ultrasound images: application to determatologic oncology.* PhD thesis, Institut National Polytechnique de Toulouse (INP Toulouse), 2012.

[Per15] Marcelo Pereyra. Proximal Markov chain Monte Carlo algorithms. 2015.

[Per16] Antonios Perperidis. Postprocessing apapproach for the improvement of cardiac ultrasound b-mode images: a review. *IEEE Trans. Ultrason. Ferroelectr. Freq. Control*, 63(3):470–485, 2016.

[PFG04] G. Rilling P. Flandrin and P. Goncalves. Empirical mode decomposition as a filter bank. *IEEE Signal Process. Lett.*, 11(2):112Ű114, 2004.

[PPK03] Sung Cheol Park, Min Kyu Park, and Moon Gi Kang. Super-resolution image reconstruction: a technical overview. *IEEE Signal Process. Mag.*, 20:21–36, 2003.

[RAHA14] Ole Marius Hoel Rindal, Jon Petter Asen, Sverre Holm, and Andreas Austeng. Understanding contrast improvements from capon beamforming. In *Proc. IEEE Int. Ultrasonics Symposium (IUS)*, Chicago, IL, USA, 2014.

[RB05] Stefan Roth and Michael J. Black. Fields of experts: a framework for learning image priors. In *Proc. IEEE Conference on Computer Vision and Pattern Recognition (CVPR)*, pages 860–867, 2005.

[Rob07] Christian P. Robert. *The Bayesian Choice: from Decision-Theoretic Motivations to Computational Implementation*. Springer Texts in Statistics. Springer-Verlag, New York, NY, USA, 2 edition, 2007.

[RPD+15] Audrey Repetti, Mai Quyen Pham, Laurent Duval, Emilie Chouzenoux, and Jean-Christophe Pesquet. Euclid in a taxicab: Sparse blind deconvolution with smoothed ℓ_1/ℓ_2 regularization. *IEEE Signal Process. Lett.*, 22(5):539–543, 2015.

[RT96] Gareth O. Roberts and Richard L. Tweedie. Exponential convergence of langevin distributions and their discrete approximations. *Bernoulli*, 2(4):341–363, 12 1996.

[RTLF10] M. Dirk Robinson, Cynthia A. Toth, Joseph Y. Lo, and Sina Farsiu. Efficient Fourier-Wavelet super-resolution. *IEEE Trans. Image Process.*, 19(10):2669–2681, 2010.

[SDR10] Kalpana Saini, M. L. Dewal, and Manojkumar Rohit. Ultrasound imaging and image segmentation in the area of ultrasound: a review. *Int. J. Advanced Science and Technology*, 24:41–60, Nov. 2010.

[SFCM14] Amandine Schreck, Gersende Fort, Sylvain Le Corff, and Eric Moulines. A shrinkage-thresholding Metropolis adjusted Langevin algorithm for Bayesian variable selection. 2014.

[SKM11] Filip Sroubek, Jan Kamenicky, and Peyman Milanfar. Superfast superresolution. In *Proc. IEEE Int. Conf. Image Process. (ICIP)*, Brussels, Belgium, 2011.

[SS04] Mehmet Sezgin and Bulent Sankur. Survey over image thresholding techniques and quantitative performance evaluation. *Journal of Electronic Imaging*, 13(1):146–168, 2004.

[SSXS08] Jian Sun, Jian Sun, Zongben Xu, and Heung-Yeung Shum. Image super-resolution using gradient profile prior. In *Proc. IEEE Conference on Computer Vision and Pattern Recognition (CVPR)*, pages 1–8, Anchorage, AK, 2008.

[SSXS11] Jian Sun, Jian Sun, Zongben Xu, and Heung-Yeung Shum. Gradient profile prior and its applications in image super-resolution and enhancement. *IEEE Trans. Image Process.*, 20(6):1529 – 1542, 2011.

[SWFU15] Martin Storath, Andreas Weinmann, Jurgen Frikel, and Michael Unser. Joint image reconstruction and segmentation using the Potts model. *Inv. Prob.*, (2):1–29, 2015.

[Sza04] Thomas L. Szabo. *Diagnostic Ultrasound Imaging: Inside Out.* Academic Press., 2004.

[Tax95] Torfinn Taxt. Restoration of medical ultrasound images using two-dimensional homomorphic deconvolution. *IEEE Trans. Ultrason. Ferroelectr. Freq. Control*, 42(4):543–554, 1995.

[TBU00] Philippe Thévenaz, Thierry Blu, and Michael Unser. Handbook of medical imaging. chapter Image Interpolation and Resampling, pages 393–420. Academic Press, Inc., Orlando, FL, USA, 2000.

[TF14a] M. Tanter and M. Fink. Ultrafast imaging in biomedical ultrasound. *IEEE Trans. Ultrason. Ferroelectr. Freq. Control*, 61(1):102–119, 2014.

[TF14b] Mickael Tanter and Mathias Fink. Ultrafast imaging in biomedical ultrasound. *IEEE Trans. Ultrason. Ferroelectr. Freq. Control*, 61(1):102–119, 2014.

[TLBL10] Yu-Wing Tai, Shuaicheng Liu, Michael S. Brown, and Stephen Lin. Super resolution using edge prior and single image detail synthesis. In *Proc. IEEE Conference on Computer Vision and Pattern Recognition (CVPR)*, pages 2400 – 2407, San Francisco, 2010.

[Tou14] Mathieu Toulemonde. *New beamforming strategy for improved ultrasound imaging: application to biologibio tissues nonlinear imaging.* PhD thesis, L'université de Lyon, 2014.

[VS91] Luc Vincent and Pierre Soille. Watersheds in digital spaces: an efficient algorithm based on immersion simulations. *IEEE Trans. Patt. Anal. Mach. Intell.*, 13:583–598, Jun. 1991.

[Wan09] Yu-Hsiang Wang. Tutorial: Image segmentation. Technical report, Graduate Institute of Communication Engineering, National Taiwan University, Taipei, Taiwan, ROC, 2009.

[WBSS04] Zhou Wang, Alan Conrad Bovik, Hamid Ramhm Sheikh, and Eero P. Simoncelli. Image quality assessment: From error visibility to structural similarity. *IEEE Trans. Image Process.*, 13(4):600–612, 2004.

[WDT15a] Qi Wei, Nicolas Dobigeon, and Jean-Yves Tourneret. Bayesian fusion of multi-band images. *IEEE J. Sel. Topics Signal Process.*, 9(6):1–11, 2015.

[WDT15b] Qi Wei, Nicolas Dobigeon, and Jean-Yves Tourneret. Fast fusion of multi-band images based on solving a Sylvester equation. *IEEE Trans. Geosci. and Remote Sens.*, 53(7):3658–3668, 2015.

[YH10] Jianchao Yang and Thomas Huang. *Super-resolution imaging*, chapter Image super-resolution: Historical overview and future challenges, pages 20–34. Boca Raton, FL, USA: CRC Press, 2010.

[YLTV15] Igor Yanovsky, Bjorn H. Lambrigtsen, Alan B. Tanner, and Luminita A. Vese. Efficient deconvolution and super-resolution methods in microwave imagery. *IEEE J. Sel. Topics Appl. Earth Observations and Remote Sens.*, 8(9):4273–4283, 2015.

[YOGD08] Wotao Yin, Stanley Osher, Donald Goldfarb, and Jerome Darbon. Bregman iterative algorithms for ℓ_1-minimization with applications to compressed sensing. *SIAM J. Imag. Sci.*, 1(1):143–168, 2008.

[YWHM10] Jianchao Yang, John Wright, Thomas S. Huang, and Yi Ma. Image super-resolution via sparse representation. *IEEE Trans. Image Process.*, 19(11):2861–2873, 2010.

[YZX12a] Chengpu Yu, Cishen Zhang, and Lihua Xie. A blind deconvolution approach to ultrasound imaging. *IEEE Trans. Ultrason. Ferroelectr. Freq. Control*, 59(2):271–280, 2012.

[YZX12b] Chengpu Yu, Cishen Zhang, and Lihua Xie. An envelope signal based deconvolution algorithm for ultrasound imaging. *Signal Processing*, 92(3):793 – 800, 2012.

[ZBKT14] Ningning Zhao, Adrian Basarab, Denis Kouamé, and Jean-Yves Tourneret. Restoration of ultrasound images using a hierarchical Bayesian model with a generalized Gaussian prior. In *Proc. IEEE Int. Conf. Image Process. (ICIP)*, Paris, France, 2014.

[ZBKT15] Ningning Zhao, Adrian Basarab, Denis Kouame, and Jean-Yves Tourneret. Joint bayesian deconvolution and point spread function estimation for ultrasound imaging. In *Proc. IEEE International Symposium on Biomedical Imaging (ISBI)*, New York, USA, April 2015.

[ZBKT16] Ningning Zhao, Adrian Basarab, Denis Kouamé, and Jean-Yves Tourneret. Joint segmentation and deconvolution of ultrasound images using a hierarchical Bayesian model based on generalized Gaussian priors. *IEEE Trans. Image Process.*, 25(8):3736 – 3750, 2016.

[ZEP12] Roman Zeyde, Michael Elad, and Matan Protter. On single image scale-up using sparse-representations. In Jean-Daniel Boissonnat, Patrick Chenin, Albert Cohen, Christian Gout, Tom Lyche, Marie-Laurence Mazure, and Larry Schumaker, editors, *Curves and Surfaces*, volume 6920 of *Lecture Notes in Computer Science*, pages 711–730. Springer Berlin Heidelberg, 2012.

[ZGTL12] K. Zhang, X. Gao, D. Tao, and X. Li. Single image super-resolution with non-local means and steering kernel regression. *IEEE Trans. Image Process.*, 21(11):4544–4556, 2012.

[ZMZ+13] Wangmeng Zuo, Deyu Meng, Lei Zhang, Xiangchu Feng, and David Zhang. A generalized iterated shrinkage algorithm for non-convex sparse coding. In *Proc. IEEE Int. Conf. Comp. Vision (ICCV)*, Sydney, Australia, 2013.

[ZW08] Xiangjun Zhang and Xiaolin Wu. Image interpolation by adaptive 2-D autoregressive modeling and soft-decision estimation. *IEEE Trans. Image Process.*, 17(6):887–896, 2008.

[ZW11] Daniel Zoran and Yair Weiss. From learning models of natural image patches to whole image restoration. In *Proc. IEEE Int. Conf. Comp. Vision (ICCV)*, pages 479–486, Barcelona , Spain, 2011.

[ZWB+16a] Ningning Zhao, Qi Wei, Adrian Basarab, Nicolas Dobigeon, Denis Kouame, and Jean-Yves Tourneret. Fast single image super-resolution using a new analytical solution for $\ell_2 - \ell_2$ problems. *IEEE Trans. Image Process.*, 25(8):3683–3697, 2016.

[ZWB+16b] Ningning Zhao, Qi Wei, Adrian Basarab, Denis Kouamé, and Jean-Yves Tourneret. Blind deconvolution of medical ultrasound images using a parametric model for the point spread function. In *Proc. IEEE Int. Ultrasonics Symposium (IUS)*, Tours, France, 2016.

[ZWB+16c] Ningning Zhao, Qi Wei, Adrian Basarab, Denis Kouame, and Jean-Yves Tourneret. Single image super-resolution of medical ultrasound images using a fast algorithm. In *Proc. IEEE International Symposium on Biomedical Imaging (ISBI)*, Prague, CZ, April 2016.

[ZWZ97] W. Zhu, Y. Wand, and J. Zhang. Total least squares reconstruction with wavelets for optical tomography. *Journal of the Optical Society of America A*, 15:2639–2650, 1997.